Publication Year	2006
Acceptance in OA	2024-06-24T12:14:53Z
Title	Data analysis and scientific performances of the LFI QM instrument
Authors	MENNELLA, ANIELLO, CUTTAIA, FRANCESCO, Leonardi. Rodrigo, MARIS, Michele, Meinhold, Peter, Salmon, M, STRINGHETTI, LUCA, Tomasi, Maurizio, VALENZIANO, Luca
Handle	http://hdl.handle.net/20.500.12386/35225
Volume	PL-LFI-PST-AN-005

UniMI / IASF-INAF / UCSB / OAT / SAN
LFI Project System Team

Planck LFI

TITLE:

Data analysis and scientific performances of the LFI QM instrument

DOC. TYPE: ANALYSIS DOCUMENT

PROJECT REF.: PL-LFI-PST-AN-005 **PAGE:** I of VI, 94

ISSUE/REV.: 1.0 **DATE:** March 2006

Prepared by	**A. MENNELLA** **F. CUTTAIA** **R. LEONARDI** **M. MARIS** **P. MEINHOLD** **M. SALMON** **L. STRINGHETTI** **M. TOMASI** **L. VALENZIANO** **LFI** **Project System Team**	**Date:** **Signatures:**	**March 20th, 2006** [redacted]
Agreed by	**M. BERSANELLI** **LFI** **Instrument Scientist** **R.C. BUTLER** **LFI** **Program Manager**	**Date:** **Signatures:**	**March 20th, 2006** [redacted]
Approved by	**N. MANDOLESI** **LFI** **Principal Investigator**	**Date:** **Signature:**	**March 20th, 2006** [redacted]

CHANGE RECORD

Issue	**Date**	**Sheet**	**Description of change**	**Release**
0.1	18th Nov, 2005	All	First draft issue of document	0.1
0.2	2nd Oct, 2005	All	Added results from THF test, corrected results for noise properties test	0.2
0.3	6th Oct, 2005	All	Corrected some values in tables in summary tables, added comparison of white noise at comparable experimental conditions	0.3
0.4	25th Nov, 2005	All	Added analysis of dynamic thermal test, added analysis of back-end thermal variations, updated analysis of noise properties. Updated the results on noise temperature of LFI24 channels A and B using data from ELE-0001 test which were acquired without the DAE gain and offset applied. Removed the susceptibility data from the summary table (data are present in the dedicated sections). Removed decimals which are not significant from results.	0.4
1.0	16th Mar, 2006	All	Added analysis of ELE tset, added comprehensive analysis of receiver basic properties, added removal of BEU instability effect, added assessment of time and people resources for flight testing.	1.0

DISTRIBUTION LIST

Recipient	**Company/Institute**	**E-mail address**	**Sent**
E. Alippi	Alenia Spazio S.p.A.	`alippi.e@laben.it`	Yes
M. Balasini	Alenia Spazio S.p.A.	`balasini.m@laben.it`	Yes
P. Battaglia	Alenia Spazio S.p.A.	`battaglia.p@laben.it`	Yes
E. Artal	Univ. of Cantabria - Santander	`artal@dicom.unican.es`	Yes
A. Balbi	Univ. di Roma Tor Vergata	`amedeo.balbi@roma2.infn.it`	Yes
M. Bersanelli	Univ. degli studi di Milano	`marco.bersanelli@fisica.unimi.it`	Yes
C. Burigana	INAF-IASF sez di Bologna	`burigana@iasfbo.inaf.it`	Yes
C. Butler	IASF-CNR Sez di Bologna	`butler@iasfbo.inaf.it`	Yes
G. Cafagna	Alenia Spazio S.p.A.	`cafagna.g@laben.it`	Yes
B. Cappellini	Univ. degli studi di Milanl	`benedetta.cappellini@mi.infn.it`	Yes
B. Collaudin	ASPI - Cannes	`bernard.collaudin@space.alcatel.fr`	Yes
F. Cuttaia	INAF-IASF sez di Bologna	`cuttaia@iasfbo.inaf.it`	Yes
O. D'Arcangelo	IFP - CNR	`ocleto@ifp.cr.it`	Yes
R. Davis	JBO - UK	`rjd@jb.man.ac.uk`	Yes
G. de Gasperis	Univ. di Roma Tor Vergata	`Giancarlo.Degasperis@roma2.infn.it`	Yes
L. Figini	IFP - CNR	`figini@ifp.cr.it`	Yes
C. Franceschet	Alenia Spazio S.p.A.	`franceschet.c@laben.it`	Yes
E. Franceschi	INAF-IASF sez di Bologna	`franceschi@iasfbo.inaf.it`	Yes
T. Gaier	JPL - Pasadena	`gaier@merlin.jpl.nasa.gov`	Yes
S. Galeotta	INAF-IASF sez di Milano	`samuele@lambrate.inaf.it`	Yes
A. Gregorio	Univ. di Trieste	`anna.gregorio@ts.infn.it`	Yes
G. Guyot	IAS - Orsay	`guyot@ias.u-psud.fr`	Yes
R. Hoyland	IAC - Tenerife	`rjh@ll.iac.es`	Yes
N. Hughes	Ylinen	`nicholas.hughes@elektrobit.com`	Yes
D. Kettle	JBO - UK	`dkettle@jb.man.ac.uk`	Yes
M. Laaninen	Ylinen	`mikko.laaninen@elektrobit.com`	Yes
J.M. Lamarre	IAS - Orsay	`lamarre@ias.u-psud.fr`	Yes
C. Lawrence	JPL - Pasadena	`crl@jplsp.ipl.nasa.gov`	Yes
R. Leonardi	UCSB – USA	`rodrigo@deepspace.ucsb.edu`	Yes
P. Leutenegger	Alenia Spazio S.p.A.	`leutenegger.p@laben.it`	Yes
D. Maino	Univ. degli studi di Milano	`davide.maino@fisica.unimi.it`	Yes
M. Malaspina	INAF-IASF sez di Bologna	`malaspina@iasfbo.inaf.it`	Yes
N. Mandolesi	INAF-IASF Sez. di Bologna	`reno@iasfbo.inaf.it`	Yes
M. Maris	INAF-OAT - Trieste	`maris@oat.ts.astro.it`	Yes
J. Marti Canales	ESA	`javier.marti.canales@esa.int`	Yes
E. Martinez-Gonzalez	Univ. of Cantabria - Santander	`martinez@ifca.unican.es`	Yes
P. Meinhold	UCSB – USA	`peterm@cfi.ucsb.edu`	Yes
L. Mendes	ESA	`lmendes@rssd.esa.int`	Yes
A. Mennella	Univ. degli studi di Milano	`daniele.mennella@fisica.unimi.it`	Yes
M. Miccolis	Alenia Spazio S.p.A.	`miccolis.m@laben.it`	Yes
G. Morgante	INAF-IASF Sez. di Bologna	`morgante@iasfbo.inaf.it`	Yes
P. Natoli	Univ. di Roma Tor Vergata	`paolo.natoli@roma2.infn.it`	Yes
L. Pagan	Alenia Spazio S.p.A.	`pagan.l@laben.it`	Yes
F. Pasian	INAF-OAT - Trieste	`pasian@oat.ts.astro.it`	Yes

T. Passvogel	ESA - PT	`tpassvog@estec.esa.nl`	Yes
L. Perez	ESA	`Leticia.Perez.Cuevas@esa.int`	Yes
L. Popa	INAF-IASF sez di Bologna	`popa@iasfbo.inaf.it`	Yes
J.L. Puget	IAS - Orsay	`puget@ias.u-psud.fr`	Yes
N. Roddis	JBO - UK	`nr@jb.man.ac.uk`	Yes
M. Salmon	Univ. of Cantabria - Santander	`salmon@ifca.unican.es`	Yes
M. Sandri	INAF-IASF sez di Bologna	`sandri@iasfbo.inaf.it`	Yes
M. Seiffert	JPL - Pasadena	`michael.d.seiffert@jpl.nasa.gov`	Yes
R. Silvestri	Alenia Spazio S.p.A.	`silvestri.r@laben.it`	Yes
A. Simonetto	IFP - CNR	`simonetto@ifp.cr.it`	Yes
C. Sozzi	IFP - CNR	`sozzi@ifp.cr.it`	Yes
L. Stringhetti	INAF-IASF sez di Bologna	`stringhetti@iasfbo.inaf.it`	Yes
J. Tauber	ESA	`jtauber@astro.estec.esa.nl`	Yes
L. Terenzi	INAF-IASF sez di Bologna	`terenzi@iasfbo.inaf.it`	Yes
M. Tomasi	INAF-IASF sez di Milano	`tomasi@lambrate.inaf.it`	Yes
J. Tuovinen	Millilab	`jussi.tuovinen@vtt.fi`	Yes
L. Valenziano	INAF-IASF sez di Bologna	`valenziano@iasfbo.inaf.it`	Yes
J. Varis	Millilab	`jussi.varis@vtt.fi`	Yes
F. Villa	INAF-IASF sez di Bologna	`villa@iasfbo.inaf.it`	Yes
A. Wilkinson	JBO - UK	`aw@jb.man.ac.uk`	Yes
F. Winder	JBO - UK	`fwinder@jb.man.ac.uk`	Yes
A. Zacchei	INAF-OAT - Trieste	`zacchei@ts.astro.it`	Yes
A. Zonca	Univ. degli Studi di Milano	`andrea.zonca@mi.infn.it`	Yes
LFI System PCC	INAF-IASF sez di Bologna	`lfispcc@iasfbo.inaf.it`	Yes

Contents

1 Summary 2
1.1 Changelog 2
1.2 Summary of calibration tests 2
1.3 Achievements and limitations 9
1.3.1 Summary of main achievements 9
1.3.2 Summary of main limitations and problem areas 10
1.4 Lessons learned and actions for the flight testing phase 11
1.5 Estimate of needed time and resources needed for LFI-FM ground testing 12

2 Scientific performace summary and comparison with RCA measurements 13
2.1 30 GHz LFI 28 13
2.2 44 GHz LFI 24 16
2.3 70 GHz LFI 23 17

3 Cryofacility setup and performances 20

4 Bias settings and channel mapping 22

5 Basic performances 22
5.1 Experimental conditions 23
5.1.1 Tests used in the analysis 23
5.1.2 Temperature sensor for monitoring sky and reference load temperatures 24
5.1.3 Major non idealities 24
5.1.4 BEM DC offset and DAE gain/offset settings 27
5.2 Noise temperature, photometric calibration and isolation 27
5.2.1 Case 1: metal plate sensor 28
5.2.2 Case 2: ECCOSORB sensor 35
5.3 Linearity 43
5.4 Offset 43

6 Noise properties 44
6.1 Experimental conditions 44
6.2 RAA 30 GHz #28 QM noise parameters 47
6.3 RAA 44 GHz #24 QM noise parameters 50
6.4 RAA 70 GHz #23 QM noise parameters 52
6.5 Conclusion 54

7 Susceptibility tests 54
7.1 Susceptibility to front-end temperature fluctuations 54
7.1.1 Test theory 54
7.1.2 Test experimental conditions 54
7.1.3 Temperature behaviour during the test 57
7.1.4 Results 59
7.1.5 Conclusions 61
7.2 Susceptibility to back-end temperature fluctuations 62
7.2.1 Test theory 62
7.2.2 Test experimental conditions 62
7.2.3 Results 68

7.3 Susceptibility to bias voltage fluctuations 70
    7.3.1 Test theory 70
    7.3.2 Test experimental conditions 70
    7.3.3 Results 74

8 REBA quantisation and compression tests 74
8.1 Behaviour of the compression rate versus the quantisation factor 74
8.2 Impact of second quantisation on scientific output 76

9 Dynamic thermal response of the focal plane unit to temperature fluctuations 76

A Appendix: Receiver basic properties – detailed figures 76

B Appendix: Technical note on dynamic thermal tests 81

Abstract

In this report we discuss the results of the scientific analysis of the radiometric data acquired during the calibration and testing of the LFI QM instrument.

Reference Documents

[RD1] F. Cuttaia, L. Stringhetti, and L. Terenzi. Analysis of thermal Behaviour of RAA Cryogenic Chamber Sensors in ALS. Technical Report PL-LFI-PST-TN-066 0.1, IASF-BO, September 2005.

[RD2] A. Mennella et al. Effect of Sorption Cooler Temperature Variations on the LFI Front–End. Technical Report PL-LFI-PST-TN-005 2.0, IFC–CNR, October 2001.

[RD3] M. et al Maris. Planck LFI - Test Report on the TMH/QM by Using a Know Signal Test Data. Technical Report PL-LFI-OAT-RP-014, INAF/OAT, March 2006.

[RD4] A. Mennella. LFI calibration and testing data analysis methods. Technical Report PL-LFI-PST-TN-068, UniMi, November 2005.

[RD5] A. Mennella and C. Franceschet. Data analysis of LFI 24 44GHz RAA data to understand anomalous results obtained in LFI QM RAA activity. Technical Report PL-LFI-PST-TN-069, UniMi, AAS, November 2005.

Applicable Documents

[AD1] M. Bersanelli. Planck-LFI calibration plan. Technical Report PL-LFI-PST-PL-008, IASF – UniMi, July 2003.

[AD2] P. Leutenegger. Title to be defined. Technical Report PL-LFI-LAB-XX-YYY, Alcatel - Alenia Spazio, September 2005.

[AD3] A Mennella, P. Meinhold, T. Bernardino, M. Salmon, F. Villa, C. Franceschet, P. Battaglia, and P. Leutenegger. Data analysis and calibration matrix of LFI 44 GHz QM receiver (LFI24). Technical Report PL-LFI-PST-AN-003, UniMi, IASF-INAF, UCSB, Univ. Santander, Alenia Spazio, May 2005.

[AD4] A Mennella, P. Meinhold, P. Leonardi, M. Salmon, F. Villa, C. Franceschet, P. Battaglia, and P. Leutenegger. Data analysis and calibration matrix of LFI 30 GHz QM receiver (LFI28). Technical Report PL-LFI-PST-AN-004, UniMi, IASF-INAF, UCSB, Univ. Santander, Alenia Spazio, May 2005.

[AD5] Planck Team. Planck-LFI QM test report. Technical Report PL-LFI-LAB-RP-048 1.0, Alcatel/Alenia Spazio, November 2005.

1 Summary

1.1 Changelog

This document is an update of version 0.3 that was issued on Oct 6th. The main changes have been:

- added results from the analysis of the dynamic thermal test;
- added results from the analysis of back-end temperature susceptibility;
- added results from the analysis of susceptibility to bias voltage variations;
- updated the noise properties section with an uncertainty analysis on the white noise level;
- added a summary of the cryofacility test setup;
- added an analysis of basic properties with effect from BEM fluctuation removed;
- added an uncertainty analysis applied to the determination of basic properties;

1.2 Summary of calibration tests

The LFI QM instrument consists of a subset of the receivers that will be present on the flight model, i.e.: one receiver at 30 GHz (LFI28) one receiver at 44 GHz (LFI24) and two receivers at 70 GHz (LFI18 and LFI23). In Figure 1 we show the the QM RCAs in the LFI focal plane.

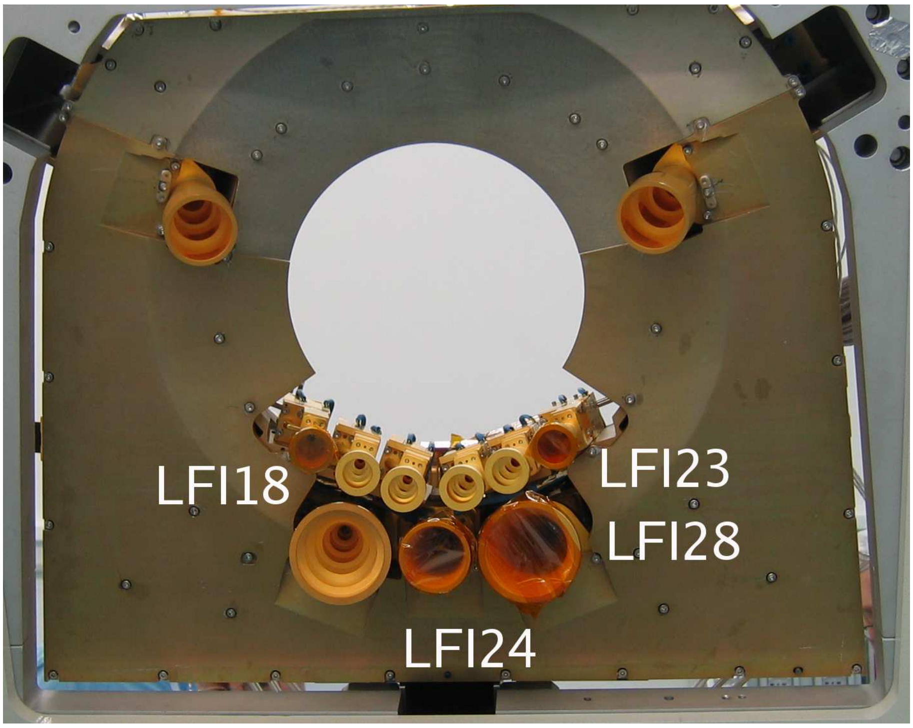

Figure 1: Picture of the LFI QM focal plan with labels indicating the QM RCAs

The sequence of the calibration tests to be performed at the various integration levels of the Planck-LFI instrument is defined in the Planck-LFI calibration plan [AD1]. The list of these tests was reviewed by the calibration team before the start of the test activity to define, for schedule reasons, a reduced test plan. The result of this assessment is summarised in the table below that reports, for each test, the indication of its priority (Mandatory, Desired, Low priority).

In the last column we also indicate whether and in which conditions the test has been run.

Table 1: Summary of the tests forseen by the LFI calibration plan

Test	Acronym in Calibration Plan	RCAs	Details	Notes	Importance	test status
FUNCTIONALITY						
Radiometric functionality	N/A	ALL	Switch on receiver channels one by one Verify functionality of LNAs and phase switches Verify correspondence between FEM biases and BEM outputs (i.e. verify that to bias variations on channels A-B on FEM correspond a signal variation on channel A-B on B	All this part is crucial to be confident that the whole system responds as expected. The most part of debugging is expected in this phase.	**Mandatory**	Done
Cryo-chamber thermal stability verification	N/A	ALL	Verify temperature stability of the various thermal stages and tune the parameters of the PID controllers to guarantee proper stability Check for long-term drifts	This is essential to ensure that all the subsequent radiometric tests are performed in temperature controlled environment	**Mandatory**	Not done: The cryo chamber has many points where is out of specs.
TUNING						
Tuning of DAE parameters	RAA_TUN	ALL	Set the DAE offset removal and gain to optimise the ADC conversion	DAE offset and gain must be tuned in order to optimise the input signal to the ADC dynamic range. Without this the radiometer noise limit could be dominated by the post-acquisition noise	**Mandatory**	Done only on 44 GHz Chain.
Tuning of phase switch biases	RAA_TUN	At least 30 GHz	Find the optimal phase switch biases	The phase switch biases are tuned in order to guarantee maximum amplitude balance in the two states	**Desired**	Not done. Set to RCA's test campaign otpimal values.
Tuning of LNA gate 1 voltage	RAA_TUN	At least 30 GHz	Find the optimal value of the gate 1 voltage for each LNA	This is a very important tuning which affects the noise temperature. The test is mandatory because we need to have the procedure fully under control before the flight instrument tests	**Mandatory**	Done: we have two set of output data at T_high and T_low, for all RCA's. TQL data have to be verified.
Tuning of LNA gate 2 voltage	RAA_TUN	At least 30 GHz	Find the optimal value of the gate 2 voltage for each LNA	In this case the test could be run using the second temperature step used to bring the sky load to starting temperature condition.	***Desired***	Scheduled to not to test in QM campaign
Tuning of REBA parameters	RAA_REB	All	For each channel the optimal values of the parameters q (quantisation factor), O (quantisation offset), r1 and r2 (gain modulation factors) are found	This tuning is fundamental to fix at first order the optimal values of these parameters (they will be fine-tuned, however, in flight). It is also important if any of the subsequent tests need to be run in the nominal operation mode (mode 5) which foresee	**Mandatory**	Partially completed. Tuning of r1 and r2 has not been performed, but script is ready. A comparison on the same channel with different values of r1 and r2 exists.
RADIOMETRIC PERFORMANCE TESTS (BASIC PARAMETERS, NOISE PROPERTIES)						
Noise temperature, calibration constant, linearity, isolation, offset	RAA_TNG RAA_LIS, RAA_OFT	All	Decrease the temperature of the sky load from ~34 K to ~ 20 K Use small sections in the ramp to calculate Tn, G, etc...	This is the test that characterise the main parameters of the receiver. We assume to be able to use the ramp data as quasi-stationary points. A limitation could be the time delay between the temperature change at the sensor and the temperature change at t	**Mandatory**	Done. Note that for the 70 GHz chains the bias configurations have changed after 28/7/2005. Therefore only tests run after this date must be considered for the 70 GHz

Noise properties	RAA_STn, RAA_UNC	All	Measure white noise limit, knee frequency, slope Characterisation of chopped versus unchopped	This test yields other very important parameters necessary to be known on the RAA system. In particular we want to cross-check the values measured at 20K-20K with what has been measured at RCA level	**Mandatory**	Done in not ideal thermal stability conditions. In particular the BEU temperature is unstable (about 1-2 K) over long periods (about 1 hr). The knee frequency is therefore an upper limit to the radiometric one. Note also that the unchopped test at high temperature is present only before the reconfiguration of the 70 GHz biases (UNC_0001).
RADIOMETRIC SUSCEPTIBILITIES						
Susceptibility to DC changes in the temperature of the FPU	RAA_THF	All	Calculate the transfer function for variation of the front end temperature	This parameter is crucial as it can potentially impact the radiometric response in terms of systematic effect	**Mandatory**	Don
Susceptibility to dynamic changes in the temperature of the FPU	RAA_THF	All	Verify the thermal and radiometric response of the FPU to periodic temperature variations at the interface between the sorpion cooler and the LFI instrument	In this case the objective is to induce temperature fluctuations at various frequencies (between 1 Hz and 1 mHz, logarithmically spaced and with a measurement at 1/60 Hz) sample the HK data from the FPU temperature sensors and the scientific data from the	**Mandatory**	Done by using the information collected during the transient.
Susceptibility to DC changes in BEU temperature	RAA_BEU	All	Calculate the radiometric susceptibility to back-end temperature variations	Here we want to induce a change in physical temperature at the BEU external interface (TBC). This test is different from the one run at RCA level. In this case, in fact, we also test the thermal transfer function of the BEU box and we test a situation wh	**Mandatory**	The test was done exploiting the BEU temperature changes occurring during the tests when the input load temperatures were stable.
Susceptibility to DC changes in the reference load temperature	RAA_THR	All	Calculate the radiometric susceptibility to reference load temperature variations	The test involves a change in the temperature of the HFI dummy. In this case the transfer function is simple and already well known from RCA testing. It is not high priority to run on the integrated QM instrument	**Low priority**	Scheduled to not to test in QM campaign
Susceptibility to DC changes in the VG1 temperature	RAA_THV	All	Calculate the radiometric susceptibility to temperature variations at the interface with the coldest V-groove	The tests run at RCA level on the 30-44 GHz radiometers yielded a higher-than-expected susceptibility. It would be highly desirable to repeat it at RAA level to verify the radiometric response and tune the test procedure The dependence of the FPU temperat	**Desired**	Scheduled to not to test in QM campaign
Susceptibility to DC changes in the VG2 and VG3 temperatures	RAA_THV	All	Calculate the radiometric susceptibility to temperature variations at the interface with the intermediate and warmest V-grooves	These tests cannot be run at RCA level (because of the cryo-chamber setup); so the RAA testing is the only opportunity to measure such susceptibility, which is expected, however, to be rather small and not critical	**Desired**	Scheduled to not to test in QM campaign
Susceptibility to DC changes in FEM biases (gate 1 voltages)	RAA_ELE	At least 30 GHz	Calculate the radiometric susceptibility to voltage variations on the gate 1 line	The data come for free from the tuning test provided that the procedure script is run properly	**Mandatory**	Done on 44 GHz chain with no gain and offset applied
Susceptibility to DC changes in FEM biases (gate 2 voltages)	RAA_ELE	At least 30 GHz	Calculate the radiometric susceptibility to voltage variations on the gate 2 line	The data come for free from the tuning test provided that the procedure script is run properly	**Desired**	Not done

From the summary table we see that all the mandatory tests were performed apart from the following exceptions:

- the PID controllers of the cryochamber thermal stages were not finely tuned. The reason for this was the non-nominal thermal behaviour of the cryochamber both in terms of temperature levels and temperature stability. More details about the LFI cryofacility can be found in [AD2].
- The impact of this non nominal temperature stability on the radiometric tests has caused uncertainties in the determination of some of the radiometric properties. A data analysis activity has then been performed to remove this effect from the data by correlating the radiometric with the temperature sensor data. The results of this analysis is discussed in Sect. 5.2).

In the following table we summarise the results of the various tests in terms of PASSED/NOT PASSED. A test is considered passed if the results are understood and consistent (where applicable) with the results obtained at RCA level.

IMPORTANT NOTICE. During the instrument test campaign the following functionality problems were encountered (more details about these problems can be found in [AD5]):

- the 30 GHz chain could not work in unswitched conditions: therefore all the `UNC` (i.e. unchopped) tests were not run for this chain;
- the 70 GHz chain LFI18 did not work properly, in the sense that both the radiometer legs showed virtually zero isolation. None of the radiometric tests could therefore be run on this chain.

For simplicity we will not consider the LFI18 chain in determining the status of each test.

Table 2: Summary of tests results

Test	**Acronym**	**RCAs**	**Result**	**Notes**	**Remedial actions**
FUNCTIONALITY					
Radiometric functionality	N/A	All	PASSED with exception of 70 GHz LFI 18		
Cryo chamber thermal stability verification	N/A	N/A	NOT DONE	Intensive effort to reach “operability conditions”. However: stability and coupling not optimised	Work is ongoing to identify and remove sources of thermal instabilities and couplings, as well as to reach the required temperature on the focal plane.
TUNING					

Tuning of DAE parameters	RAA_TUN	ALL	PASSED	The test was run only on the 44 GHz channel to increase flexibility in the data analysis	
Tuning of LNA gate 1 Voltage	RAA_TUN	At least 30 GHz	PASSED		
Tuning of REBA parameters	RAA_REB	ALL	Quantisation noise inconsistent with expectations.	The data stream that were acquired in the nominal mode 5 (compressed and quantised) showed a reconstruction error that was much higher than expectations. Some software problems have been identified in the TQL/TMH code that partly explain the observed behaviour	Detailed tests have been run (Dec 2005) to validate the TQL/TMH software; data analysis is in progress and will be discussed in a dedicated technical note.
RADIOMETRIC PERFORMACE TESTS					
Noise temperature, calibration constant, linearity, isolation, offset	RAA_TNG, RAA_LIS, RAA_OFT	ALL	PASSED		
Noise properties	RAA_STn, RAA_UNC	ALL	PASSED		
RADIOMETRIC SUSCEPTIBILITY					

Susceptibility to Front end temperature variations	RAA_THF	ALL	Not conclusive	The results obtained from this test were strongly limited by the thermal limitations in the cryofacility. Therefore the test itself did not present major problems but the data were not suitable for an analysis at the required level of precision	Apart from improving the hardware performace of the cryofacility, during the flight testing phase the test should be conducted in order to maximise the response of the instrument to thermal fluctuations, i.e. by increasing the sky-reference input offset and by running the test according to the same procedure used at RCA level (at least three steps followed by stabilisation).
FPU thermal response to dynamic temperature variations	RAA_THF	N/A	Not conclusive	The test was performed with a step-change in the FEU temperature istead of using sinusoidal temperature variations. This was done because of schedule limitations. From the analysis of these data it has not been possible to reconstruct the thermal damping expected from the thermal model. This has been uderstoom by furhter analysis (detailed in Sect. 9) that has demonstrated that a step change is a procedure not suitable for this kind of test.	In the flight tests we will induce sinusoidal temperature variations in the FPU to characterise the thermal damping at the various frequencies.

Susceptibility to back end temperature variations	RAA_THB	ALL	PASSED	In this case it was not run a specific test but the data from the ST1_0002 test were used, as these data (as all the data acquired during the QM campaign) were characterised by back-end thermal instabilities.	
Susceptibility to bias voltage fluctuations	RAA_ELE	ALL	PASSED	This test has been performed on the 44 GHz LFI24 with no DAE gain and offset applied.	

1.3 Achievements and limitations

1.3.1 Summary of main achievements

The testing phase of the LFI QM turned out to be a tough exercise, as for the first time numerous hardware and software sub-systems have been interfaced in a very complex cryogenic environment. The major achievements can be summarised in the definition of a consolidated test procedure, in the development of a higher level of confidence in the various subsystems and in an acceptable of the radiometric properties measured at RAA and RCA levels.

Here follows a more detail list of these achievements:

- Consolidated test procedures and data analysis
  - An automated tuning procedure has been set up to quickly explore a wide range of bias settings;
  - We have demonstrated the possibility to use temperature transients to perform quasi-stationary analyses to determine the basic radiometric properties and the susceptibility to temperature variations (FEU - BEU). This will allow an optimised planning of the flight testing phase;
  - We have successfully interfaced and synchronised the data acquisition system of the cryofacitily with the instrument scientific and housekeeping acquisition. This allows to have both the instrument and the cryofacility data in an uniform format and immediately available for data analysis;
  - The data analysis software LAMA (Lfi Array Measurements Analyser) has reached a maturity level to be routinely used in the data analysis process. This software will be used throughout the testing phase of the flight model.
- Acceptable agreement of basic radiometric properties measured at RAA level with those measured at RCA level, taking into account uncertainties deriving from the different experimental conditions.
- Generally good agreement on noise properties. In particular:

- Very good agreement for LFI28 (30 GHz) in the noise properties measured at RAA level with those measured at RCA level.
- For the 44 GHz LFI23 we could not perform such comparison as in the RCA we could not resolve the white noise properly; an internal consistency check on the RAA data, however, has shown that in this case the noise was properly resolved.
- For the 70 GHz LFI23 the noise properties measured at RAA level matched acceptably with those measured at RCA level, taking into account the uncertainties deriving from the the following facts:
    - the RCA tests were conducted in a completely different test setup, with representative waveguides and without the DAE breadboard;
    - the bias conditions in the RAA were different from those provided by the Finnish team because with the provided biases it was not possible to obtain a voltage output large enough to perform the tests in the RAA.
    - the noise has not been resolved properly because of the DAE gain and offset settings (that were set to 1 and 0, respectively). Therefore we believe that the bandwith performances of this receiver could be even better than those quoted in this measurement and that the measurements performed during the RCA tests could be dominated by the noise of the data acquisition chain.

- The activity has also helped to identify problematic areas in the cryogenic setup that are currently being addressed (in particular the high absolute temperature of the FPU and the instability of the BEU temperature).

1.3.2 Summary of main limitations and problem areas

Although the activity has been successful on many fronts many have been the limitations that have not allowed a completely successful completion of the performace tests. These problems mainly belong to three categories: (i) limitations of the thermal setup, (ii) problems in the data acquisition chain and (iii) problems identified from the radiometric output. All these problems are currently being analysed; dedicated reports will be issued covering the performed activity and the obtained results.

Here follows a more detailed description of these problems.

- Limitations of the thermal setup.
    - **FPU temperature too high**. In fact the temperature of the LFI focal plane could not reach values less than ~ 25 K, i.e. about 5 K above the required temperature. This implies a noise temperature which is expected to be few K higher than in the RCA measurements. The reason for this behaviour has then been understood to be in a too high thermal resistance of the thermal straps and in non-nominal cooling performaces of the 20 K cooler provided by CSL. We believe that both these limitations will be overcome in the flight testing phase.
    - **BEU temperature fluctuations**. These fluctuations were of the order of 2 K peak-to-peak on a 24 hrs period. The origin of this istability is still unclear. There have been three main impacts of this instability on the radiometric measurements: (i) difficulty in measurement of radiometer isolation (the change in reference load voltage is not caused only by the lack of isolation but also by the BEM temperature variation), (ii) the noise temperature (the change in BEM temperature affects the change in the radiometric voltage output), (iii) the noise properties (in particular the knee frequency is affected by this instability). See Sections 5 and 6 for more details.

  - **Not proper tuning of PID controllers**. The non nominal behaviour of the cryofacility and, in particular, the BEU temperature fluctuations that propagated to almost all thermal stages, made a precise tuning of the temperature controllers impossible. This resulted in a temperature environment that was not stable enough for a precise characterisation of the radiometric stability.

- Problems in the data acquisition chain
  - **Missing packets**. We have observed in almost all the tests packets missing from the telemetry data because of a bug on the TMH time check. This bug has been subsequently found and fixed.
  - **Swapping of sky and reference data in some channels**. For each radiometer some of the channels have the sky-reference identification of the data which is inverted. We have understood that this problem is already present at the level of the packet in SCOS2000, therefore it is likely to be originated by the REBA. The precise source of the problem, however, has still to be understood. During data analysis we have implemented the possibility to swap the channels with wrong identification.

- Problems identified from the radiometer output
  - **70 GHz LFI18 not working**. During all the tests the output of the 70 GHz receiver LFI18 showed a complete non-isolation.
  - **70 GHz LFI23 noise spectrum with spikes**. Several spikes have been found in the noise spectrum of the 70 GHz RCA. This is an open and well known problem also for what concerns the flight receivers at this frequency. We do not discuss in detail this issue here as it is widely treated in the context of the 70 GHz tiger team and is summarised in [**?**].
  - **30 GHz non working unswitched**. Due to a malfunction in the command to the phase switches, it was not possible to stop the 4 KHz switching in the LFI28 RCA. Therefore for this chain it was not possible to acquire data in unchopped state.
  - **44 GHz meaningless radiometric parameters in channel B, investigation reported in [RD5]**. In the LFI24 RCA the calculated radiometeric parameters are unreasonable channel B. Also the noise temperature of channel A is strangely high although not totaly unreasonable ($T_{\rm noise} \sim 50K$). Deeper analysis of the acquired data revealed that there has been a problem in the DAE gain setting for this channel. In practice the value of the gain that was quoted in the housekeeping data was about 400, which was inconsistent with the value reported in our logbooks (16) and with the value that was possible to derive directly from the data, which was 6. Correcting the data with a gain value of 6 fixed the problem and the data analysis was meaningful also for this channel. The origin of the problem has not been fully understood. A thorough testing of the data acquisition chain will be performed to reduce the risk of such inconsistencies during the fligt testing.

1.4 Lessons learned and actions for the flight testing phase

The testing activity performed on the qualification model of the LFI instrument and the many problems encountered and solved have taught important lessons and guidelines that will be followed during the calibration and testing activity of the flight model. Also in this case we can identify three main areas: (i) thermal, (ii) data acquisition chain and (iii) radiometers.

- Thermal issues
  - **Cryo-chamber dry run**. A detailed and thorough dry run of the cryo-chamber before loading it with the LFI instrument is key to understanding its performances and limitations (note that this was foreseen also for the QM but was heavily reduced for schedule pressure). This activity is ongoing right now.
  - **Thermal testing and PID tuning**. Enough time must be dedicated to testing the cryofacility with the LFI instrument in nominal working conditions in order to properly tune the PID controllers and guarantee the necessary stability.
  - **Temperature sensors**. More temperature sensors will be installed in the cryofacility to monitor accurately the sky load and the reference load temperatures (currently there are two temperature sensors on the back metal plate of the sky-load, one sensor on the ECCOSORB side of the sky-load and two sensors on the HFI-dummy to monitor the reference load temperature).
- Data acquisition issues
  - **Back end acquisition noise**. A dedicated test must be performed with the LFI front-end in OFF state in order to properly characterise the level of the data acquisition noise, to be sure it does not dominate the radiometer noise.
  - **Data consistency check**. A check of the consistency and integrity of the telemetry packets saved by SCOS2K and by the TQL software must be done before starting the testing campaign.
  - **Check of analog DAE output**. Before closing the cryo-chamber enough time must be dedicated to check the analog outputs of the DAE (bias lines and scientific outputs) to verify the correct response to telecommands (i.e. verify that if a certain bias value is set on a certain line by a telecommand on SCOS2K this is actually what happens) and the consistency between the DAE and REBA scientific outputs.
- Radiometer issues
  - **Channel identification**. The mapping between the DAE bias outputs and the radiometer bias inputs must be thoroughly checked and the correspondence with the RCA verified.
- Test procedure issues
  - **Susceptibility to thermal fluctuations**. Even in a thermal environment with a good thermal stability it is necessary to perform these tests maximising the instrument response to thermal variations. To achieve this the test procedure should foresee a higher temperature offset between the sky and reference temperatures and a series of at least three temperature steps followed by enough time to reach stabilisation.

1.5 Estimate of needed time and resources needed for LFI-FM ground testing

As a response to a RID raised during the IQR co-location meeting a detailed table has been sent to PSO providing a breakdown of the radiometric tests foreseen for the flight model of the LFI and an estimate of the needed resources. This information has then been harmonised with the official LFI schedule. Therefore we do not reproduce the table and estimate here in order not to generate confusion but we refer to the official LFI schedule and planning.

2 Scientific performace summary and comparison with RCA measurements

In this section we summarise the measured performances on the LFI QM instrument and where this is possible we also make a comparison with the same parameters measured at RCA level. We do not compare RAA with RCA in the following cases:

- noise properties (sensitivity, noise effective bandwidth, knee frequency and $1/f$ slope) of 44 GHz LFI24. In this case, in fact, the values measured at RCA level were not representative because the receiver noise was not resolved due to an incorrect setting of the DAE gain and offset stage.
- calibration constant of 70 GHz LFI23. In this case, in fact, the calibration constant was not reported in the 70 GHz EM test reports. Furthermore me must consider that also the other parameters must be compared with extreme caution because the receiver was tested in two very different experimental conditions (in particular waveguides were different, data acquisition setup was different and the bias conditions were very different).

Note. As discussed before, the correspondence between channel labels in the RCAs do not always correspond to the same labels in the RAA. In the following figures we use the A, B, C, and D labelling used in the RAA and compare them with the same physical channels in the RCA.

The quoted basic performace parameters have been calculated for the following conditions:

- sky-load sensor on the sky-load back metal plate; this has been considered to be more representative of the sky load temperature with respect to the sensor placed on the side of the ECCOSORB pyramid bed as we expect a smaller temperature gradient between the plate and the centre pyramids compared to the gradient between the ECCOSORB side and the centre (this has been shown to be true in the sky load used in the RCA tests). In the FM tests we are evaluating the possibility to add an extra sensor to monitor the temperature of the ECCOSORB centre pyramids.
- back-end temperature fluctuation effect removed from 30 and 44 GHz data. The 70 GHz data were not cleaned by the back-end temperture fluctuation effect as they did not show any evident correlation with the back-end temperature sensor data.

Results in other conditions have been calculated too and are reported in this report in the relevant subsections. The effect of considering a different sky-load temperature sensor is discussed in Sect 5.1.2.

Finally, in this last issue of the summary tables we do not include the susceptibility to front-end and back-end temperature variations, as a direct comparison between RCA and RAA is not possible as the experimental conditions were not the same. The objective of this test was to verify that with the parameters used in the RCA tests the susceptibility function matched theoretical expectations. Detailed results of the analysis is presented in Sections 7.1 and 7.2.

2.1 30 GHz LFI 28

In Fig. 2 we compare the basic performances measured at RAA level with those measured at RCA level for the 30 GHz receiver LFI28. We notice how the correspondence among the noise temperature values is very good, while there is a noticeable discrepance (between 30 and 50 %) in the calibration constant and in the isolation. The nature of this discrepancy is still unclear and a full understanding would require a more thorough statistical analysis of receiver basic properties also at RCA level in the same way it has been performed at RAA level.

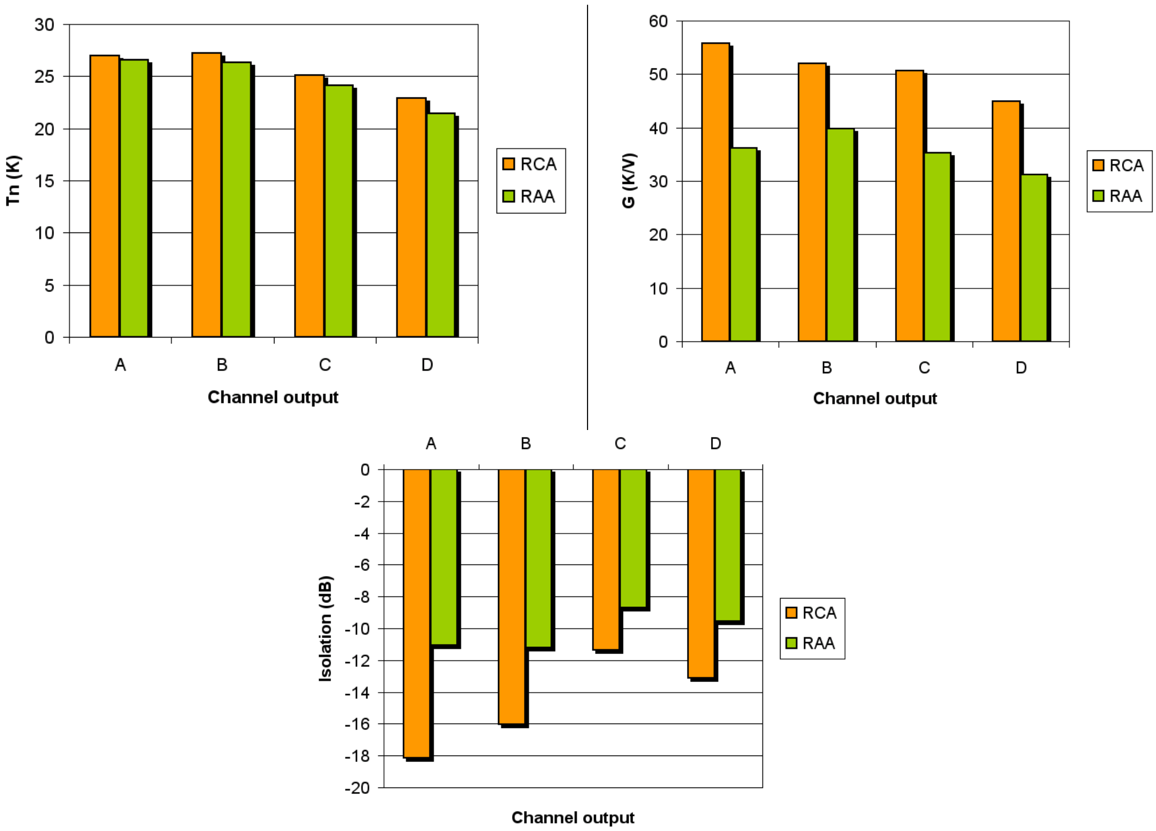

Figure 2: Summary of basic performances for LFI28: noise temperature (top left), calibration constant (top-right) and isolation (bottom)

In Fig. 3a (left) we show a comparison of the RAA-RCA white noise levels; notice that the values take into account the different phase switch blanking time (7.5 μs in the RAA and 30 μs in the RCA). In this comparison we need to consider that the experimental conditions in which the white noise was measured were different at RCA and RAA levels. In particular the sky load temperature was $\sim$ 35 K in the RAA and $\sim$ 21 K in the RCA.

Therefore in the right plot of Fig. 3 we plot the ratio $\rho = \frac{\mathrm{WN(RAA)}}{\mathrm{WN(RCA)}}\frac{(T_{\mathrm{sky}}+T_{\mathrm{sys}})(\mathrm{RCA})}{(T_{\mathrm{sky}}+T_{\mathrm{sys}})(\mathrm{RAA})}$, i.e. the ratio of white noise limits over the ratio of the sums of sky and system temperatures; this ratio should obviously be close to 1. The results presented in Fig. 3 clearly indicate a very good level of consistency between the white noise and system temperature measurements.

This consistency is also apparent in the comparison of the noise effective bandwidths (bottom plot in Fig. 3) which compare very well between RAA and RCA.

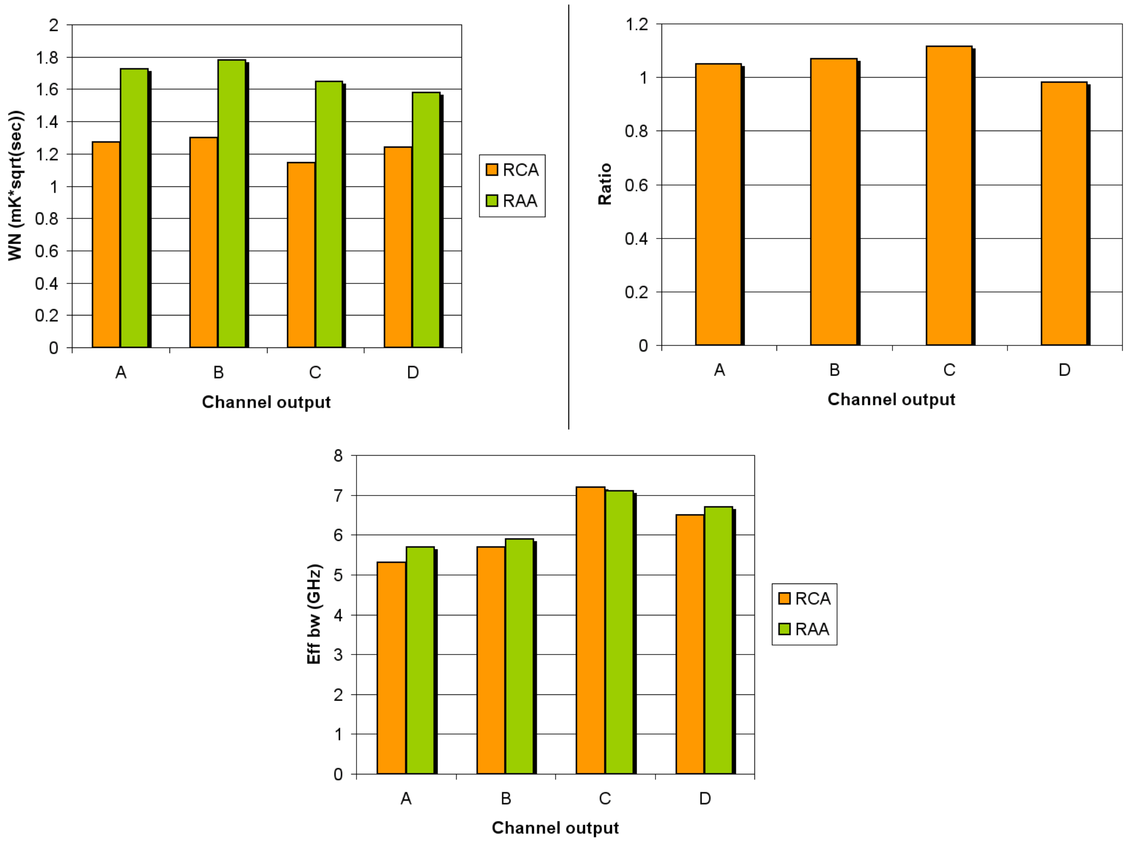

Figure 3: LFI 28 white noise properties: comparison of white noise direct measurements (left); ratio $\rho = \frac{\mathrm{WN(RAA)}}{\mathrm{WN(RCA)}}\frac{(T_{\mathrm{sky}}+T_{\mathrm{sys}})(\mathrm{RCA})}{(T_{\mathrm{sky}}+T_{\mathrm{sys}})(\mathrm{RAA})}$; effective bandwidths (bottom)

In Fig. 4 we compare the knee frequency and the $1/f$ slope calculated at RAA and RCA levels. The match is generally good (between $\sim$5% and $\sim$ 20%, with the exception of the knee frequency of channel D, that was a factor 2 higher in the RCA compared to the RAA).

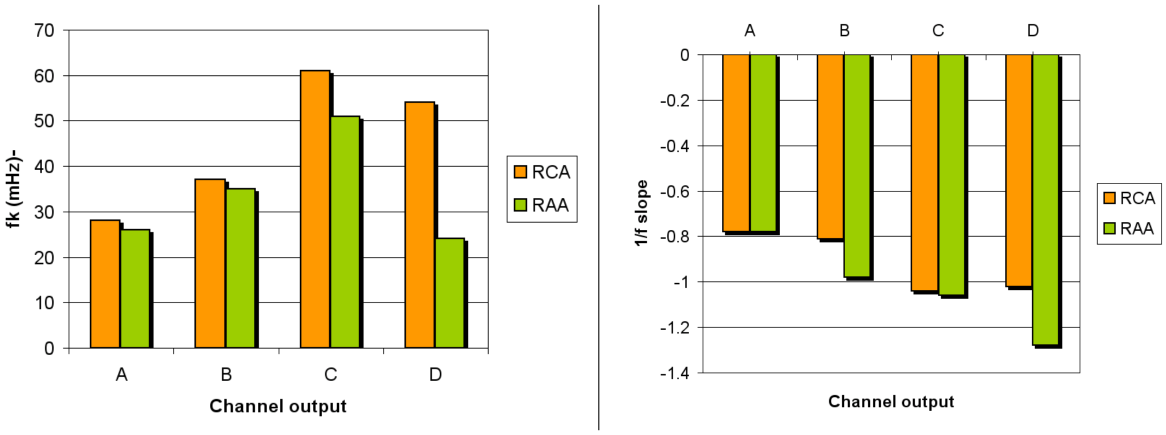

Figure 4: Knee frequency (left) and $1/f$ noise slope for LFI28 receiver.

2.2 44 GHz LFI 24

In Fig. 5 we compare the basic performances measured at RAA level with those measured at RCA level for the 44 GHz receiver LFI24. The most noticeable particular is that for channels A and B the noise temperature in the RAA is systematically higher than in the RCA. This is an effect due to the compressed output of these channels that cause an overestimation of the noise temperature calculated from the Y factor method as well as from the linear interpolation method. In the flight model testing we will improve the estimation of these properties in presence of compression in the following ways:

1. by characterising the BEM compression curve with a dedicated test and
2. by esimating the noise temperature with more sophisticated interpolations that will take into account the receiver non linear response.

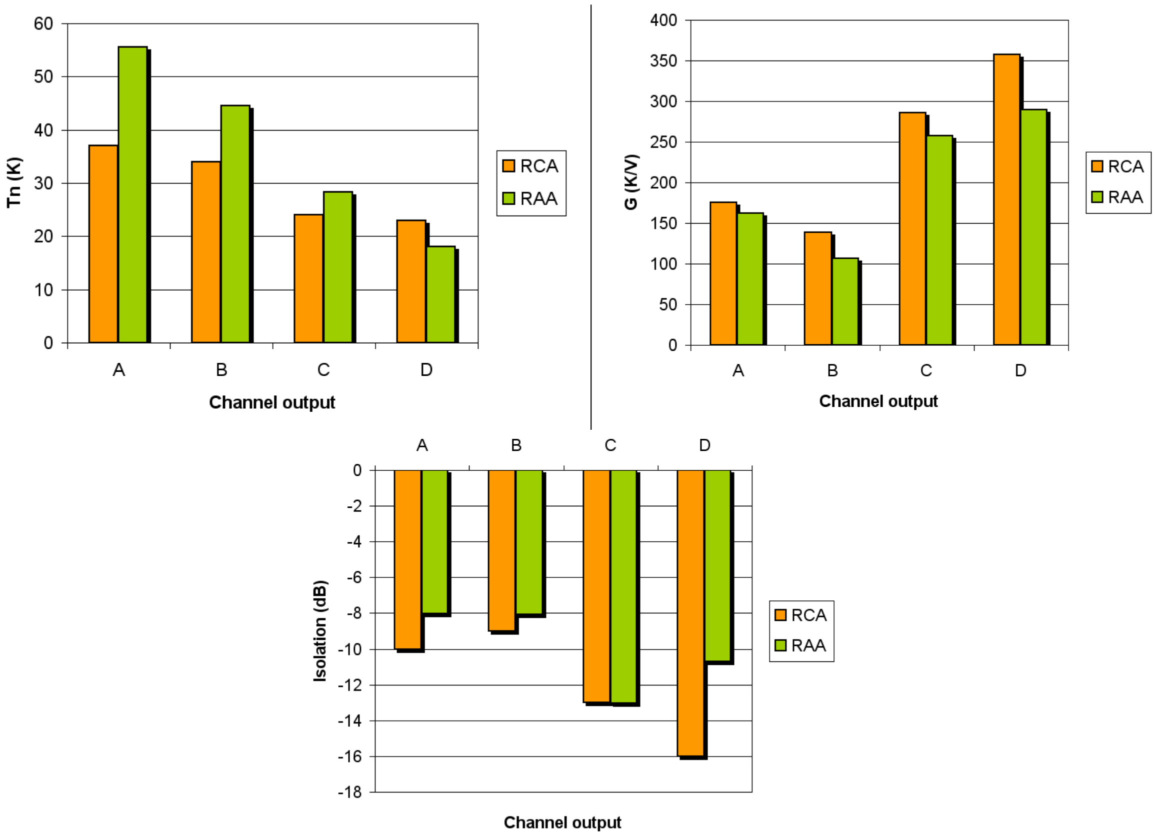

Figure 5: Summary of basic performances for LFI24: noise temperature (top left), calibration constant (top-right) and isolation (bottom)

In Fig. 6a (left) we show the noise levels and effective bandwidths for LFI24. In this case we do not provide a comparison with measurements performed at RCA level because, as already said previously, at RCA level we did not resolve the receiver noise due to incorrect settings of the DAE gain and offset stages. The results show, as expected from the FEM-BEM tests, a very low bandwidth for channels C and D, that was caused by a FEM-BEM mismatch that has been solved in the FM.

In channels A and B the bandwidth is good for channel B while is about 25% smalle than the requirement for channel A.

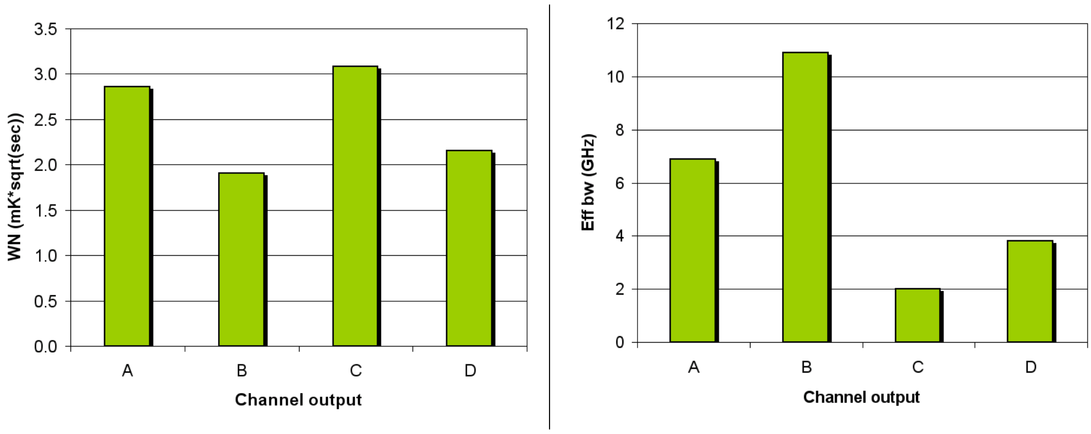

Figure 6: LFI 24 white noise properties: comparison of white noise direct measurements (left); effective bandwidths (right)

Finally in Fig. 7 we show the knee frequency and the $1/f$ slope. Also in this case we do not provide a comparison with the RCA measurements for the same reasons explained above.

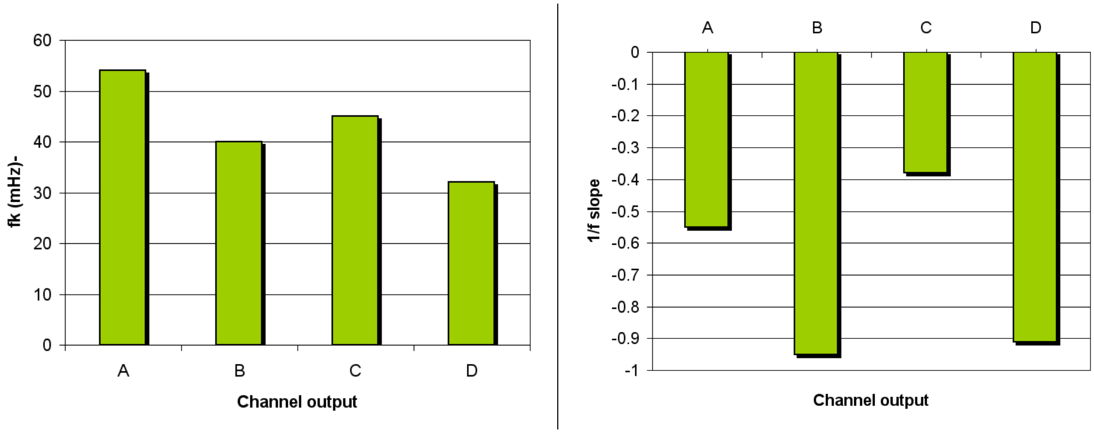

Figure 7: Knee frequency (left) and $1/f$ noise slope for the LFI24 receiver.

2.3 70 GHz LFI 23

In Fig. 8 we compare the basic performances measured at RAA level with those measured at RCA level for the 70 GHz receiver LFI23. Notice that we do not provide a RAA-RCA comparison for the photometric calibration constant because this parameter was not reported in the EM test reports. It is also important to consider that the comparison of all the other parameters between the RCA and the RAA is purely indicative as the differences between in the EM and RAA test setups and bias points makes a real quantitative comparison impossible.

Considering the limitations discussed above, the comparison of the receiver basic properties show in any case a fair match. In particular in channels C and D the match is better both in noise temperature and in isolation compared to A and B, indicating that the bias point was probably closer to the one used in the EM tests. We remind that with the 70 GHz receivers we experienced problems in reproducing the bias points that were used in the EM, essentially because of the differences in the two test setups, so that a new bias search was performed on the RAA with the objective to maximise the DC voltage output (therefore this was not a proper tuning). This problem will not be present in the FM as the 70 GHz FM RCAs are being tested with the DAE breadboard, exactly in the same way of the 30 and 44 GHz RCAs.

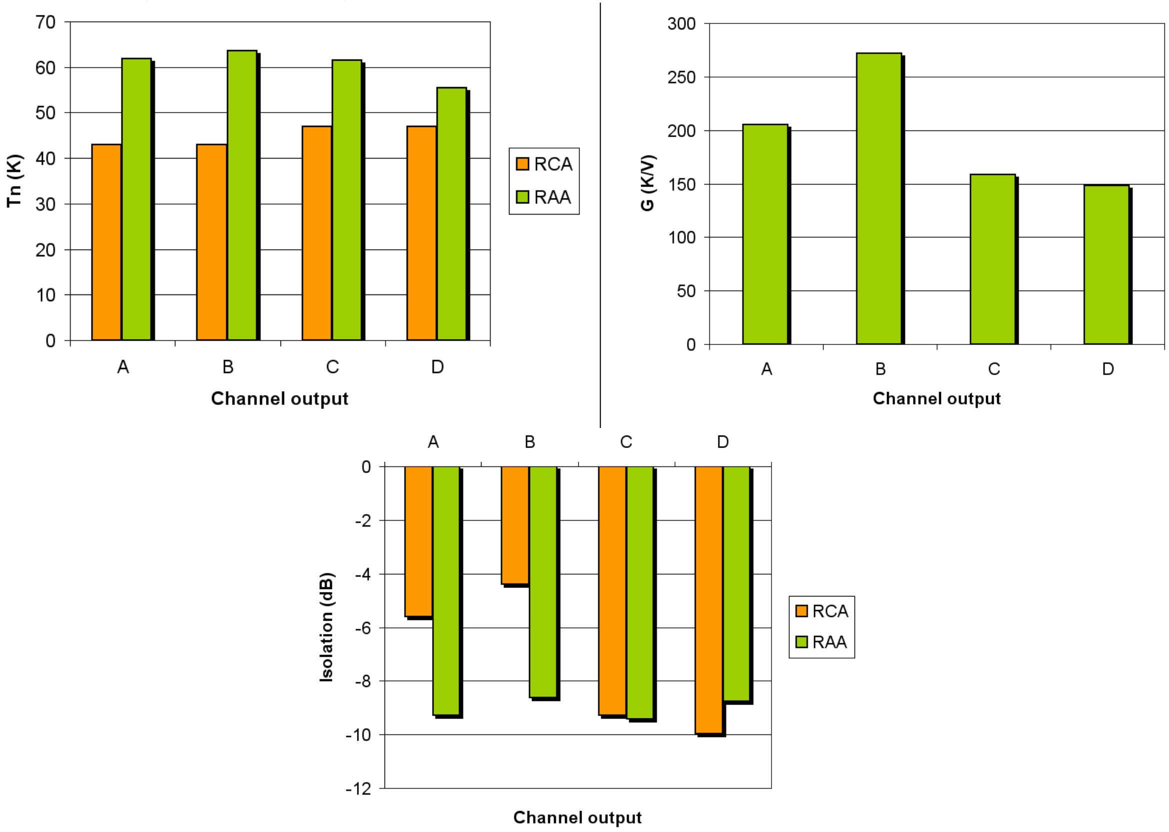

Figure 8: Summary of basic performances for LFI23: noise temperature (top left), calibration constant (top-right) and isolation (bottom)

In Fig. 9a (left) we show the noise levels and effective bandwidths for LFI23. We can notice how the RAA-RCA comparison in this case is far from being good as in the case of LFI28. It is difficult to interpret these data, given the differences in the two tests; this demostrates how it is crucial that RCA and RAA tests are run in really comparable conditions especially for what concerns the bias and acquisition systems. Again, this issue has been understood and solved for the flight model RCA tests at 70 GHz.

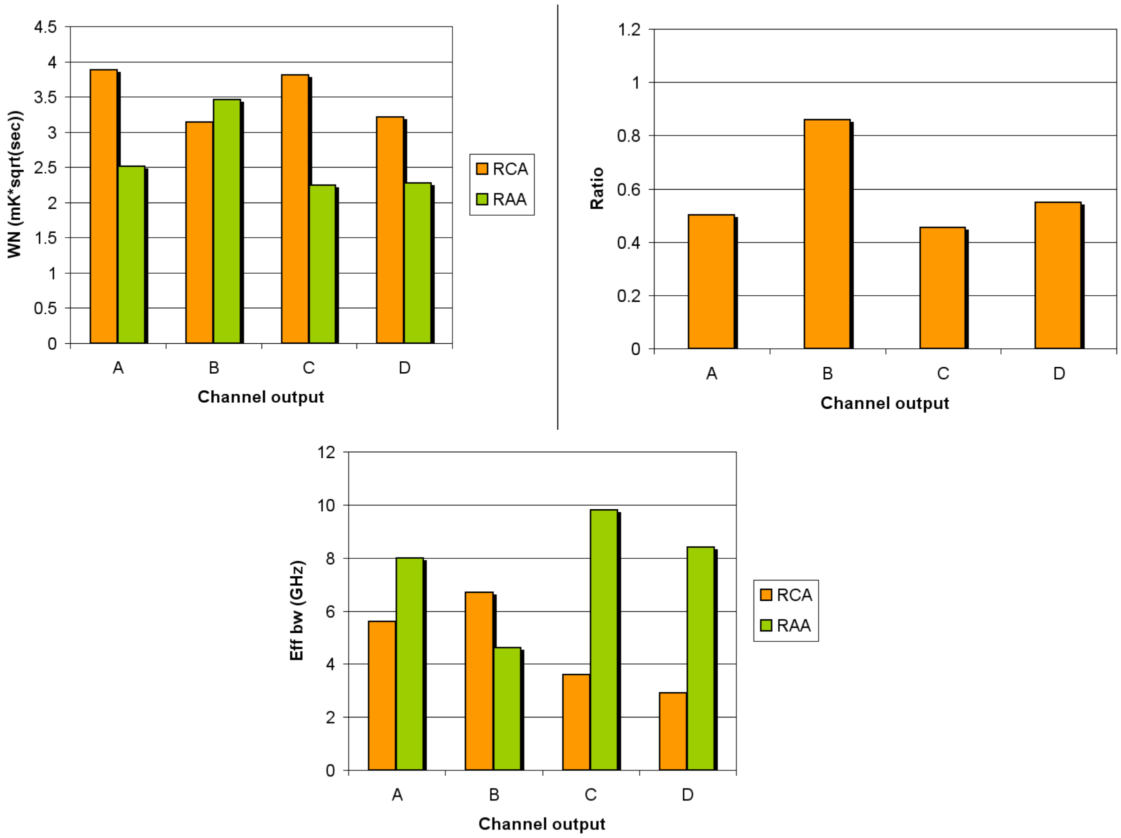

Figure 9: LFI 23 white noise properties: comparison of white noise direct measurements (left); ratio $\rho = \frac{\mathrm{WN(RAA)}}{\mathrm{WN(RCA)}}\frac{(T_{\mathrm{sky}}+T_{\mathrm{sys}})(\mathrm{RCA})}{(T_{\mathrm{sky}}+T_{\mathrm{sys}})(\mathrm{RAA})}$; effective bandwidths (bottom)

Finally in Fig. 10 we compare the knee frequency and the $1/f$ slope. The same considerations done in the case of the white noise comparison hold also for this case.

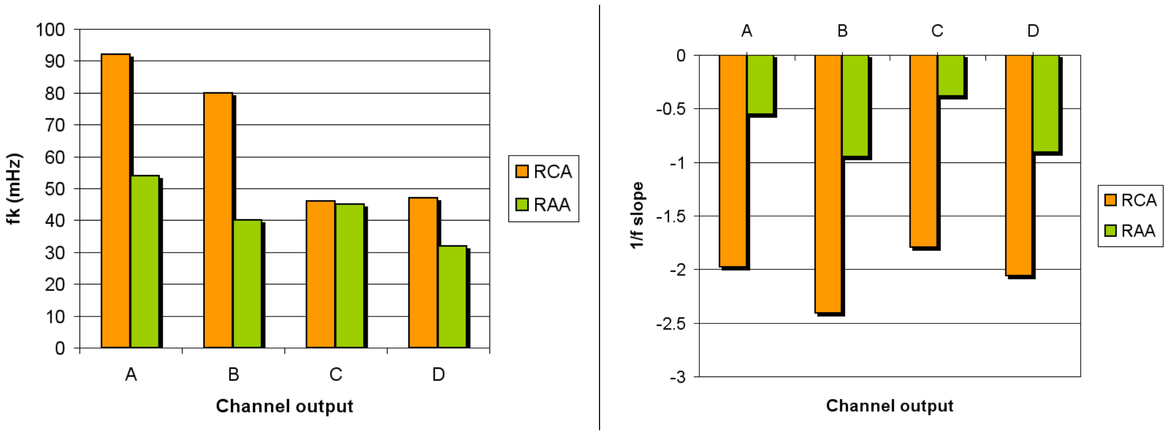

Figure 10: Knee frequency (left) and $1/f$ noise slope for the LFI23 receiver.

3 Cryofacility setup and performances

This section provides a brief description of the RAA test facility. More information can be found in [AD5]. A detailed analysis of the cryofacility performances is discussed in [RD1].

The RAA cryo-facility is based in ALENIA SPAZIO S.p.A. - LABEN. An internal view of the chamber with and without the internal shroud is shown in Fig. 11.

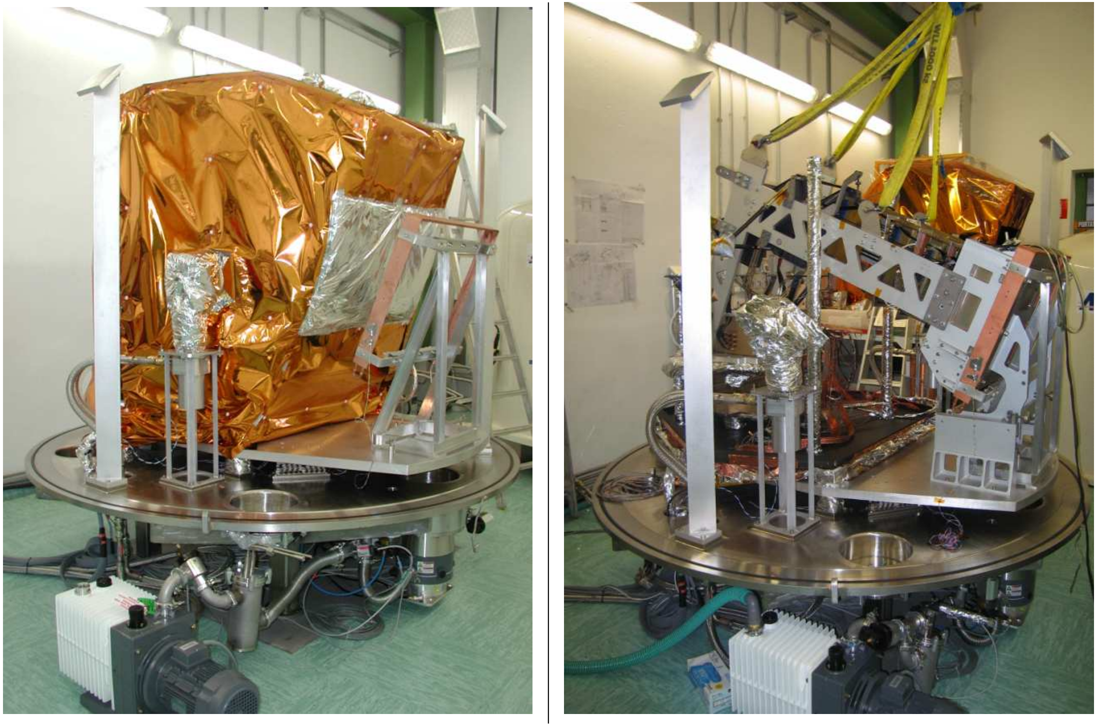

Figure 11: Left - internal view of the RAA-cryo-facility, showing the 50K internal shroud. Right - internal view of the RAA-cryofacility when the shroud is removed and during the instrument integration.

The cryo-facility is 2.5 m in diameter, sufficient to fit the whole RAA including DAE and specifically designed cryo-MGSE for supporting the instrument during testing. The RAA is directed downwards to the floor of the chamber where a cold Eccosorb load covers the complete optical field of view.

The load is attached to a 20 K dual stage helium gas cooler. A metal shroud covers the whole of the FPA and most of the waveguides and will be held at 50]K by a separate cooler. There are 3 coolers in total to give flexible cooling.

The cryo-chamber cooling curve is shown in Figures 12 through 14. The required cooling time is approximately 100 hours, including the time needed for thermal stabilization.

The cryo-chamber has 7 separate interfaces that can be temperature controlled. They are:

- Sky load (20K nominal)

- FEU (20K nominal)
- 1st V-groove (50K nominal)
- 2nd V-groove (100K nominal)
- 3rd V-groove (150K nominal)
- DAE (300K nominal)

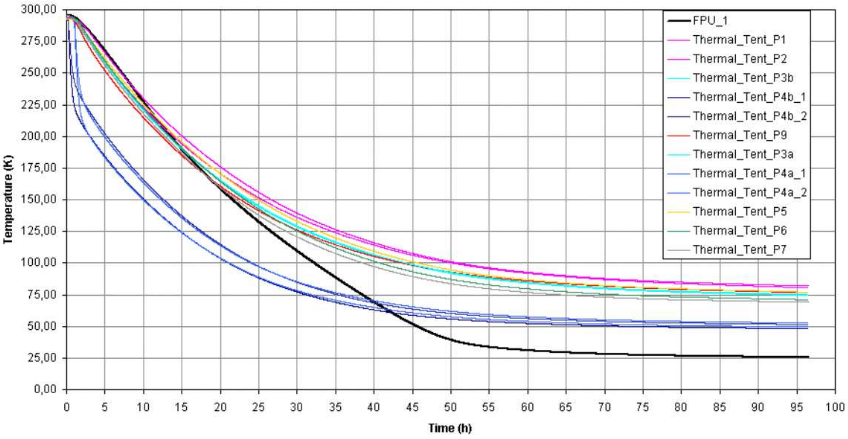

Figure 12: Measured cool-down time for the cryo-facility shroud

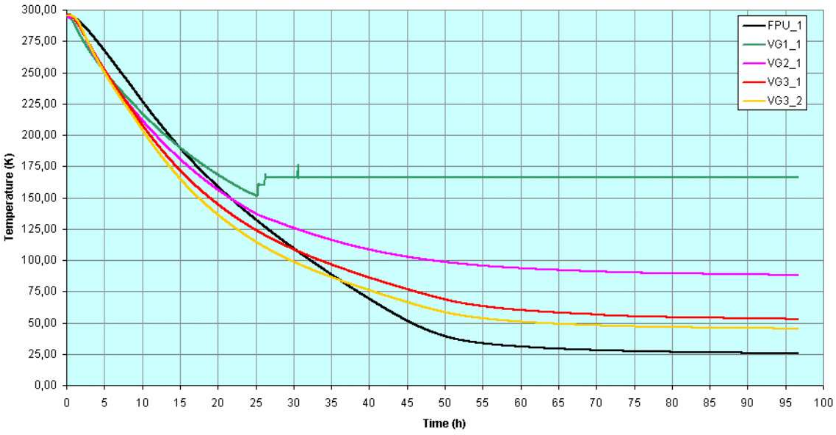

Figure 13: Measured cool-down time for the most important LFI interfaces

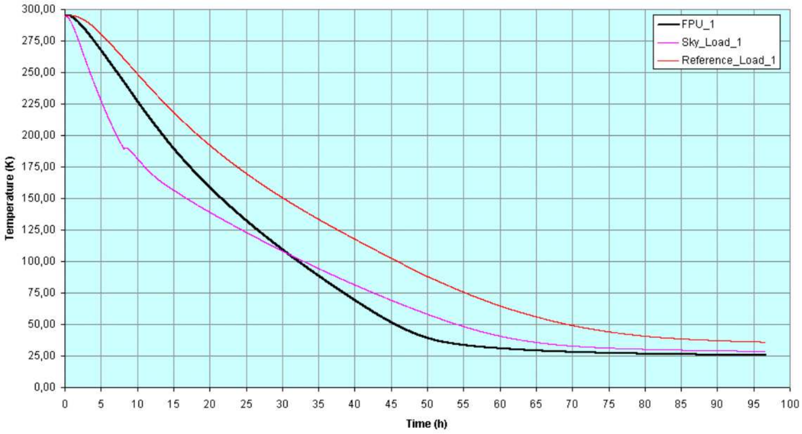

Figure 14: Measured cool-down time for sky and reference load

4 Bias settings and channel mapping

TBW

- Present a table summarising the bias settings for the three chains.
- Recall the tuning results performed on the 44 GHz chain
- Recall the tuning work done on the 70 GHz chains
- Discuss the channel mapping RAA vs RCA

5 Basic performances

In this section we report and discuss the radiometeric basic performances (i.e. noise temperature, photometric calibration, isolation, linearity and input offset) measured during the QM test campaign of the LFI instrument.

From the experimental point of view the measurement of these parameters share some common aspects, i.e.:

- the measurement requires data collected at different temperatures of one of the input loads (sky or reference load). In the tests reported here we varied the sky load temperature and maintained the reference load temperature constant;
- the calculation requires measurement of average input temperatures and average output voltages. Signal instability caused by $1/f$ fluctuations have a negligible impact on the measurement because this type of noise increases the standard deviation, introduces correlated fluctuations but does not alter the signal DC level;

- a thermal stability at the level of few mK is required for the thermal stages which have a stronger coupling with the radiometric signal (reference load, front and and back-end units). In particular slow temperature variation and drifts may change the signal DC levels introducing systematic errors in the calculated parameters.

Further details on the methods used to calculate the radiometric properties can be found in [RD4].

5.1 Experimental conditions

5.1.1 Tests used in the analysis

The instrument basic properties have been analysed using different datasets in which the sky load temperature was varied. All the data have then been considered in the analysis and the final values and uncertainties have been calculated using linear regressions as described in the following subsections.

In Table 3 we list the various tests that were used for this analysis.

Table 3: List of tests used to derive the instrument basic properties.

Test ID	Max $\Delta T_{\rm sky}$ (K)	$T_{\rm ref}$ (K)	Radiometers	Notes
ELE_0001	13.7	24.50	All	This test was performed to estimate the radiometric susceptibility to bias variations. A temperature step in the sky load was also acquired with the receiver in nominal bias conditions; data from this step have been used to calculate basic properties
LIS_0001	4.48	24.50	All	During this test the temperature rise stopped after few K and then the temperature dropped back again.
LIS_0002	1.95	24.50	All	The objective of this test was to change the sky load temperature by a much larger amount, but the scientific data acquisition stopped at the beginning of the test so that the radiometric ouput was logged only for a limited rise of the sky load temperature.
ST1_0002	10.53	24.50	LFI 28 and LFI 24 (only channels C and D)	This test was run before rebiasing the 70 GHz chain LFI23 so that the DC voltage output was vary low with respect to all the test performed after the rebiasing. Therefore these data were not consistent with the data acquired in the subsequent tests and have not been unsed in the analysis. For what concerns LFI24 we set the DAE gain to a value (24) that caused the signal output on channels A and B to saturate.
ST1_0006	3.55	24.50	All	Test in which the sky load temperature was slowly drifting

5.1.2 Temperature sensor for monitoring sky and reference load temperatures

It is well known that an uncertainty in the measurement of the temperature of the load used to stimulate the receiver has an important impact on the final values of the calculated parameters. In the RAA QM setup we have two redundant temperature sensors placed on the HFI dummy which can be used to monitor the temperature of the 4 K reference load and two temperature sensors placed on the sky load, one at the centre of the back metal plate and one on the side of the bed of ECCOSORB pyramids.

Because in all our tests we have always changed the sky load temperature, the values of the measured parameters will be dependent on the choice of the sky load temperature sensor. In the following we will present results obtained in both cases, i.e. considering the sensor on the metal plate and the sensor on the side of the ECCOSORB load.

5.1.3 Major non idealities

Two were the main problems that were econtered in these tests: (i) the instability in the temperature of the back-end unit and (ii) an instability in the BEM output of the 44 GHz receiver LFI24 that was observed during some of the tests.

This fluctuations appears to couple both with the sky load and with the thermal tent inside the cryo-chamber, which implies that the measurements performed using these data will be affected by this coupling. A software procedure to remove this effect by correlating the scientific with the housekeeping data has been setup and is now a part of the LAMA software. The details of this procedure will be described in a forthcoming technical note.

In the following we report results obtained both before and after the application of the cleaning procedure. In Fig. 16 we show, as an example, the radiometric output (LFI28 channel A) before and after the cleaning procedure.

It is worth noting that this effect was very well visible in the radiometric output of LFI28 and LFI24, but not in LFI23, as shown in Fig. 15. Therefore the application of the removal algorithm to the 70 GHz data likely worsened the quality of the radiometric data instead of improving it. Therefore the pararmeters listed in the summary tables (see Sect. 2) for this receiver have been those calculated without applying any removal algorithm.

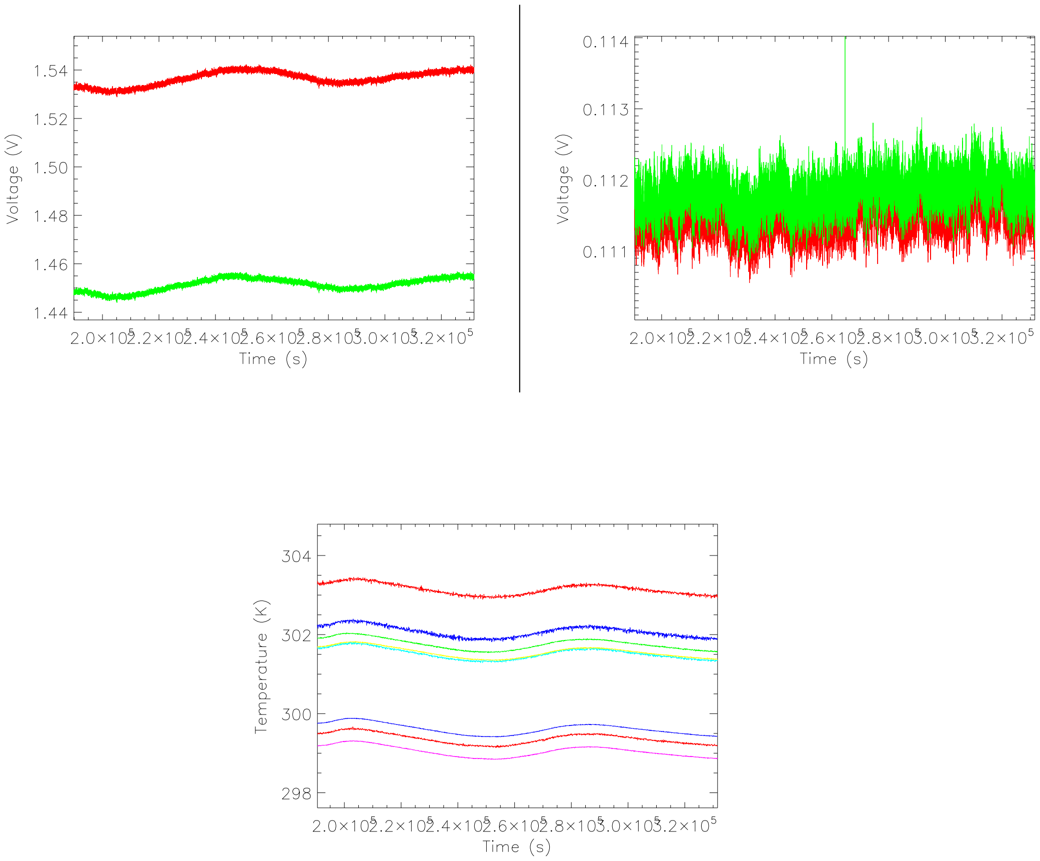

Figure 15: Effect on BEU temperature instability on radiometric output of LFI28 (channel A) compared to LFI23 (channel A). Left – LFI28 receiver output; right – LFI23 receiver output; bottom – temperature recorded by BEU sensors. Dataset was ST1_0002.

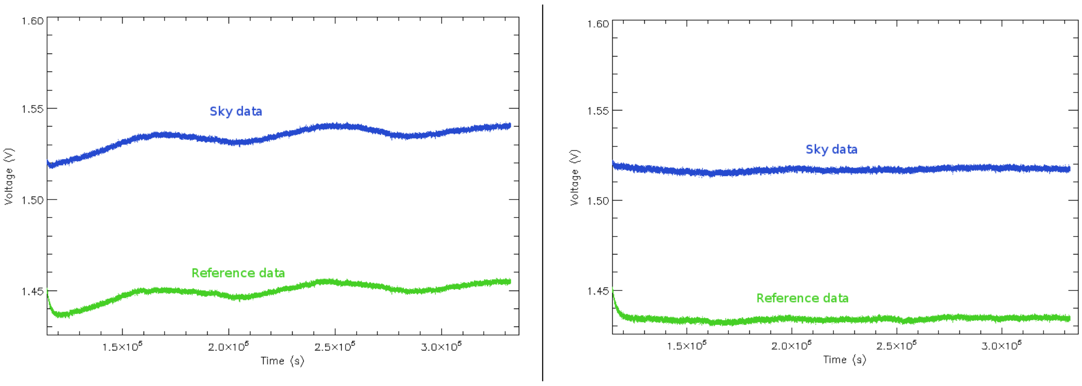

Figure 16: Radiometric data (LFI28 channel A) before and after removal of the effect of BEU temperature instability

Another problem that showed up during the tests was an instability in the BEM output of some channels in the 44 GHz LFI24 (see an example shown in Fig. 17). This problem is very likely of the same nature of the BEM instabilities observed in the 30 and 44 GHz flight BEMs, a problem which has now been understood and about to be solved.

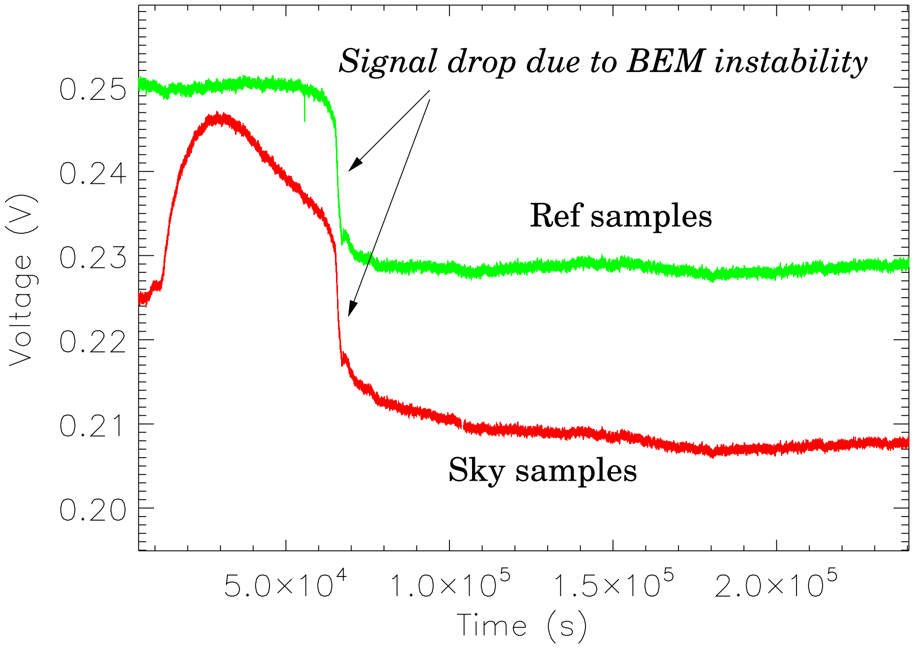

Figure 17: Istability in the BEM output of LFI24 channel C observed during the LIS_0001 test

The impact of this problem on the calculated radiometric paramteres is discussed in Sec. 5.2, where the results relative to LFI24 are presented.

5.1.4 BEM DC offset and DAE gain/offset settings

BEM DC offsets. The value of the output voltage of the BEMs have been measured with the radiometer FEMs in OFF state and subsequently removed from the voltage readings for a correct estimation of the radiometric parameters. These values are reported in Table 4

Table 4: BEM voltage outputs measured at nominal temperature conditions with the FEMs in OFF state

	BEM DC offsets (V)			
	Channel A	Channel B	Channel C	Channel D
30 GHz LFI28	0.0199	0.0193	0.0206	0.0229
44 GHz LFI24	0.0190	0.0216	0.0123	0.0249
70 GHz LFI23	0.0146	0.0220	0.0111	0.0123

DAE gain and offset settings During this test the DAE gain and offset have been set to 1 and 0 V respectively for all the radiometers apart from the 44 GHz LFI24. For this chain the gain and offset settings are summarised in the following table

Table 5: DAE gain and offset settings for LFI24

ELE_0001 start and end of test		
	Gain	Offset (V)
Channel A	1	0
Channel B	1	0
Channel C	1	0
Channel D	1	0
ELE_0001 middle of test		
	Gain	Offset (V)
Channel A	24	0.653
Channel B	16	0.857
Channel C	24	0.267
Channel D	24	0.207
All other tests		
	Gain	Offset (V)
Channel A	24	0.653
Channel B	6	0.857
Channel C	24	0.267
Channel D	24	0.207

5.2 Noise temperature, photometric calibration and isolation

In this section we present briefly the receiver noise temperature, photometric calibration and isolation in tabular form for the following cases:

1. metal plate sensor;

2. ECCOSORB sensor.

For each of the two cases we compare results with and without the BEU temperature fluctuation effect in the data. Numerical results in tabular form can be found in Appendix

5.2.1 Case 1: metal plate sensor

Noise temperature. The noise temperature has been calculated by fitting the Voltage *vs* Temperature data points for all the tests with a straight line and then calculating the intercept with the x axis as discussed in [RD4]. In Figure 18 we show the voltage *vs* temperature diagram relative for the 30 GHz LFI28 receiver (channel A) for all the datasets considering the BEU temperature instability effect present (left) and removed from data (right).

From these two figures it is clear that the data from different datasets lie on the same line and that the BEU temperature instability has a small effect in this case.

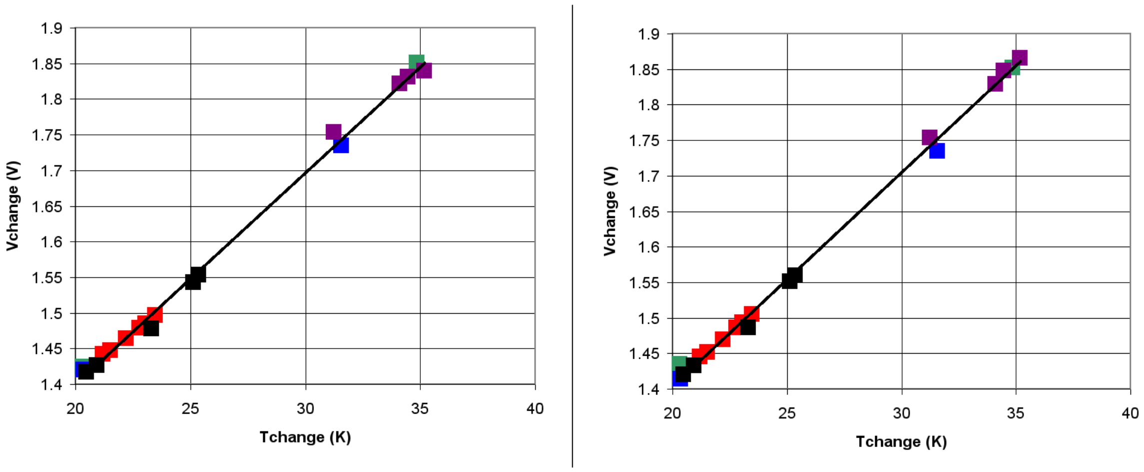

Figure 18: Voltage-temperature diagram for the 30 GHz LFI28 channel A: (left) with the BEU temperature instability present in data, (right) with the BEU temperature instability removed from the data. Different colors indicate different datasets: Green – ELE_0001, Red – LIS_0002, Blue – ST1_0002, Magenta – ST1_0006, Black – LIS_0001

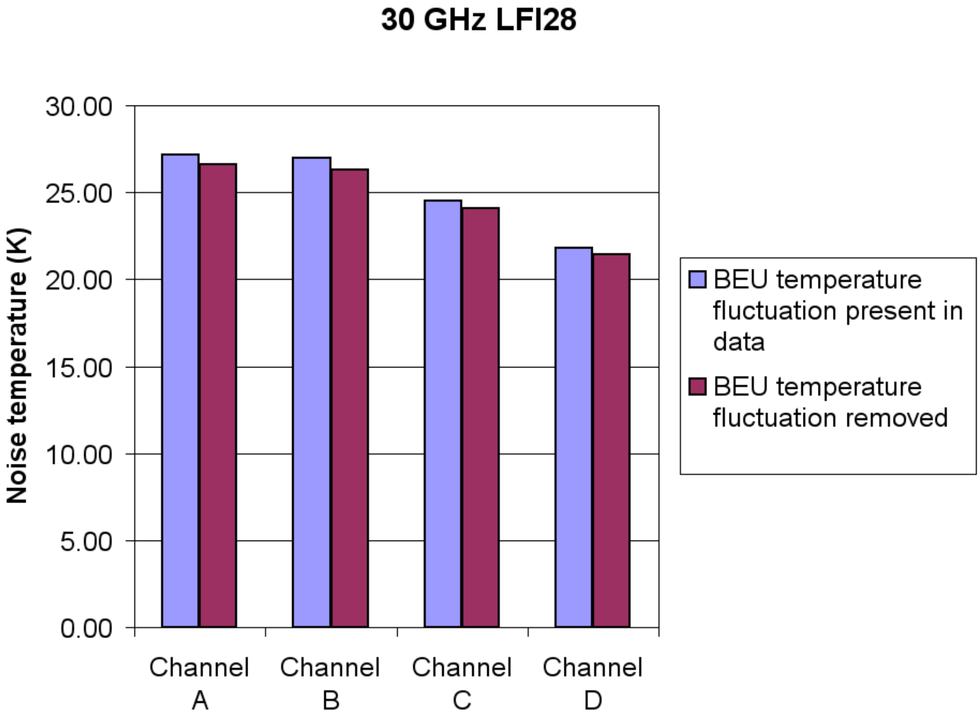
30 GHz LFI28
Noise temperature (K)
30.00
25.00
20.00
15.00
10.00
5.00
0.00
Channel A
Channel B
Channel C
Channel D
BEU temperature fluctuation present in data
BEU temperature fluctuation removed

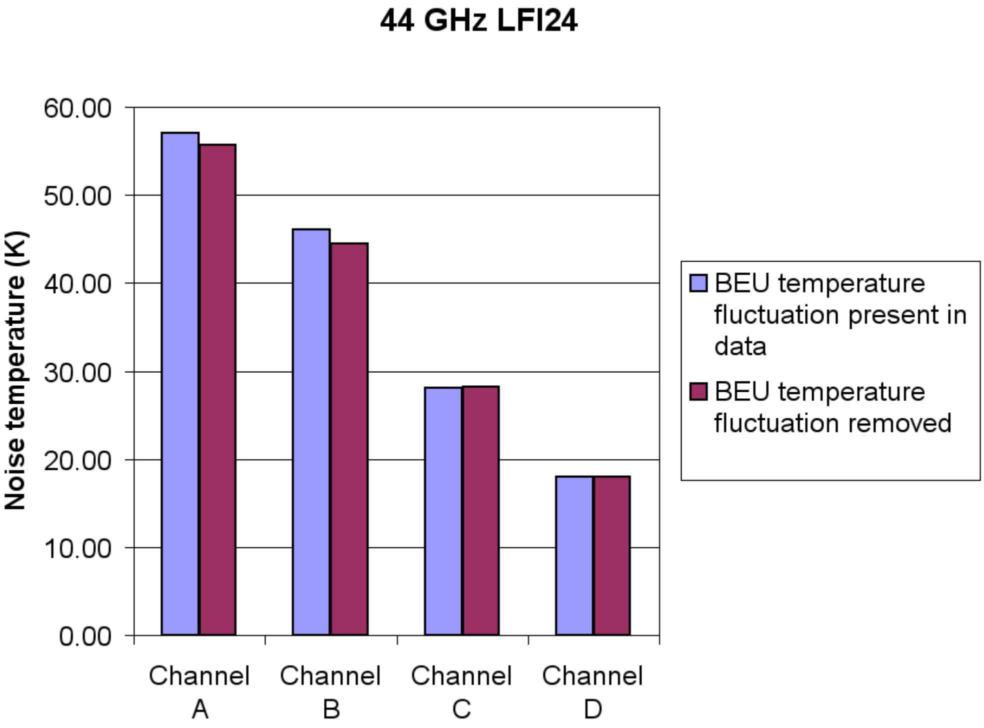
44 GHz LFI24
Noise temperature (K)
60.00
50.00
40.00
30.00
20.00
10.00
0.00
Channel A
Channel B
Channel C
Channel D
BEU temperature fluctuation present in data
BEU temperature fluctuation removed

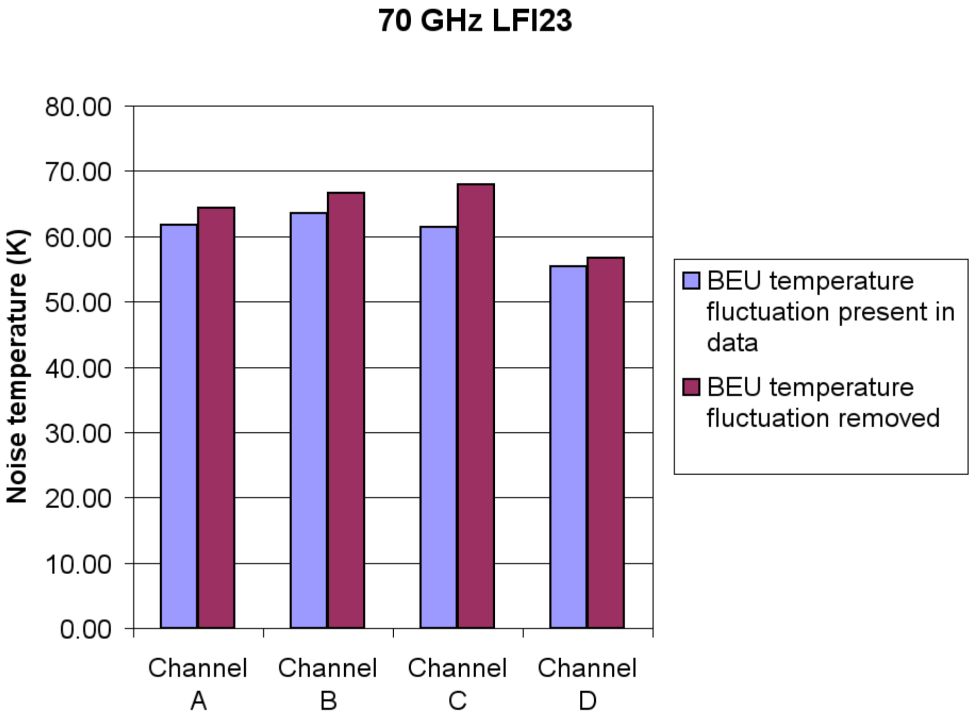

Figure 19: Noise temperatures estimated from tests listed in Table 3: (a) LFI28 - 30 GHz, (b) LFI24 - 44 GHz, (c) LFI23 - 70 GHz

The results summarised in Figures 19 indicate that the impact of the temperature fluctuations at the back-end unit level has a small impact on the noise temperature estimation.

Another result which is particularly striking is the high value of the noise temperature for channels A and B of the LFI24. In this case we already know that in these channels the radiometric output is compressed due to a too high gain in the back-end unit, therefore a linear interpolation over estimates the noise temperature, especially in these tests where the sky load temperature was increased up to ~35 K.

Finally it is worth noting that for LFI28 and LFI24 the removal of the BEU temperature instability effect improves the noise temperature estimate, while for the LFI23 the result is the opposite. The reason for this is likely the fact that the radiometeric output in this case did not trace clearly the BEU temperature fluctuation; therefore the application of the removal algorithm (which tries anyway to find a correlation between the scientific and housekeeping channels) has introduced a spurious effect which is non-physical (see also Sect. 5.1.3, Fig. 16).

Photometric calibration. The photometric calibration constant has been calculated by fitting the ΔV *vs* ΔT (where $\Delta V = V_{\rm sky} - V_{\rm ref}$ and $\Delta T = T_{\rm sky} - T_{\rm ref}$)) data points for all the tests with a straight line and then calculating the slope of the best fit line (see always [RD4]).

In Figure 20 we show the $\Delta V - \Delta T$ diagram relative for the 30 GHz LFI28 receiver (channel A) for all the datasets considering the BEU temperature instability effect present (left) and removed from data (right). The slope of this line provides the photometric calibration.

From these two figures it is clear that the data from different datasets lie on the same line and that the BEU temperature instability has a small effect also in this case.

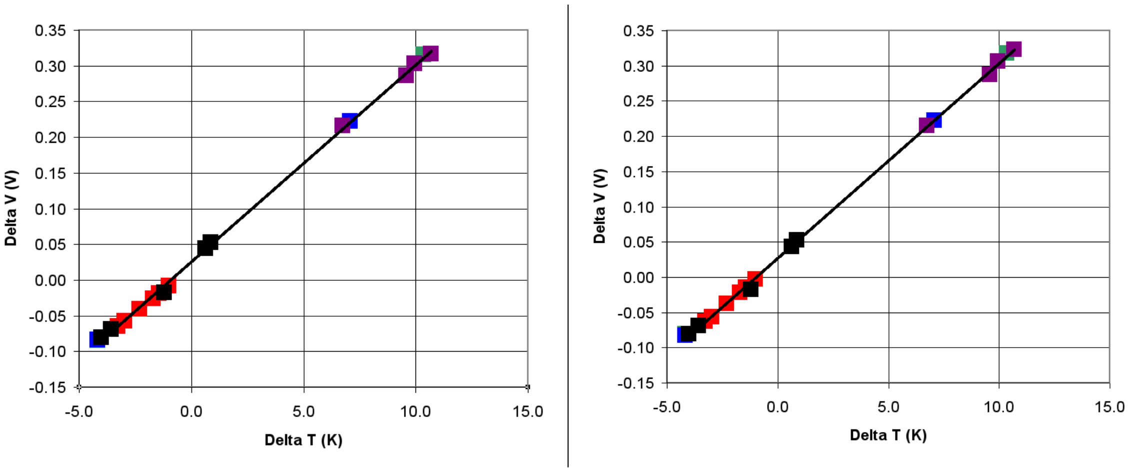

Figure 20: ΔV-ΔT diagram for the 30 GHz LFI28 channel A: (left) with the BEU temperature instability present in data, (right) with the BEU temperature instability removed from the data. Different colors indicate different datasets: Green – ELE_0001, Red – LIS_0002, Blue – ST1_0002, Magenta – ST1_0006, Black – LIS_0001

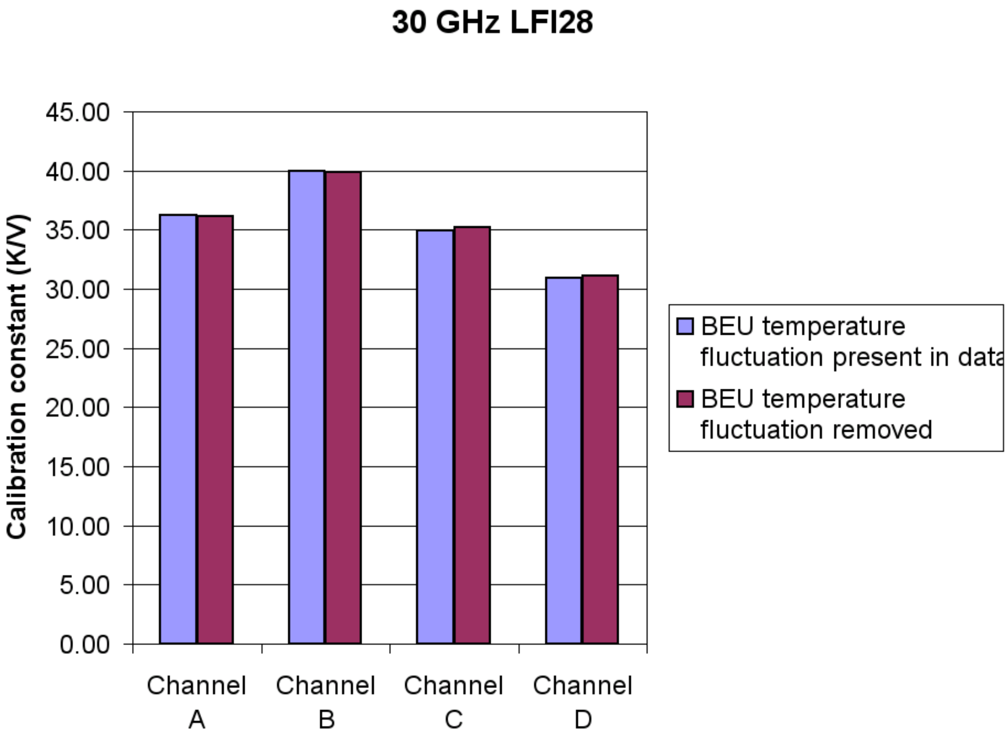

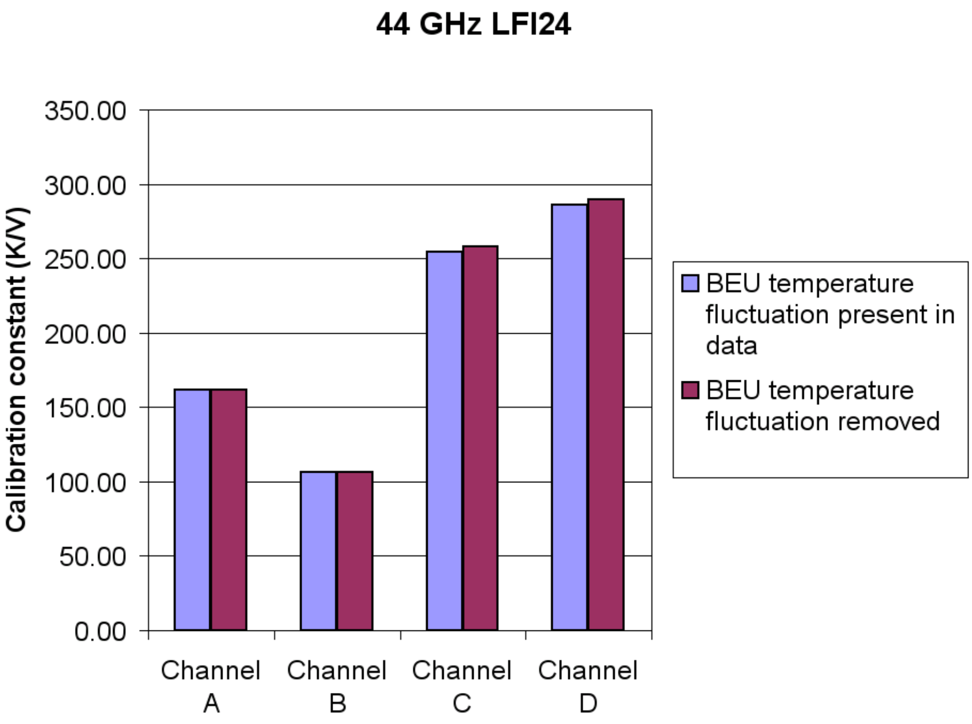
44 GHz LFI24
Calibration constant (K/V)
350.00
300.00
250.00
200.00
150.00
100.00
50.00
0.00
Channel A
Channel B
Channel C
Channel D
BEU temperature fluctuation present in data
BEU temperature fluctuation removed

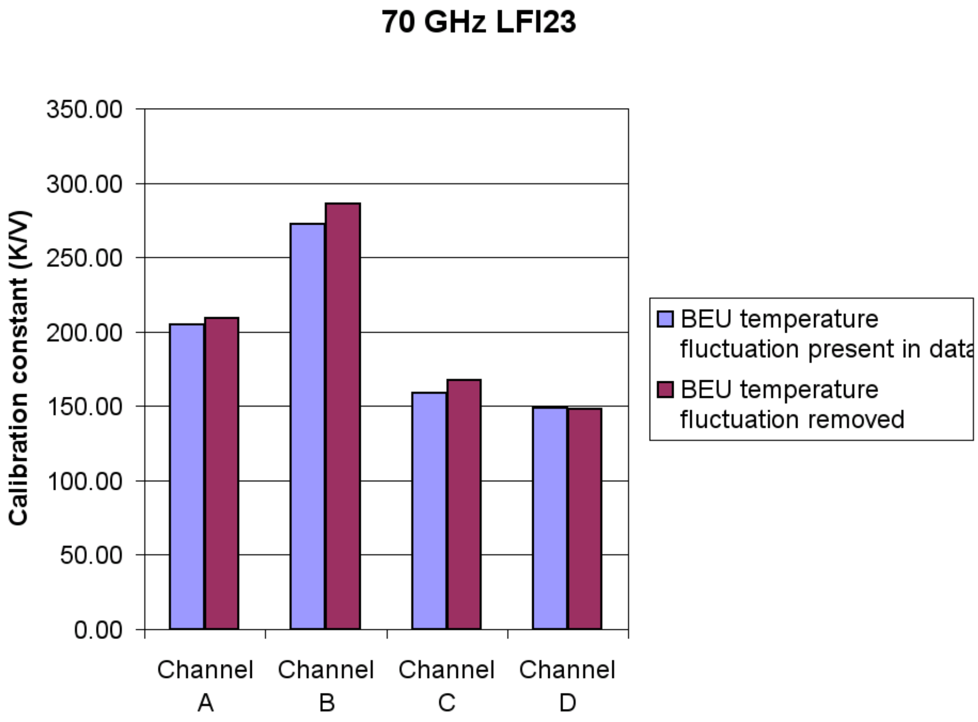
70 GHz LFI23
Calibration constant (K/V)
350.00
300.00
250.00
200.00
150.00
100.00
50.00
0.00
Channel A
Channel B
Channel C
Channel D
BEU temperature fluctuation present in data
BEU temperature fluctuation removed

Figure 21: Photometric calibration estimated from tests listed in Table 3: (a) LFI28 - 30 GHz, (b) LFI24 - 44 GHz, (c) LFI23 - 70 GHz

Similarly to the previous case, also for the computation of photometric calibration we see that the impact of the temperature fluctuations at the back-end unit level can be considered small.

Isolation. The calculation of receiver isolation is strongly dependent on the stability of the thermal environment, as any change in the voltage channel not looking at the changing temperature is interpreted as due to non-perfect isolation.

In our case the instabilities in the back-end unit temperature have limited the accuracy in the isolation calculation, especially in the tests with a small temperature change in the sky load.

To allow the calculation of isolation also in presence of back-end unit thermal fluctuations we have followed a different approach compared to the one described in [RD4]. In particular we have started from the definition of isolation reported in Equation 1 (assuming a test in which the sky load temperature is varied and the reference load temperature is maintained fixed):

$$I = \frac{\Delta V_{\mathrm{ref}} - G \times \Delta T_{\mathrm{ref}}}{\Delta V_{\mathrm{sky}} + \Delta V_{\mathrm{ref}} - G \times \Delta T_{\mathrm{ref}}} \equiv \frac{\delta_{\mathrm{fixed}}}{\delta_{\mathrm{tot}}}. \tag{1}$$

If we plot, for each measurement, δ_{fixed} *vs* δ_{tot}, then the isolation I is simply the slope of the linear best fit through the data.

In Figure 22 we show the plot δ_{fixed} *vs* δ_{tot} diagram relative to the 30 GHz LFI28 receiver (channel A) for all the datasets considering the BEU temperature instability effect present (left) and removed from data (right). The slope of this line provides the isolation.

In this case we clearly see how the scatter in the data points is reduced when we remove the temperature instability effect from the data, thus increasing the accuracy of the estimate.

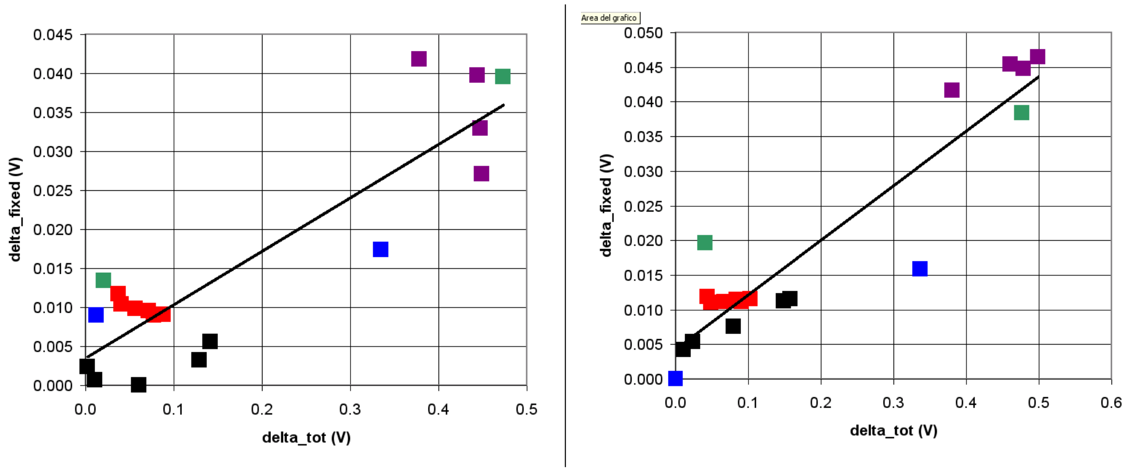

Figure 22: δ_{fixed} *vs* δ_{tot} diagram for the 30 GHz LFI28 channel A: (left) with the BEU temperature instability present in data, (right) with the BEU temperature instability removed from the data. Different colors indicate different datasets: Green – ELE_0001, Red – LIS_0002, Blue – ST1_0002, Magenta – ST1_0006, Black – LIS_0001

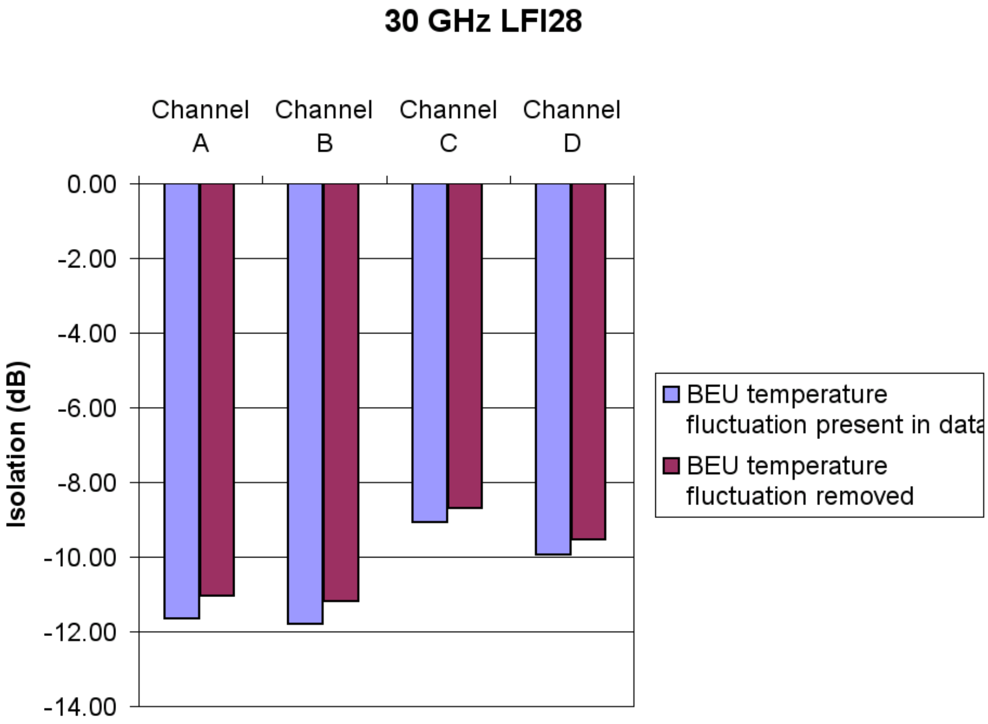
30 GHz LFI28
Channel A
Channel B
Channel C
Channel D
0.00
-2.00
-4.00
-6.00
-8.00
-10.00
-12.00
-14.00
Isolation (dB)
BEU temperature fluctuation present in data
BEU temperature fluctuation removed

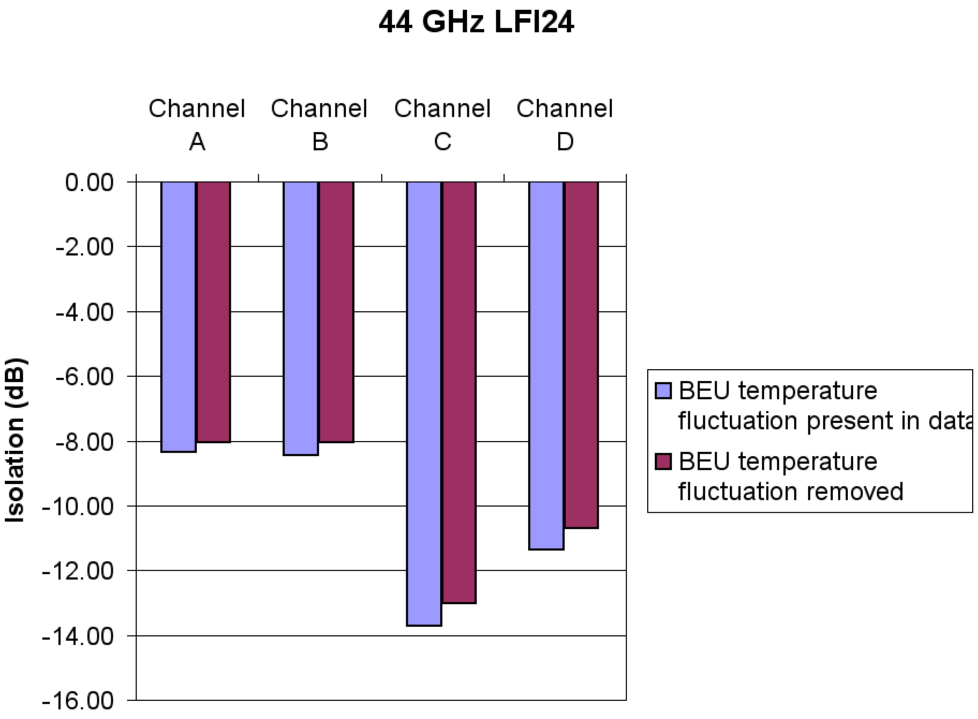
44 GHz LFI24
Channel A
Channel B
Channel C
Channel D
0.00
-2.00
-4.00
-6.00
-8.00
-10.00
-12.00
-14.00
-16.00
Isolation (dB)
BEU temperature fluctuation present in data
BEU temperature fluctuation removed

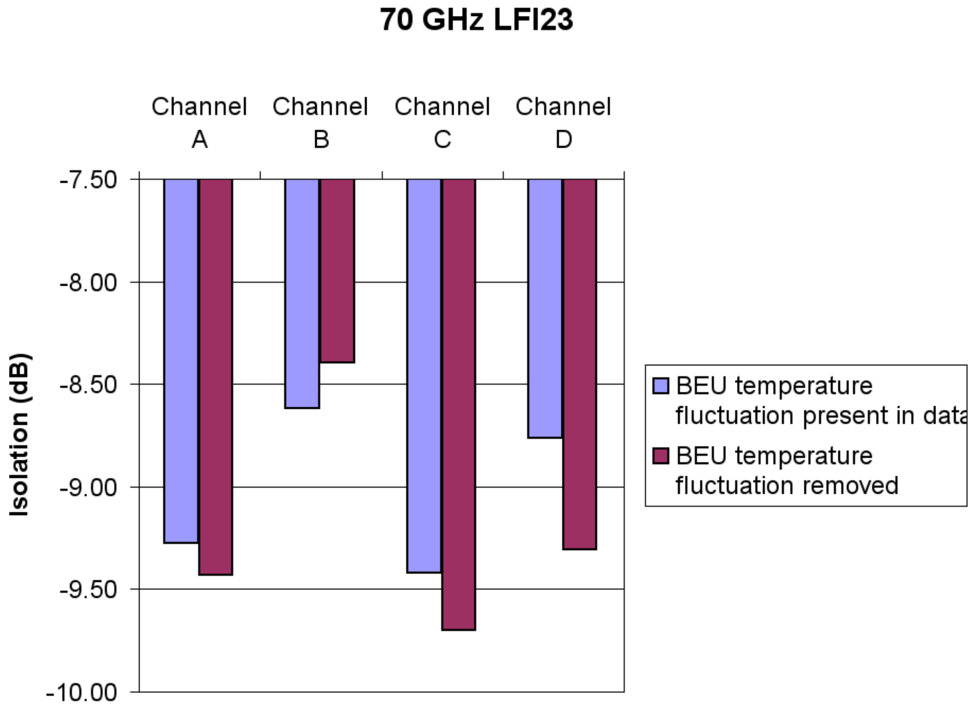

Figure 23: Isolation estimated from tests listed in Table 3: (a) LFI28 - 30 GHz, (b) LFI24 - 44 GHz, (c) LFI23 - 70 GHz

Similarly to the previous case, also for the computation of photometric calibration we see that the impact of the temperature fluctuations at the back-end unit level can be considered small.

5.2.2 Case 2: ECCOSORB sensor

Noise temperature. In Figure 24 we show the voltage *vs* temperature diagram relative for the 30 GHz LFI28 receiver (channel A) for all the datasets considering the BEU temperature instability effect present (left) and removed from data (right).

Comments similar to the previous case can be stated here: data from different datasets lie on the same line and that the BEU temperature instability has a small effect.

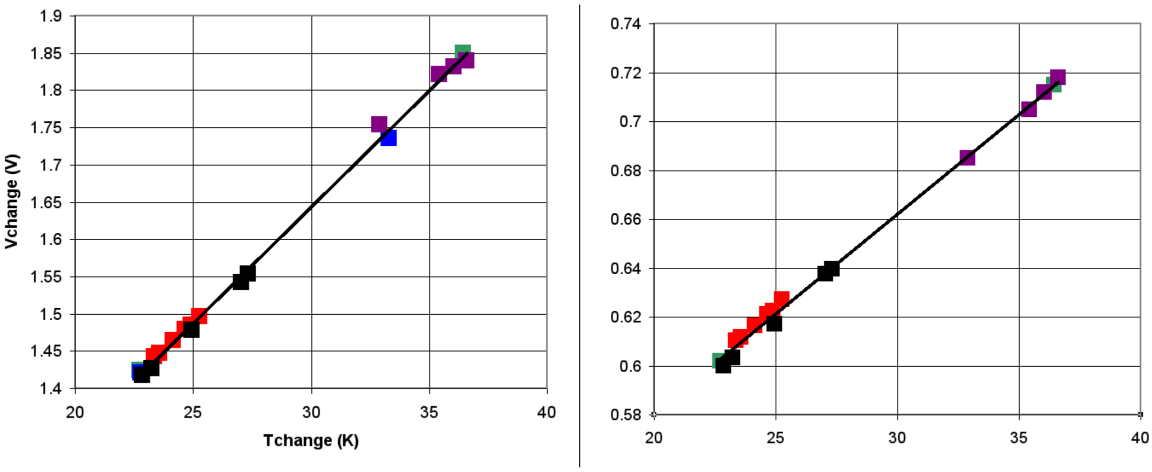

Figure 24: Voltage-temperature diagram for the 30 GHz LFI28 channel A: (left) with the BEU temperature instability present in data, (right) with the BEU temperature instability removed from the data. Different colors indicate different datasets: Green – ELE_0001, Red – LIS_0002, Blue – ST1_0002, Magenta – ST1_0006, Black – LIS_0001. Sky load temperature data from ECCOSORB sensor.

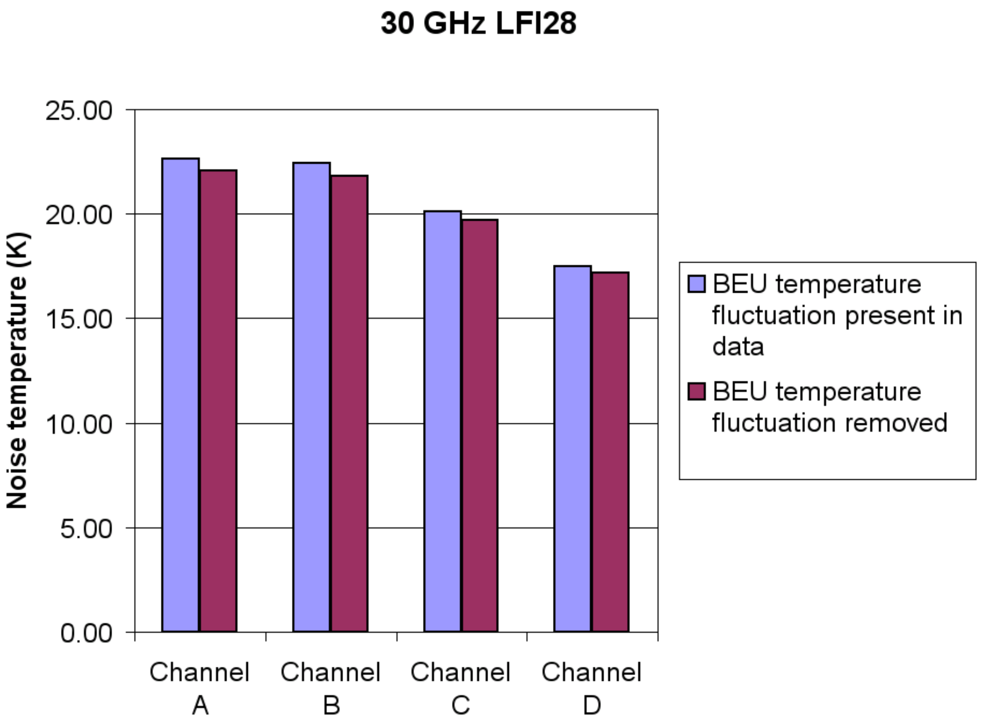

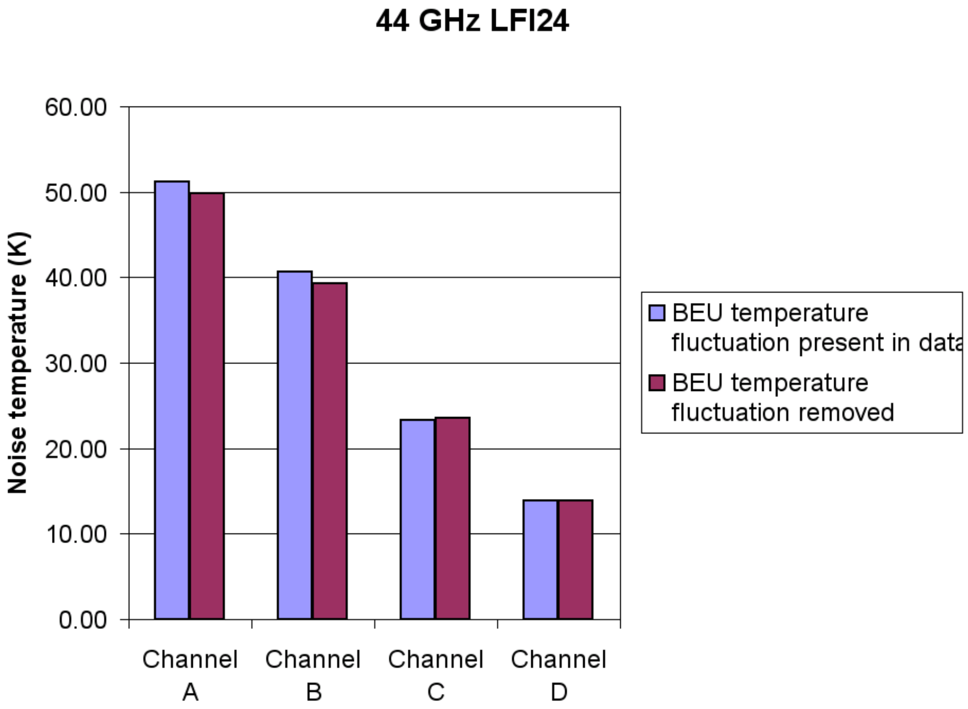
44 GHz LFI24
Noise temperature (K)
60.00
50.00
40.00
30.00
20.00
10.00
0.00
Channel A
Channel B
Channel C
Channel D
BEU temperature fluctuation present in dat
BEU temperature fluctuation removed

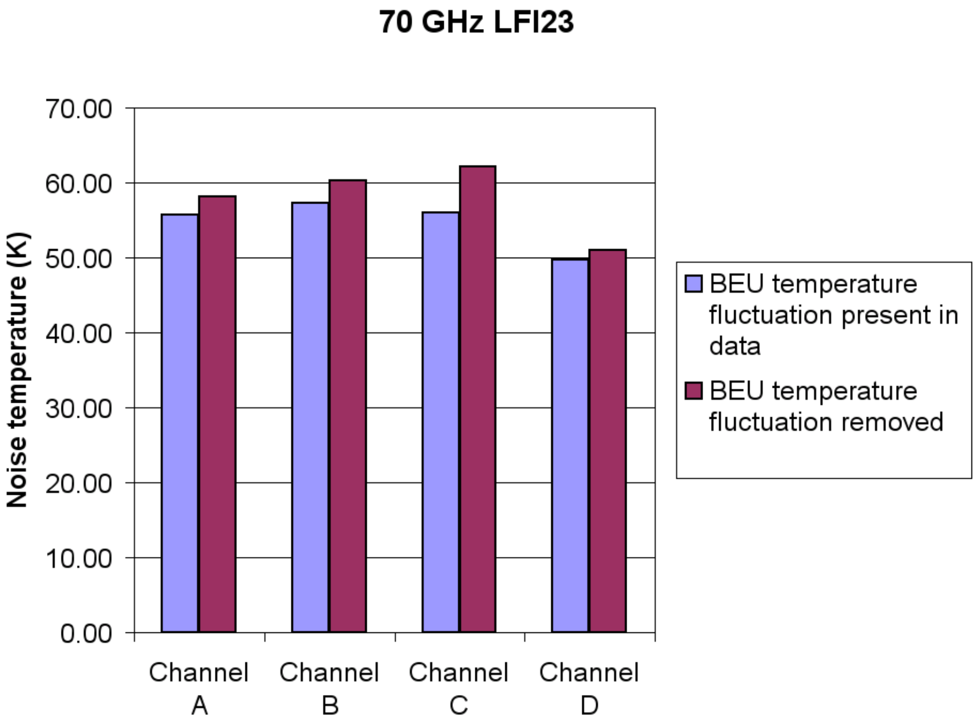
70 GHz LFI23
Noise temperature (K)
70.00
60.00
50.00
40.00
30.00
20.00
10.00
0.00
Channel A
Channel B
Channel C
Channel D
BEU temperature fluctuation present in data
BEU temperature fluctuation removed

Figure 25: Noise temperatures estimated from tests listed in Table 3: (a) LFI28 - 30 GHz, (b) LFI24 - 44 GHz, (c) LFI23 - 70 GHz. Sky load temperature data from ECCOSORB sensor

The results summarised in Figures 25 show the same trend found in Figures 19, although the noise temperature values are ∼5 K lower. In practice this result indicates that the choice of which temperature sensor is representative of the sky load temperature is the main source of uncertainty in the noise temperature estimate.

On the sky load used in the RCA tests results from thermal modelling as well as from measurements indicate that the sensor on the metal plate is the more representative of the sky load temperature at the centre of the bed of pyramids; unfortunately a detailed thermal model of the RAA sky load has not been developed, so that we cannot extrapolate this result to our case.

Therefore in the testing of the LFI flight model we will explore the possibility to place at least one more temperature sensor near the centre of the ECCOSORB layer; this way we will have more sound information of the sky load temperature distribution.

As shown by the results presented in the next paragraphs, the calibration constant and the isolation show respectively less sensitivity to the choice of the sky load temperature sensor, as these quantities are derived from differential values rather than from absolute temperature values.

Photometric calibration. In Figure 26 we show the $\Delta V - \Delta T$ diagram relative for the 30 GHz LFI28 receiver (channel A) for all the datasets considering the BEU temperature instability effect present (left) and removed from data (right). The slope of this line provides the photometric calibration.

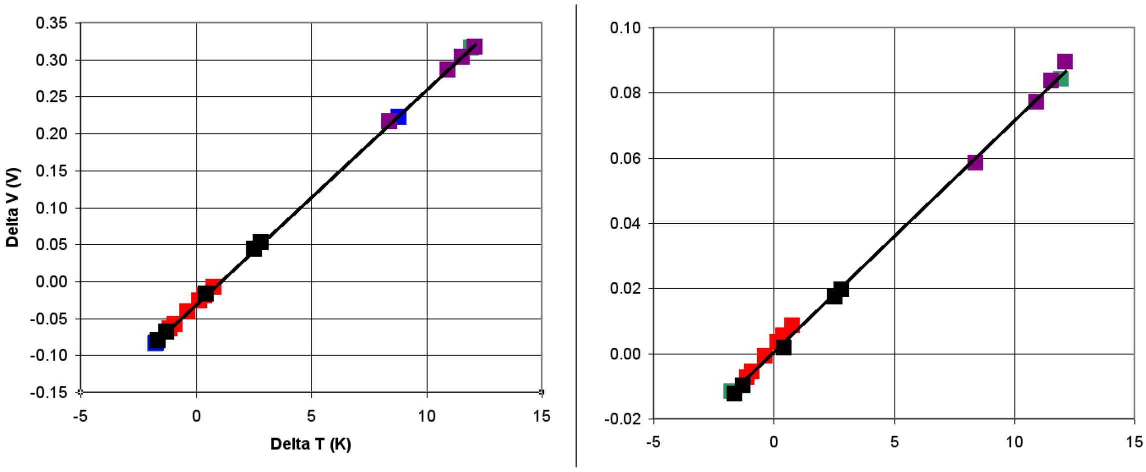

Figure 26: ΔV-ΔT diagram for the 30 GHz LFI28 channel A: (left) with the BEU temperature instability present in data, (right) with the BEU temperature instability removed from the data. Different colors indicate different datasets: Green – ELE_0001, Red – LIS_0002, Blue – ST1_0002, Magenta – ST1_0006, Black – LIS_0001. Sky load temperature data from ECCOSORB sensor.

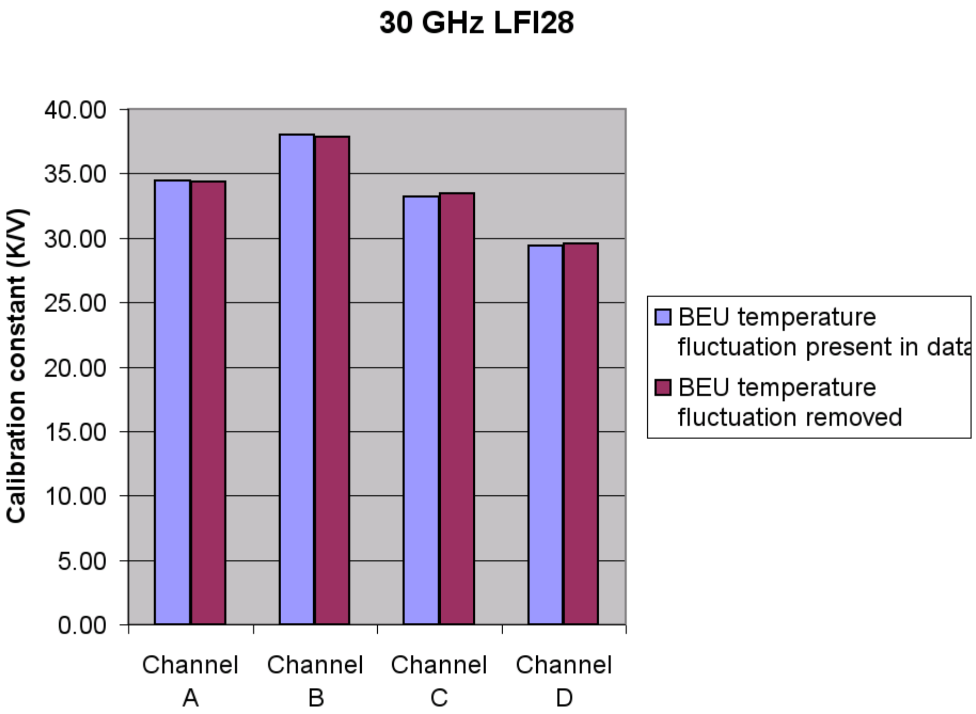
30 GHz LFI28
Calibration constant (K/V)
40.00
35.00
30.00
25.00
20.00
15.00
10.00
5.00
0.00
Channel A
Channel B
Channel C
Channel D
BEU temperature fluctuation present in dat
BEU temperature fluctuation removed

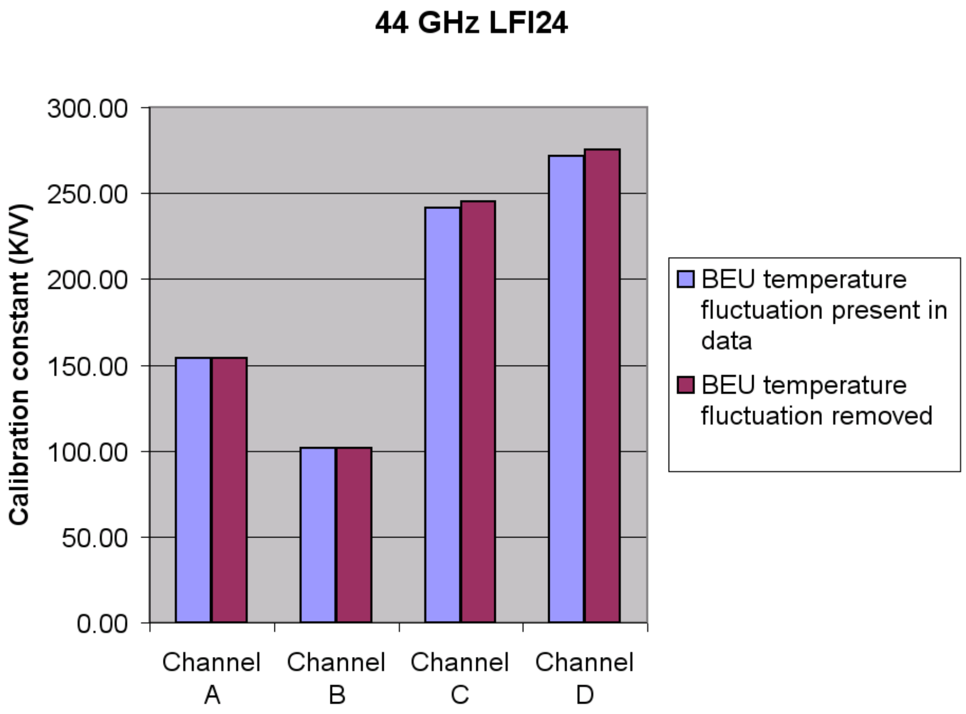
44 GHz LFI24
Calibration constant (K/V)
300.00
250.00
200.00
150.00
100.00
50.00
0.00
Channel A
Channel B
Channel C
Channel D
BEU temperature fluctuation present in data
BEU temperature fluctuation removed

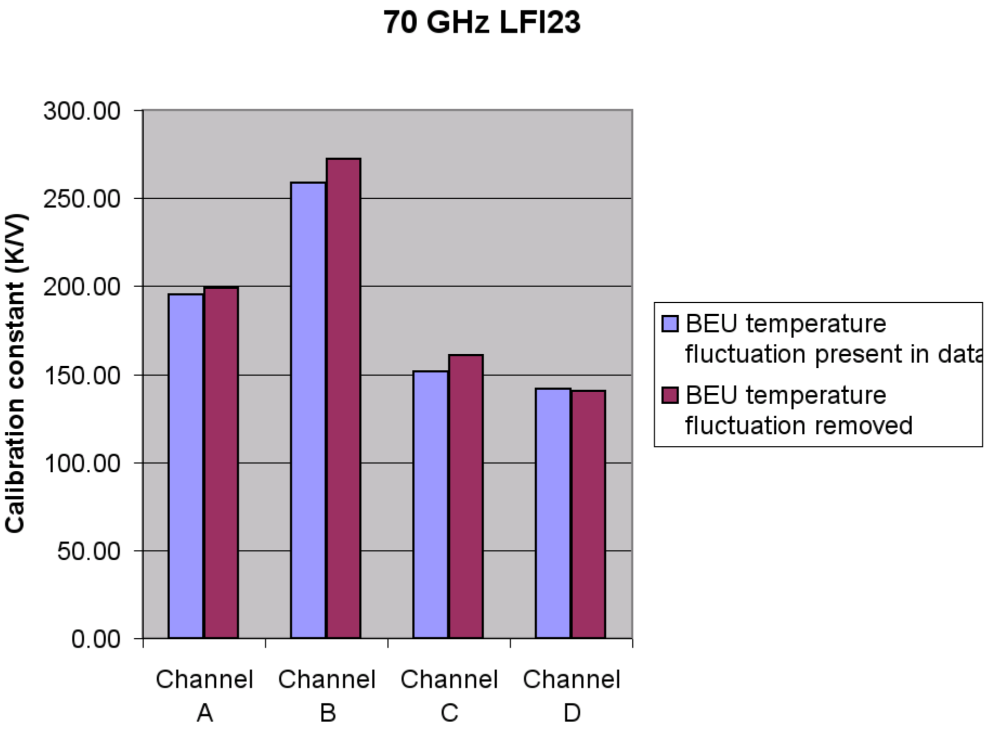

Figure 27: Photometric calibration estimated from tests listed in Table 3: (a) LFI28 - 30 GHz, (b) LFI24 - 44 GHz, (c) LFI23 - 70 GHz. Sky load temperature data from ECCOSORB sensor

Similarly to the previous case, also for the computation of photometric calibration we see that the impact of the temperature fluctuations at the back-end unit level can be considered small.

Isolation. In Figure 28 we show the plot δ_{fixed} *vs* δ_{tot} diagram relative to the 30 GHz LFI28 receiver (channel A) for all the datasets considering the BEU temperature instability effect present (left) and removed from data (right). The slope of this line provides the isolation.

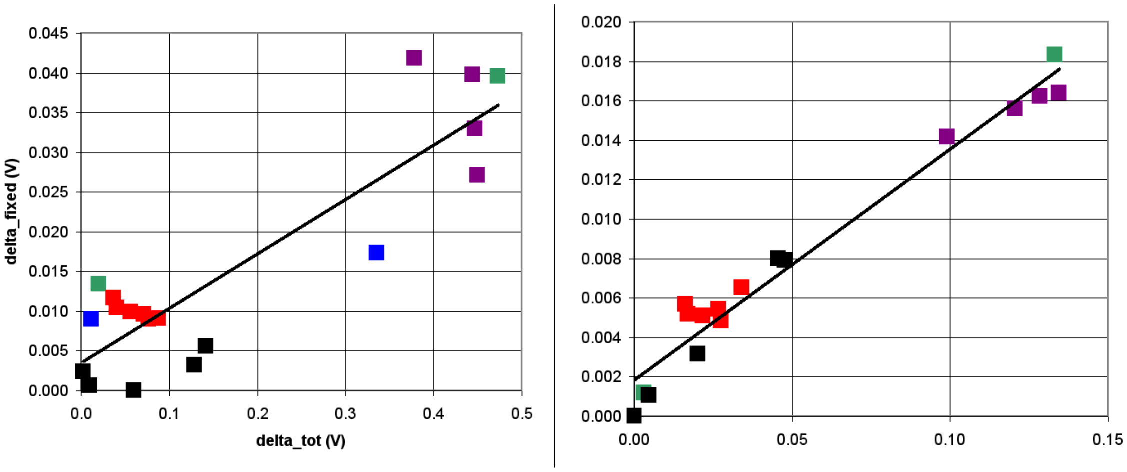

Figure 28: $\delta_{\rm fixed}$ *vs* $\delta_{\rm tot}$ diagram for the 30 GHz LFI28 channel A: (left) with the BEU temperature instability present in data, (right) with the BEU temperature instability removed from the data. Different colors indicate different datasets: Green – ELE_0001, Red – LIS_0002, Blue – ST1_0002, Magenta – ST1_0006, Black – LIS_0001. Sky load temperature data from ECCOSORB sensor.

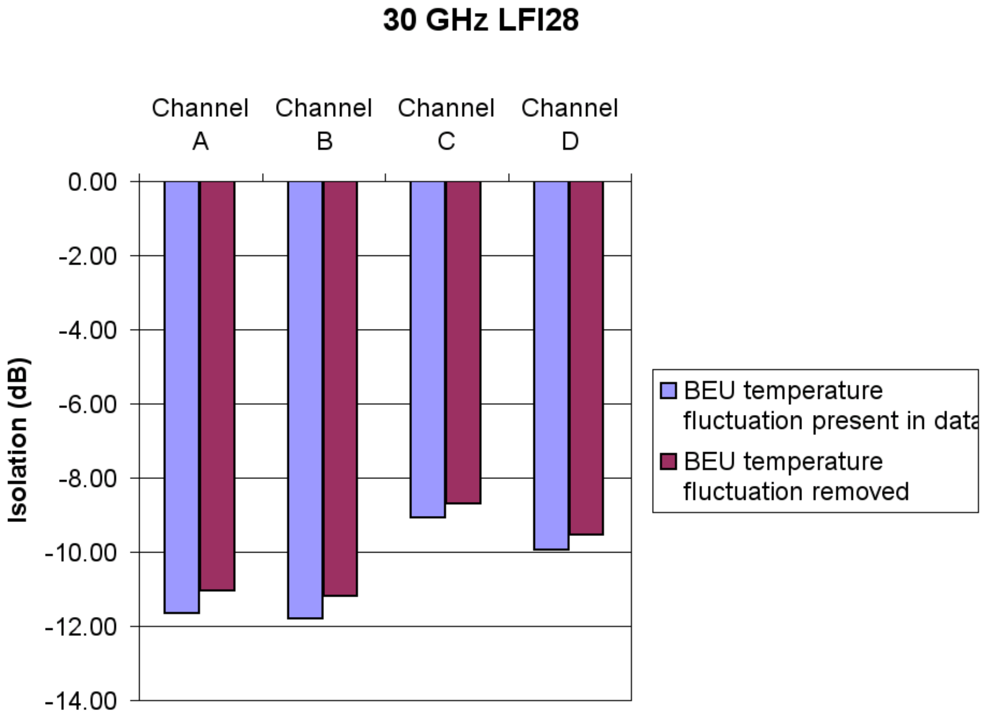

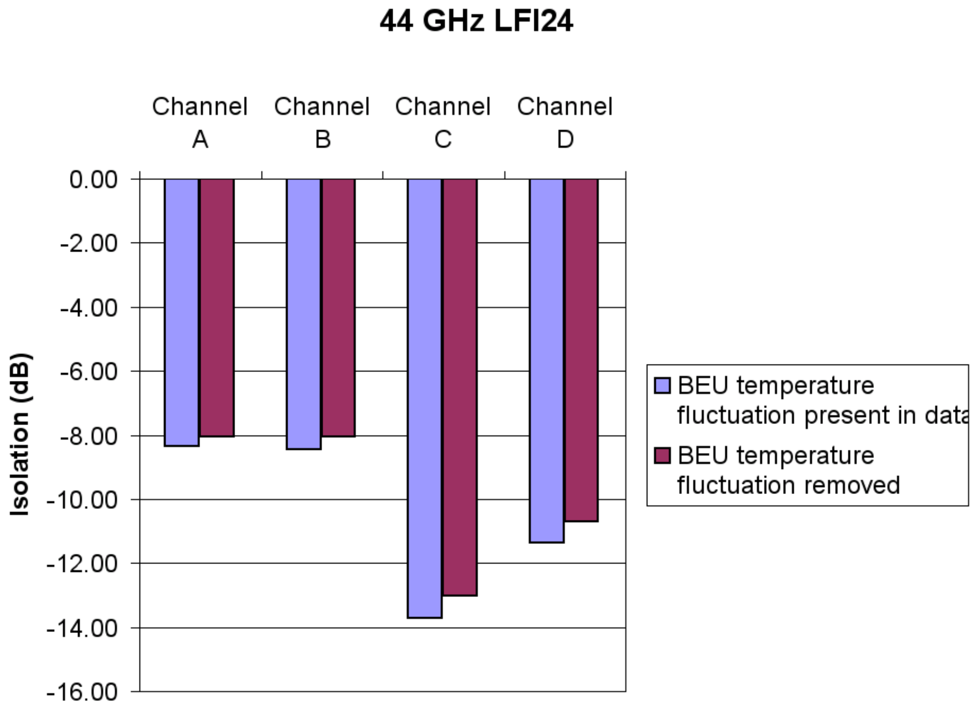
44 GHz LFI24
Channel A
Channel B
Channel C
Channel D
0.00
-2.00
-4.00
-6.00
-8.00
-10.00
-12.00
-14.00
-16.00
Isolation (dB)
BEU temperature fluctuation present in data
BEU temperature fluctuation removed

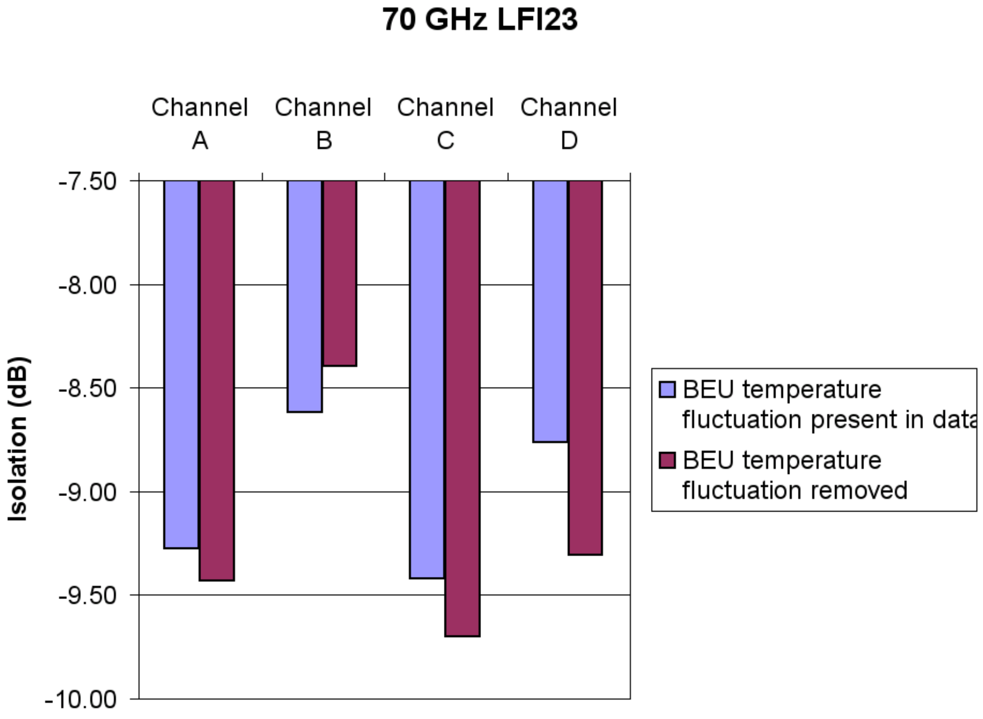
70 GHz LFI23
Channel A
Channel B
Channel C
Channel D
-7.50
-8.00
-8.50
-9.00
-9.50
-10.00
Isolation (dB)
BEU temperature fluctuation present in data
BEU temperature fluctuation removed

Figure 29: Isolation estimated from tests listed in Table 3: (a) LFI28 - 30 GHz, (b) LFI24 - 44 GHz, (c) LFI23 - 70 GHz. Sky load temperature from ECCOSORB sensor.

5.3 Linearity

The linearity factor for all the tests shown here was very small, i.e. in the range 10^{-4} - 10^{-5}; therefore we will not go into the details of the numbers. As an example in Fig. 30 we show three linearity responses (in terms of ΔV vs. ΔT) relative to channels A of the 30 GHz LFI28 and 70 GHz LFI23 and relative to channel C of the 44 GHz LFI24.

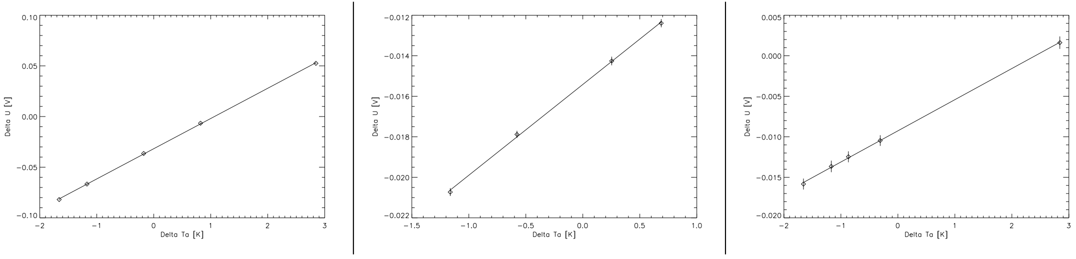

Figure 30: Linearity response of 30 GHz LFI28 (Channel A), 44 GHz LFI24 (Channel C) and 70 GHz LFI23 (Channel A)

5.4 Offset

In the following tables we report the input offset in Kelvin for the three radiometric chains. The values have been derived from the test set LIS_0001. Note that for the 44 GHz LFI24 we report the input offset only for channels A and B because of the anomalous behaviour of C and D during this test. The test LIS_0002 that was used to calculate the basic properties of LFI24 could not be used for the offset calculation as no crossing was present in the data.

Table 6: Input offset in K for the 30 GHz LFI28

OMT Side arm				OMT Main arm			
RAA-A	RCA-D	RAA-B	RCA-C	RAA-C	RCA-A	RAA-D	RCA-B
1.08	TBD[1]	1.06	TBD	-0.48	TBD	0.12	TBD

Table 8: Input offset in K for the 44 GHz LFI24 (only channels A and B)

OMT Side arm			
RAA-A	RCA-B	RAA-B	RCA-A
2.26	0.651	1.34	0.552

---

[1] Not measured yet on 30 GHz QM RCA

Table 10: Input offset in K for the 70 GHz LFI23

OMT Side arm				OMT Main arm			
RAA-A	RCA-A	RAA-B	RCA-B	RAA-C	RCA-C	RAA-D	RCA-D
-0.37	TBD[2]	2.6	TBD	0.13	TBD	0.24	TBD

6 Noise properties

In this section we discuss the main noise properties measured on the LFI QM instrument during August 2005. In the following we will use the symbols: $\Delta\nu$ = effective bandwidth; w_{noise} = white noise level; r = gain modulation factor; T_{sys} = system temperature; T_{sky} = sky temperature; T_{ref} = reference temperature; V_{sky} = sky voltage; V_{ref} = reference voltage; V_{diff} = difference voltage. The differenced radiometric data is defined by the following relation

$$V_{\text{diff}} = V_{\text{sky}} - rV_{\text{ref}}, \tag{2}$$

where r is the gain modulation factor given by $< V_{\text{sky}} > / < V_{\text{ref}} >$.

6.1 Experimental conditions

The data we have used in this analysis are from two consecutive tests named ST1_0005 and ST1_0006. Both tests provided scientific and housekeeping data for the 30 GHz #28, 44 GHz #24, and 70 GHz #23 LFI radiometers. The 70 GHz #18 was not working during these tests and it is not being considered in this report.

The ST1_0005 test consists of 15.3 hours of data acquired in quasi-stable conditions. In Figure 31 we show the behaviour of the sky and reference loads temperature during the test. The figure shows that the reference load was stable at the level of 10 mK peak-to-peak, while the sky load increased its temperature by about 250 mK during the test. The ST1_0006 test consists of 22.9 hours of data and includes a sky load temperature step from 32.9 K to 36.5 K with the reference load fixed at 24.5 K. In Figure 32 we show the behaviour of the sky and references loads temperature during the test. The ST1_0005 test contains useful data for white noise and $1/f$ estimation, the ST1_0006 test contains useful data for T_{sys}, G, and sensitivity estimation.

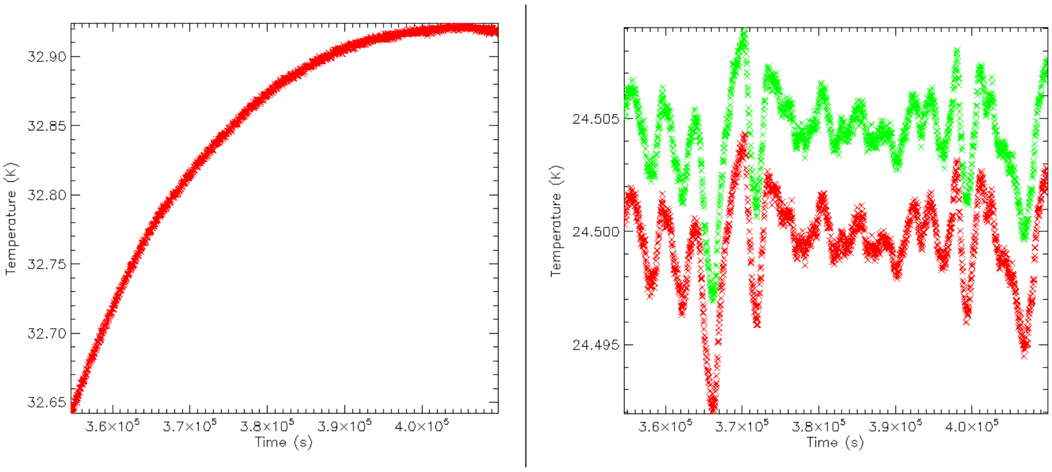

Figure 31: Behaviour of the temperature of the sky load (left) and of the reference loads (right) during the ST1_0005 test.

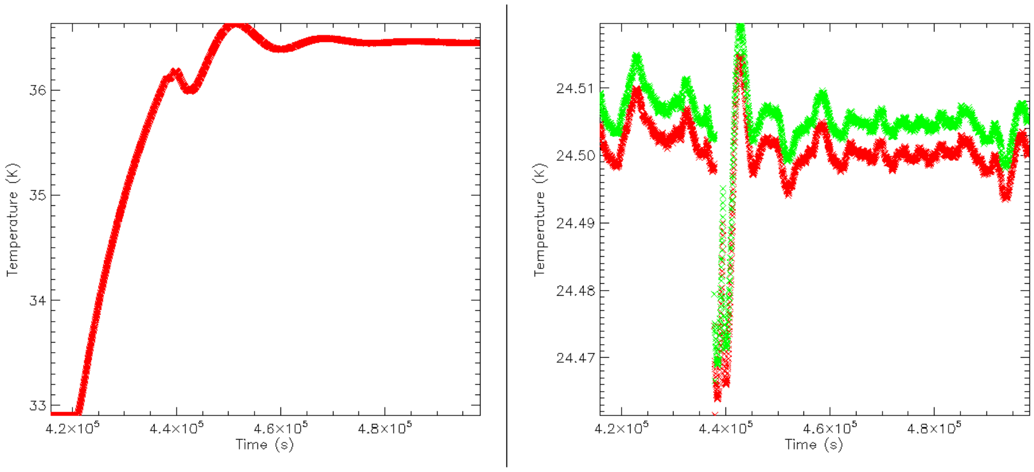

Figure 32: Behaviour of the temperature of the sky load (left) and of the references loads (right) during the ST1_0006 test.

The FPU temperature was relatively stable, with only a small decrease of the order of 10 mK, while the BEU temperature fluctuated in a periodic pattern as in all the tests reported in this document. In Figures 33 and 34 we show, respectively, the temperature behaviour of the FPU and BEU during the tests.

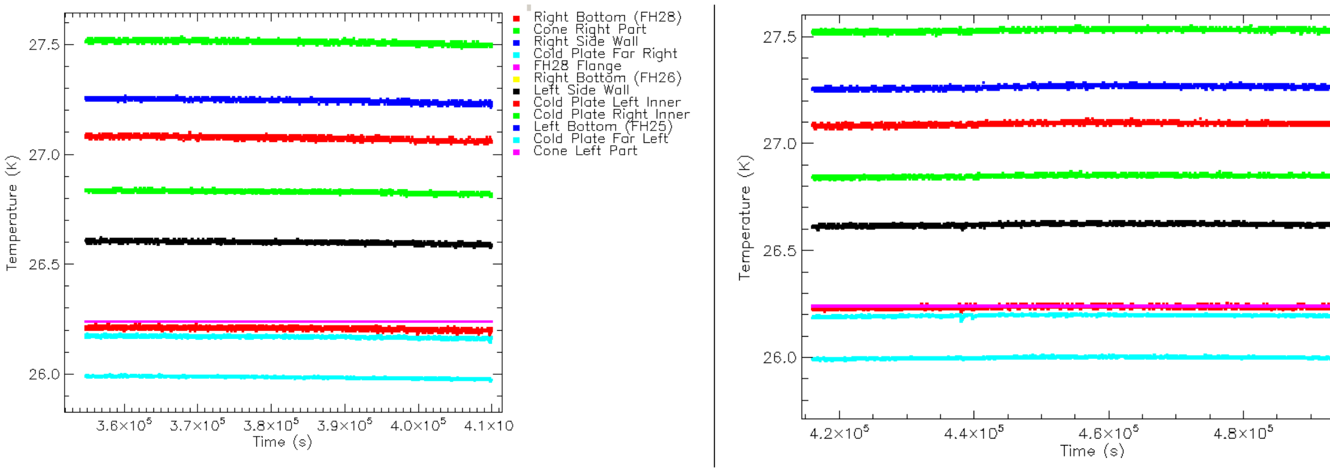

---

[2] Not measured yet on 70 GHz EM RCA

Figure 33: Behaviour of the temperatures of the FPU during the ST1_0005 (left) and ST1_0006 (right) tests.

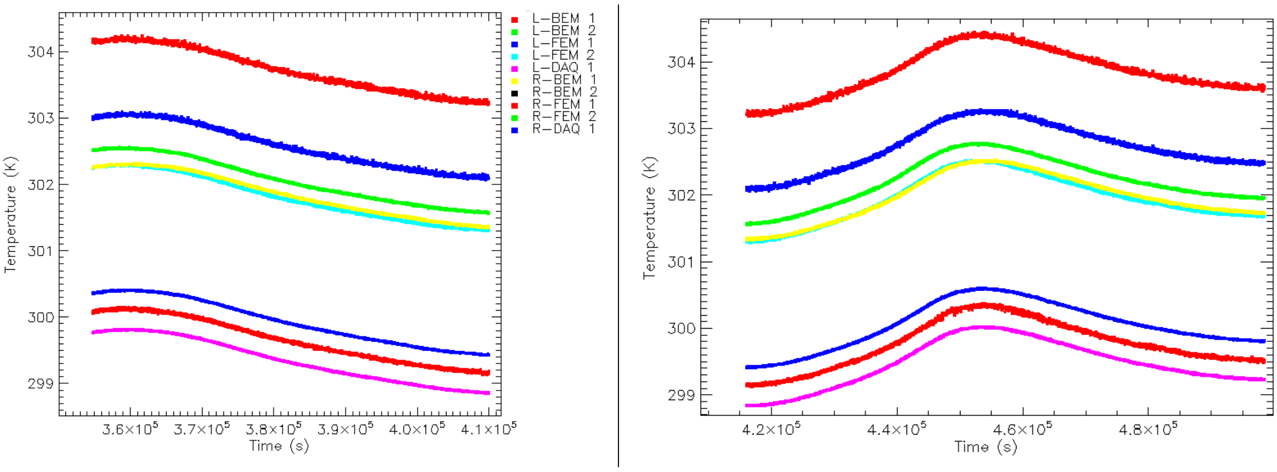

Figure 34: Behaviour of the temperatures of the BEU during the ST1_0005 (left) and ST1_0006 (right) tests.

The data were acquired in REBA mode 1, i.e. with only the data binning; in Table 12 we show the sampling rate for each horn in those tests that is consequence of the REBA data binning.

Table 12: Sample rate of the RAA QM data.

Radiometer	Sample rate (Hz)
30 GHz #28	32.507937
44 GHz #24	46.545455
70 GHz #18	not working
70 GHz #23	78.769231

The LIFE package (Lfi Integrated perFormance Evaluator) was the main tool used for the data analysis reported in here. For analysis purpose, the $T_{\rm sky}$ and $T_{\rm ref}$ were obtained, respectively, from the environmental data labeled SKY E.sorb (in Extra temperatures) and Reference_Load_1 (in CSL temperatures). To perform the analysis, we selected for each horn and channel, data sections where the signal and all the temperature sensors registered an approximately constant value during a time interval much greater then the time length of a given section, and the log messages do not report any event occurring during the section. All the errors reported are the statistical uncertainty. Systematic error were not included in the analysis.

6.2 RAA 30 GHz #28 QM noise parameters

After a visual inspection of the ST1_0005 data plots, we selected an uncalibrated data section containing 3 hours of RAA QM data with bin chosen as 1, starting at 355000 sec. For channels A and C we selected the option swap sky-ref as they were had a wrong identification in the telemetry packets.

In Figures 35, and 36 we show an example of the differenced data on detector C in time and frequency domain. Note that the sky-load difference shows a linear trend that is correlated with a change in the sky-load temperature during the test (see Figure 31). In the computation of the power spectrum this linear trend was removed.

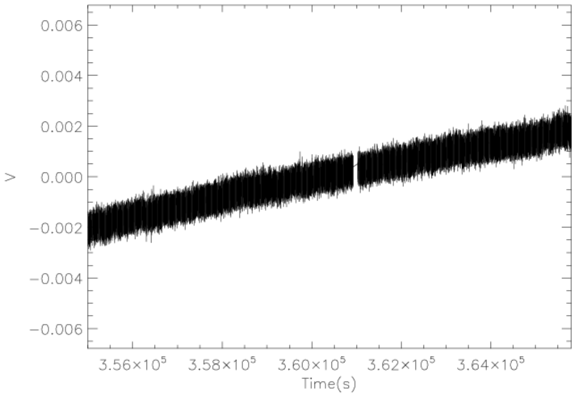

Figure 35: Differenced data for LFI28 channel C (left) showing a linear trend. This trend is correlated with a change in sky load temperature.

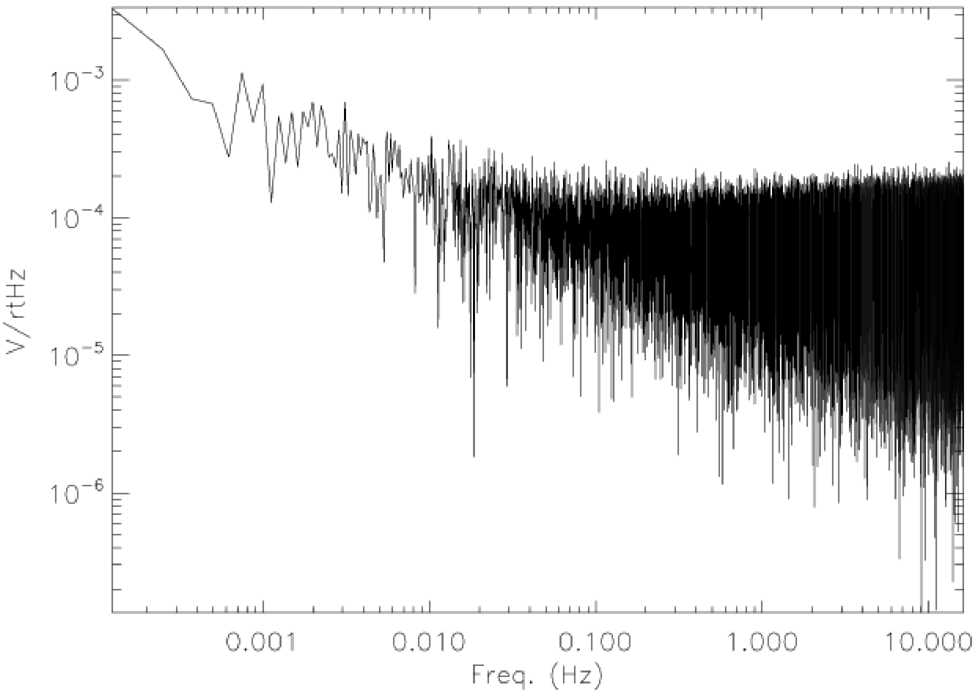

Figure 36: Power spectrum of differenced data shown in Figure 35. The linear trend due to the sky load variation was removed before Fourier transforming the data. The $1/f$ knee is $\sim$ 50 mHz and the $1/f$ slope is ~ -1.0.

Using the selected subset of data, we computed the gain modulation factor r from the ratio of the signal DC levels, the white noise level of the differenced data ($V_{\rm diff}$), the noise effective bandwidth ($\Delta\nu$), and the $1/f$ parameters. Note that with the RAA data it is not possible to resolve the white noise from the total power data streams, because because in this case the $1/f$ noise dominates up to the REBA sampling frequency. The results are listed in Tables 13 and 14.

Table 13: Noise parameters for 30 GHz $V_{\rm diff}$ data – section in ST1_0005 with 3 hours starting at 355000 s.

Detector	$\Delta\nu$ (GHz)	$w_{\rm noise}$ (μV/$\sqrt{\rm Hz}$)	r
A	5.7	65.5	1.1351
B	5.9	57.8	1.1345
C	7.1	62.1	1.1657
D	6.7	66.6	1.1664

The effective bandwidths and knee frequencies obtained from differenced data are whithin requirements and consistent with measurements obtained at RCA level (cfr with section 2).

Table 14: $1/f$ parameters for 30 GHz V_{diff} data – section in ST1_0005 with 3 hours minutes starting at 355000 s.

Channel label	$1/f$ knee frequency (mHz)	$1/f$ slope
A	26.2	-0.78
B	35.5	-0.98
C	51.1	-1.06
D	24.0	-1.28

To estimate the scattering in the white noise, we computed it for 15 different sections each one containing 12 minutes of 30 GHz RAA data. Figure 37 shows the white noise scattering from ST1_0005 test. Table 15 provides the white noise measured for 30 GHz RAA.

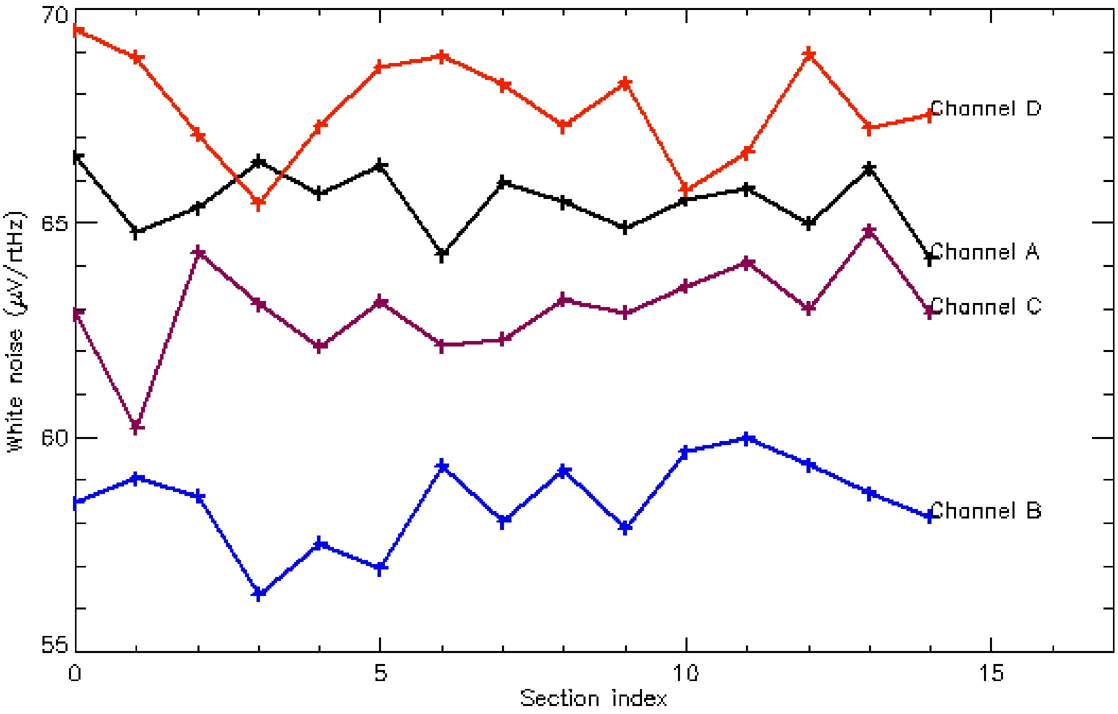

Figure 37: White noise level from 15 different sections of data from ST1_0005 test, each section is 12 minutes in length

The step in T_{sky} in the test ST1_0006 allowed us to obtain calibrations and T_{sys} for each diode using the Y-factor method from DC level and white noise level. The results shown in Table 16 were obtained using two sections with 2400 s in lenght each. The first sections starts at 416210 seconds. The second sections starts at 483420 seconds. To compute the white noise scattering

Table 15: White noise measured for 30 GHz $V_{\rm diff}$ – section in ST1_0005.

Channel label	A	B	C	D
$w_{\rm noise}$ (μV/$\sqrt{\rm Hz}$)	65.5 ± 0.2	58.5 ± 0.3	63.0 ± 0.2	67.7 ± 0.3

we used 8 sections each one containing 5 minutes of 30 GHz data. The white noise and the gain modulation factor reported in Table 16 are from the first section.

Table 16: Noise parameters for 30 GHz $V_{\rm diff}$ data – sections in ST1_0006.

Channel label	A	B	C	D
Y factor from DC	1.0526 ± 0.0008	1.0522 ± 0.0008	1.0543 ± 0.0006	1.0577 ± 0.0005
Y factor from $w_{\rm noise}$	1.06 ± 0.01	1.07 ± 0.02	1.05 ± 0.01	1.05 ± 0.02
r	1.1387 ± 0.0008	1.1382 ± 0.0008	1.1693 ± 0.0006	1.1702 ± 0.0006
$\Delta\nu$ (GHz)	5.9 ± 0.1	5.6 ± 0.2	7.2 ± 0.1	6.6 ± 0.2

Our measurements show that the $T_{\rm sys}$ obtained from DC and white noise level are consistent with each other inside the error bars. This is an indication that the white noise is being resolved. The effective bandwidths obtained are consistent with LFI specifications for this band. The $1/f$ knee is well below 100 mHz as we would desire.

6.3 RAA 44 GHz #24 QM noise parameters

A similar procedure as described in the last section was applied to the 44 GHz data. From ST1_0005 file, we selected an uncalibrated data section containing 3 hours of RAA QM data at the full REBA sampling rate. We swapped the sky and reference channels for channels B and D because of the unconsistency in the data identification. The results we have obtained are listed in Table 17.

Table 17: Noise parameters for 44 GHz $V_{\rm diff}$ data – section in ST1_0005 with 3 hours starting at 355000 s.

Detector	$\Delta\nu$ (GHz)	$w_{\rm noise}$ (μV/$\sqrt{\rm Hz}$)	r
A	6.9	24.4	1.061
B	10.9	24.5	1.000
C	1.8	16.5	1.079
D	3.4	10.2	1.126

We notice, in the data above, that channels C and D are characterised by a very small effective bandwidth, a problem that was already known from the FEM+BEM tests and understood as the result in a non nominal effective bandwidth of the BEM for these channels.

In Table 18 we summarise the $1/f$ characteristics of LFI24. Also in this case we removed the linear drift in the differenced data caused by the sky load temperature change before Fourier transforming the data. In Figure 38 we show, as an example, the power spectrum of the differenced output from channel C of LFI24.

Table 18: $1/f$ parameters for 44 GHz V_{diff} data – section in ST1_0005 with 3 hours starting at 355000 s.

Channel label	$1/f$ knee frequency (Hz)	$1/f$ slope
A difference	0.054	-0.55
B difference	0.041	-0.95
C difference	0.0450	-0.38
D difference	0.0318	-0.91

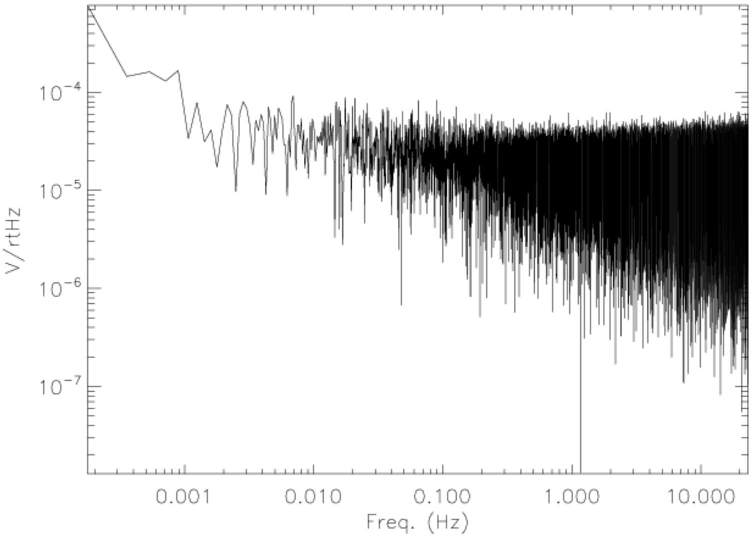

Figure 38: Power spectrum amplitude for 44 GHz difference data in channel C. The white noise level is 16.5 μV/$\sqrt{\text{Hz}}$. The $1/f$ knee frequency is ∼ 45 mHz and the slope is $\alpha \sim -0.38$.

The step in T_{sky} in the test ST1_0006 allowed us to obtain calibrations and T_{sys} for each diode using the Y-factor method. The results are shown in Table 19.

Here we note that each channel has a different noise behaviour. Channels A, C, and D presented an effective bandwidths smaller that the 8.8 GHz required by LFI specification for this band. Channel B shows anomalous high bandwidth. For channels A, C, and D it seems that $\Delta\nu$ correlates with the DC level (mean signal) and we note that the T_{sys} we get from DC level does not match the one we get from white noise level. This behaviour would be consistent with excess of white noise. The small scattering in the white noise we have seen in channel B is also consistent with the hypothesis of quasi-saturation in this channel. The $1/f$ knee are below 100 mHz but this could result from the low bandwidth we have been observing.

Table 19: Noise parameters for 44 GHz V_{diff} data – sections in ST1_0006.

Channel label	A	B	C	D
Y factor from DC	1.027 ± 0.001	1.033 ± 0.002	1.050 ± 0.002	1.057 ± 0.002
Y factor from w_{noise}	1.03 ± 0.02	1.04 ± 0.01	1.05 ± 0.01	1.05 ± 0.01
r	1.0620 ± 0.0009	1.0314 ± 0.0002	1.082 ± 0.002	1.129 ± 0.002
$\Delta\nu$ (GHz)	7.1 ± 0.1	11.0 ± 0.11	2.06 ± 0.03	3.78 ± 0.06

6.4 RAA 70 GHz #23 QM noise parameters

As in the previous cases we selected an uncalibrated data section containing 3 hours of 70 GHz #23 RAA QM data with the full REBA sampling rate. We swapped the sky and reference channels for channels B and D because of the unconsistency in the dat identification. The measured effective bandwiths and white noise levels are summarised in Table 20.

In Figure 39 we show an example of a power spectrum for the channel C of the 70 GHz LFI23 receiver. Note that with these receiver we see some sensitivity to fluctuations offrequency of 1 Hz (which is the main frequency of the cooler compressors) and higher harmonics. This is apparent in the right panel of Figure 39 where the same spectrum is plotted in linear frequency scale and calculated with Welch windowing to reduce the noise level and highlight the peaks.

A peculiar feature of this series of peaks is the absence of a 4 Hz and 8 Hz harmonics. The reason why only the 70 GHz channel appears to be sensitive to such fluctuations is still unclear.

Table 20: Noise parameters for 70 GHz #23 V_{diff} data – section in ST1_0005 with 3 hours starting at 355000 s.

Detector	$\Delta\nu$ (GHz)	w_{noise} measured ($\mu\mathrm{V}/\sqrt{\mathrm{Hz}}$)	r
A	8.0	17.0	1.094
B	4.6	17.8	1.055
C	9.8	19.3	1.074
D	8.4	21.5	1.089

Table 21: $1/f$ parameters for 70 GHz V_{sky} and V_{ref} data – section in ST1_0005 with 3 hours starting at 355000 s.

Channel label	$1/f$ knee frequency (Hz)	$1/f$ slope
A difference	0.164	-1.079
B difference	0.100	-0.911
C difference	0.085	-0.622
D difference	0.077	-0.983

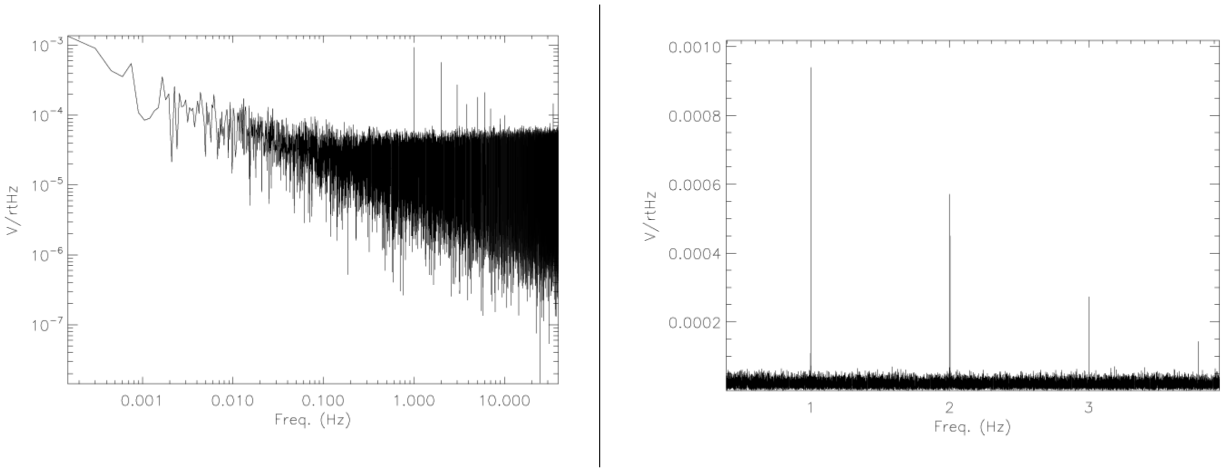

Figure 39: Power spectrum amplitude for 70 GHz LFI23 differenced data in channel C. The left panel shows the full noise spectrum in log-log scale, the right panel shows the noise spectrum in linear scale to highlight the spikes at multiples of 1 Hz. The white noise level is 19.3 $\mu\mathrm{V}/\sqrt{\mathrm{Hz}}$. The $1/f$ knee frequency is $\sim$ 85 mHz and the slope is $\alpha \sim -0.62$.

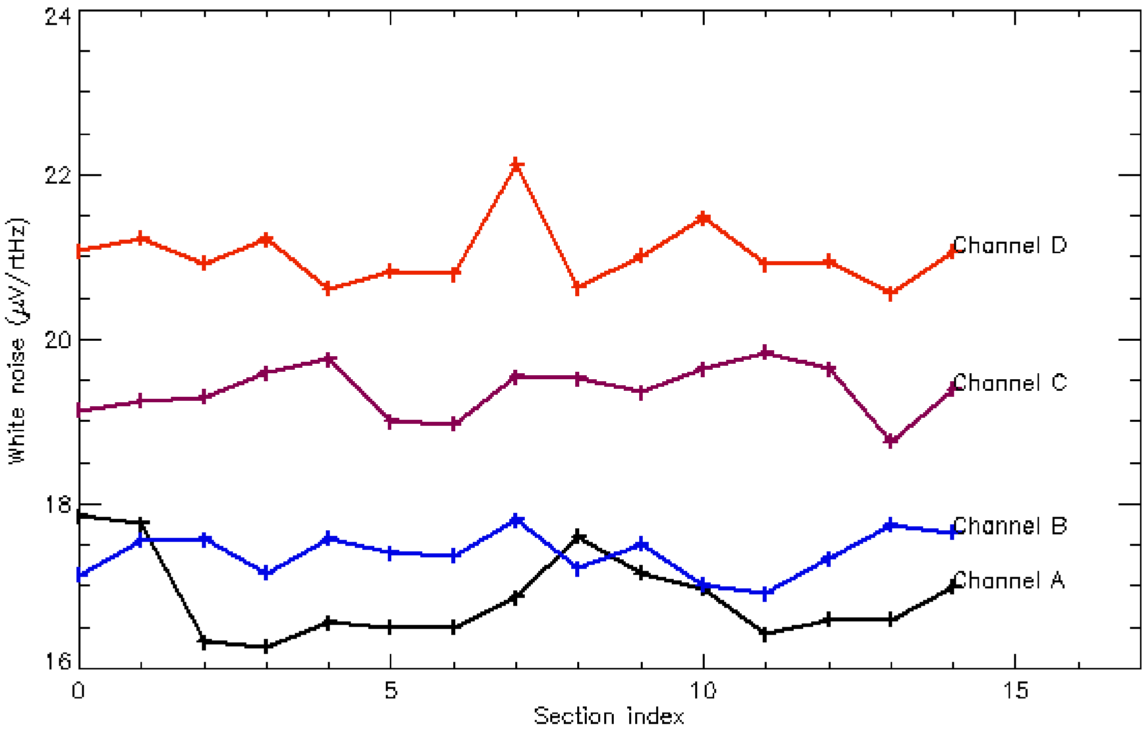

The step in T_{sky} in the test ST1_0006 allowed us to obtain calibrations and T_{sys} for each diode using the Y-factor method. The results are shown in Table 23.

Figure 40: White noise level from 15 different sections of data from ST1_0005 test, each section is 12 minutes in length

Table 22: White noise measured for 70 GHz $V_{\rm diff}$ – section in ST1_0005.

Channel label	A	B	C	D
$w_{\rm noise}$ (μV/$\sqrt{\rm Hz}$)	16.8 ± 0.1	17.4 ± 0.1	19.4 ± 0.1	21.0 ± 0.1

The difference data from all the channels present a smaller bandwidth than the 14 GHz required by LFI specifications for this band. Comparison with the $T_{\rm sys}$ from DC level and white noise reveals that the white noise was probably not well resolved, considering that we did not change the DAE offset and gain. The $1/f$ knee is above 100 mHz for channel A.

6.5 Conclusion

The results obtained at 30 GHz are consistent with the measurements performed at RCA level.

Channel B of the 44 GHz chain shows an unnaturally high effective bandwidth. This is consistent with the strange results obtained for the noise temperature, which indicates a possible problem in the setting and/or in the monitoring of the DAE offset and gain for this channel. The results obtained with the other 44 GHz channels are not consistent with each other. Further investigation would be desired to understand the 44 GHz noise behaviour.

The results obtained at 70 GHz are generally consistent with RCA measurements and indicate that the white noise was probably not very well resolved (and in fact for this channel the DAE gain and offset was left at the default values of 1 and 0 V). Therefore we might expect an underestimation of the effective bandwidth for this receiver.

The 70 GHz #18 was not working and its noise parameters still need to be measured.

7 Susceptibility tests

7.1 Susceptibility to front-end temperature fluctuations

7.1.1 Test theory

The objective of the susceptibility test to variations in the front-end temperature is the measurement of the radiometric response in the differential output to variation of the FPU physical temperature. Details on the test theory can be found, for example, in [AD4, AD3] and [RD4].

Furthermore, previous studies (see, for example, [RD2]) have indicated that this response is expected to be linear, so that we can describe in with a proportionality constant in units of K/K that indicates how many K (in antenna temperature) we expect in the differential radiometric output per Kelvin of variation in the front-end physical temperature.

7.1.2 Test experimental conditions

Ideally the test is conducted inducing a series of steps in the FPU temperature and then recording the radiometric output for each step when the system has reached thermal stability. Furthermore one would like to measure the temperature directly on the front-end modules of each radiometer

Table 23: Noise parameters for 70 GHz V_{diff} data – sections in ST1_0006.

Channel label	A	B	C	D
Y factor from DC	1.041 ± 0.003	1.046 ± 0.004	1.040 ± 0.001	1.043 ± 0.002
Y factor from w_{noise}	1.00 ± 0.01	1.00 ± 0.01	1.00 ± 0.01	1.0 ± 0.01
r	1.096 ± 0.003	1.056 ± 0.004	1.076 ± 0.002	1.091 ± 0.002
$\Delta\nu$ (GHz)	7.8 ± 0.2	4.5 ± 0.1	9.5 ± 0.1	8.1 ± 0.1

as this temperature varies from FEM to FEM. In particular, at RCA level this test is conducted exactly in this way.

On the RAA, however, there have been some limitations that did not allow to conduct the test in the best possible conditions: in particular the main limitaions have been:

- the number of sensors on the focal plane is limited to 12, and there is none directly placed on any of the front-end modules (see Fig. 41);
- the large thermal mass of the FPU implies that the stabilisation after a temperature step induced at some point takes several hours (differently from the RCA, where the FEM temperature stabilisation was very fast). For this reason we performed the test with a single temperature step and used short data sections in the long stabilisation tail, where we can assume quasi stationarity;
- during the test the radiometric data were affected not only by variations in the front end temperature, but also by temperature variations at the level of the BEU, of the V-grooves and of the sky and reference loads. In the data analysis we could easily account for these last two couplings, while we did not try to remove the effects of the BEU and V-grooves temperature variations, although this could be possible, in principle, at first order. In the next issue of this document we will report also on the attempts to remove from the data these spurious effects.

These limitations caused an uncertainty in the computed transfer function that manifested as a discrepancy between the measured and theoretically computed values, differently from the RCA tests, where the match betweem measurements and theory has been very good.

Further limitations caused by contingencies during the testing campaign have been:

- we could not determine the transfer function for the 70 GHz LFI28 RCA as after this test this chain was re-bised with a different set of bias values. The photometric calibration (which is necessary in the computation of the transfer function) was then calculated for the new set of biases while we do not have available photometric calibration factors for the bias values at which this test was conducted;
- some of the sensors in the focal plane were not working properly. This limited the choice of temperature sensors to be chosen in the data analysis, thus increasing the uncertainty on the final measured value. A possibility to overcome this limitation and improve the estimate of the transfer function is to use thermal model predictions of the temperature behaviour in close proximity of the radiometer front-end modules. Results of this kind of analysis will be reported in a future issue of this document.

In Figure 41 we show the location of the 12 sensors in the LFI focal plane. The five circled points indicate the high resolution sensors that will be used to monitor temperature stability.

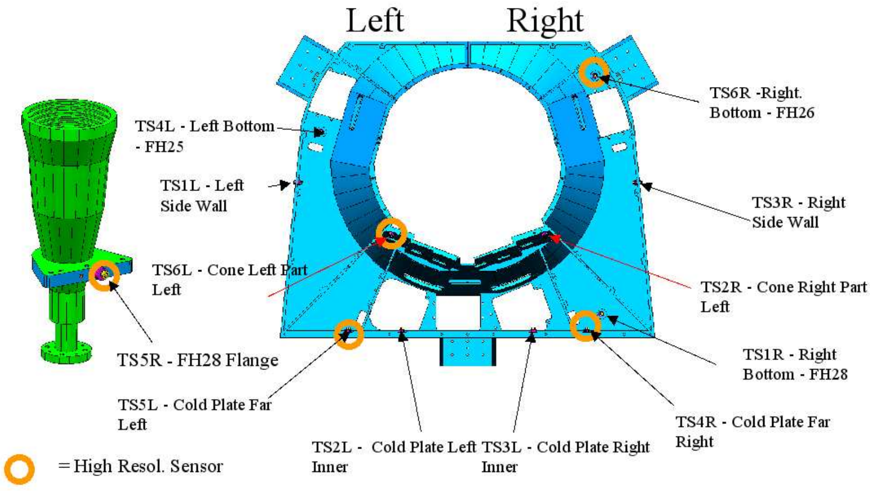

Figure 41: Location of the 12 temperature sensors in the focal plane

In Table 24 we list the FPU temperature sensors with their name, location on the focal plane unit and a comment on their functionality during the LFI QM tests. In particular two of these sensors were not working and other two saturated at the temperature of 23.6 K. The cause of this failure is still TBD and the problem is currently under investigation.

Table 24: List of the 12 temperature sensors in the focal plane with indication of their functionality during the LFI QM tests

Sensor name	Sensor position	Functional ?
TS1L	Left side wall	Yes
TS2L	Cold plate left inner	Yes
TS3L	Cold plate right inner	Yes
TS4L	Left bottom (FH25)	Yes
TS5L	(High Resol.) Cold plate far left	Saturates at 26.3 K
TS6L	(High Resol.) Cone left part (on QM: FH27 flange)	Saturates at 26.3 K
TS1R	Right bottom (FH28)	Yes
TS2R	Cone right part	Yes
TS3R	Right side wall	Yes
TS4R	(High Resol.) Cold plate far right	Saturates at 26.3 K
TS5R	(High Resol.) FH28 flange	No
TS6R	(High Resol.) Right bottom (FH26) (on QM: OMT RCA 26)	No

The sensor that we have considered as the most representative of the temperature of the front end modules has been the TS2R, which was close to all the RCAs LFI24 and LFI28. We remind here that the two 70 GHz receivers were not considered in this test because:

- the LFI18 was not working properly, as discussed in Section 1.3.2, and
- the LFI23 was rebiased after this test, so that the photometric calibration constant (that was determined after the rebiasing) could not be used in the analysis of the temperature susceptibility data.

7.1.3 Temperature behaviour during the test

This test lasted about 20 hours, during which a temperature rise of about 2 K was induced on a resistor close to the temperature sensor TS2L. In Figure 42 we show the position of the heater on the focal plane, while in Figure 43 we show a plot of the temperatures recorded by the working sensors on the focal plane.

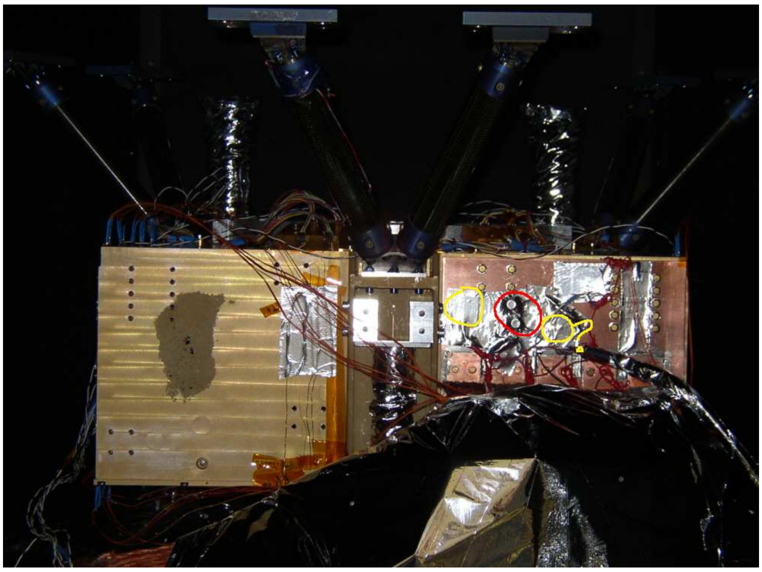

Figure 42: Position of the heater on the focal plane used to increase the focal plane temperature. The heater is enclosed in the red circle, while the two sensors TS3L and TS4R.

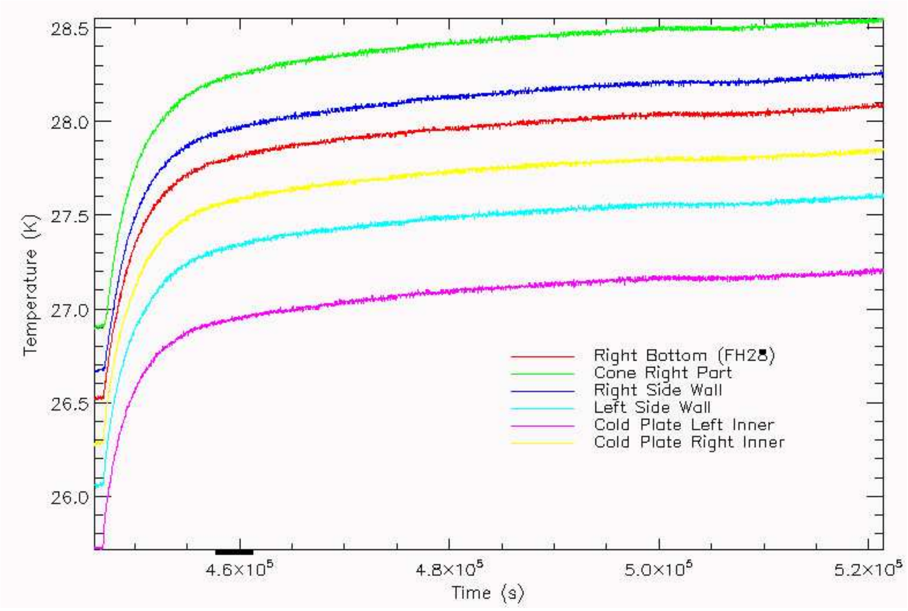

Figure 43: Focal plane temperatures during the temperature susceptibility test

In the next figure we show the behaviour of the sky and reference load temperatures, indicating a clear correaltion with the focal plane temperatures. By knowing the photometric calibration constant it was possible to remove the effect of this variation from the data.

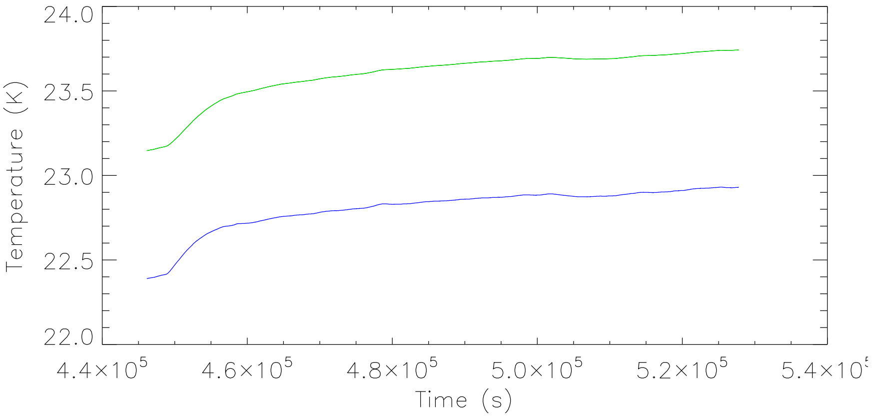

Figure 44: Sky (blue line) and reference load (green line) temperature behaviour during the temperature susceptibility test

Finally, in Figure 45 we show the variation of the back-end unit temperature, which shows a ∼ 1K variation with a main period of ∼ 24 hours. The effect of this variation was not removed from the data. In principle, however, it is possible to remove this effect by knowing the radiometric transfer function linking the back-end physical temperature to the differential radiometric output. The results from this more detailed analysis will be included in future releases of this report, but the correction is expected to be of second order importance.

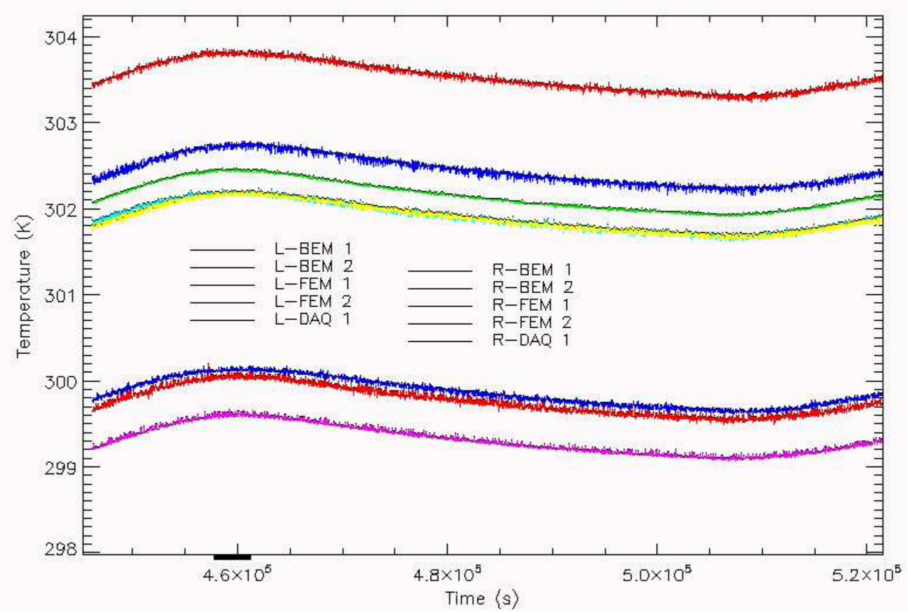

Figure 45: BEU temperatures during the temperature susceptibility test

7.1.4 Results

30 GHz - LFI28 In Table 26 we summarise the measured transfer functions for the 30 GHz RCA compared with those calculated from the theorerical model. The parameters used in the theoretical calculation are summarised in table 25 (cfr with Table 43 of [AD4]).

Table 25: Receiver parameters used in the computation of the theoretical transfer functions

	Ch. A	Ch. B	Ch. C	Ch. D
$\mathrm{L_{feed-OMT}}$ (dB)	0.25			
$\mathrm{L_{4K}}$ (dB)	0.2			
$\mathrm{G_{F1}^{dB}}$ (dB)	35			
$\mathrm{G_{F2}^{dB}}$ (dB)	35			
$\mathrm{T_{nF1}}$ (K)	20		20	
$\mathrm{T_{nF2}}$ (K)	20		20	
$\frac{\partial(\mathrm{G_{F1}^{dB}})}{\partial(\mathrm{T_{phys}^{FE}})}$ (dB/K)	-0.05	-0.03	-0.03	-0.03
$\frac{\partial(\mathrm{G_{F2}^{dB}})}{\partial(\mathrm{T_{phys}^{FE}})}$ (dB/K)	-0.05	-0.03	-0.03	-0.03
$\frac{\partial(\mathrm{T_n})}{\partial(\mathrm{T_{phys}^{FE}})}$ (K/K)	0.12	0.06	0.04	0.051

Table 26: Measured and calculated susceptibility to front end temperature variations

$f_{\rm therm}^{\rm front-end}$ (K/K)	Channel A		Channel B		Channel C		Channel D	
[meas | theo]	0.023	0.006	0.020	0.005	0.002	0.014	0.010	0.010

44 GHz - LFI24 In Table 28 we summarise the measured transfer functions for the 44 GHz RCA compared with those calculated from the theorerical model. The parameters used in the theoretical calculation are summarised in table 27 (cfr with Table 43 of [AD3]).

Table 27: Receiver parameters used in the computation of the theoretical transfer functions

	Ch. A	**Ch. B**	**Ch. C**	**Ch. D**
$L_{\rm feed-OMT}$ (dB)	0.1			
$L_{\rm 4K}$ (dB)	0.2			
$G_{\rm F1}^{\rm dB}$ (dB)	35			
$G_{\rm F2}^{\rm dB}$ (dB)	35			
$T_{\rm nF1}$ (K)	20		20	
$T_{\rm nF2}$ (K)	20		20	
$\frac{\partial(G_{\rm F1}^{\rm dB})}{\partial(T_{\rm phys}^{\rm FE})}$ (dB/K)	-0.05	-0.05	-0.05	-0.05
$\frac{\partial(G_{\rm F2}^{\rm dB})}{\partial(T_{\rm phys}^{\rm FE})}$ (dB/K)	-0.05	-0.05	-0.05	-0.05
$\frac{\partial(T_{\rm n})}{\partial(T_{\rm phys}^{\rm FE})}$ (K/K)	0.8	0.8	0.8	0.8

RESULTS

Table with the measured experimental data and the theoretical simulations:

Index	$(T_{\rm phys}^{\rm FE})_0$ (K)	$(T_{\rm phys}^{\rm FE})_1$ (K)	$\Delta T_{\rm phys}^{\rm FE}$ (K)	$(\delta T_{\rm Sky})_{\rm meas}$ (K)	$(\delta T_{\rm Sky})_{\rm theo}$ (K)
1	26.524288	27.975290	1.4510019	0.056087494	-0.0043985569
2	26.524288	28.031240	1.5069518	0.074771881	-0.0045681631
3	26.524288	28.061519	1.5372305	0.076988220	-0.0046599498

Table 28: Measured and calculated susceptibility to front end temperature variations (LFI24)

$f_{\rm therm}^{\rm front-end}$ (K/K)	Channel A		Channel B		Channel C		Channel D	
[meas | theo]	0.066	0.001	0.18	0.002	-0.199	-0.0125	-0.183	-0.0015

7.1.5 Conclusions

The measured trasfer functions from this test do not match with theoretical calculations, apart from channel D of receiver LFI28. The reasons of this mismatch are presumably the following:

- the test was run with a very small offset between sky and reference load, which results in a very little sensitivity to physical temperature fluctuations (the calculated susceptibility is of the order of $10^{-2} - 10^{-3}$ K/K), which is difficult to measure if the surrouding environment is hot highly stable;
- the analysis was run using the data from the stabilization tail of the temperature ramp, thus exploiting temperature differences of less than a K, which increases the uncertainty in the transfer function estimation;
- the radiometric signal was affected by other sources of instability other than the variation in the focal plane temperature, i.e. in the sky and reference load temperature (corrected at first order in the analysis), in the BEU temperature, in the V-Groove temperature and in the temperature of the thermal tent;
- we considered data from a single sensor as representative of the temperature of all the front-end modules, which again introduces an uncertainty.

Although some of these effects could be accounted for in the data analysis, a sound measurement of such a small quantity requires better temperature stability conditions and a test procedure in which the temperature is varied in steps of few K each and then the system is let to stabilise.

An improvement could also come from running the test with a higher input offset (i.e. a larger difference between sky and reference load temperatures), which would increase the susceptibility to front-end temperature fluctuations. This solution, however, has the drawback that a larger offset causes also a larger susceptibility to other kinds of instabilities.

7.2 Susceptibility to back-end temperature fluctuations

7.2.1 Test theory

The objective of this test is the measurement of the radiometric response in the differencial output to variation of the back-end physical temperature. The test conduction and data analysis is completely similar to the test aiming at characterising the suscetpibility to front-end temperature variations (see Sect. 7.1.1 and references therein).

7.2.2 Test experimental conditions

The susceptibility to back-end temperature variations has been analysed using two different datasets, i.e. LIS_0001 and ST1_0002. Both tests were characterised by long acquisition at stable conditions in which the only instability was caused by the temperature variation of the back-end unit. In the following plots we show the temperature data in the time-windows that have been used in the data analysis.

ST1_0002 dataset. In the following figures we show the behaviour of the relevant temperatures in the dataset ST1_0002 with the system in stable conditions; in particular:

- Fig. 46 shows the BEU and reference load temperature;
- Fig. 47 shows the temperature of the sky load (eccosorb - left - and base plate - right -).
- Fig 48 shows the temperature of the FPU (all the sensors - left - and the detail of sensor TS2R (see Sect. 7.1.2).

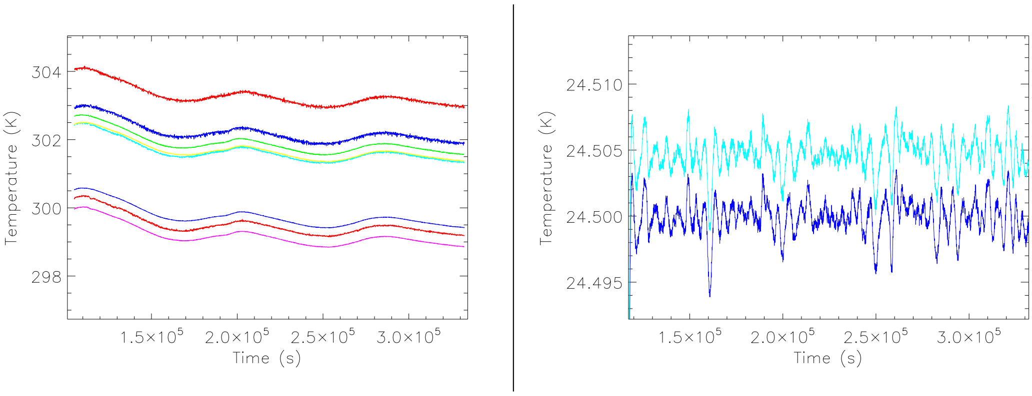

Figure 46: Behaviour of BEU (left) and reference load (right) temperatures during the ST1_0002 test

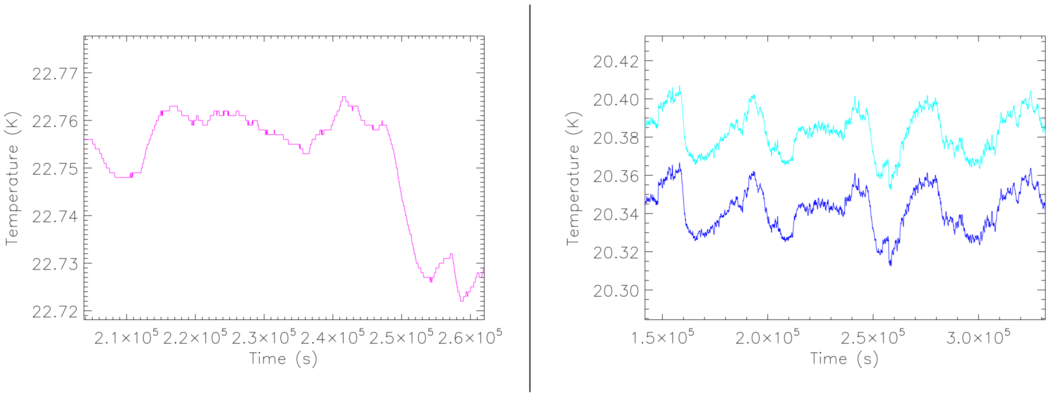

Figure 47: Behaviour of the sky load temperature during the ST1_0002 test. Left: temperature of the ECCSORB bed, right: temperature of the sky load base plate

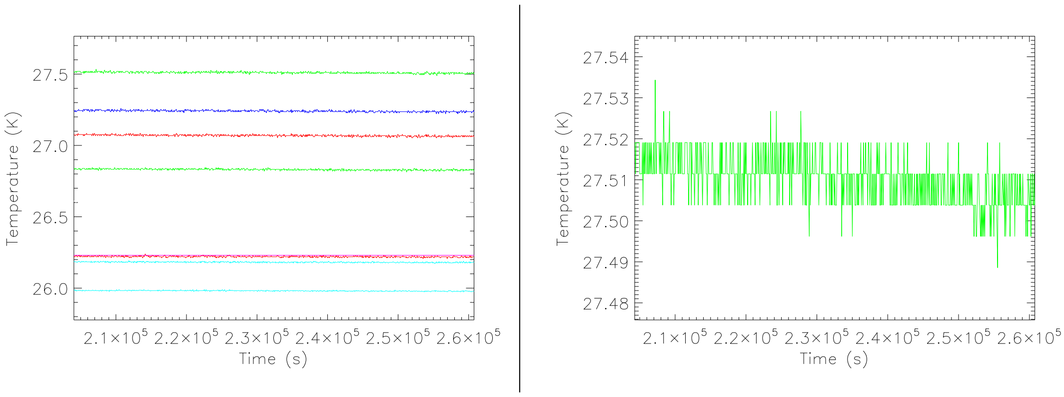

Figure 48: Behaviour of FEU temperatures during the ST1_0002 test. Left: view of all the working FPU sensors, right: detail of sensor TS2R

LIS_0001 dataset. Similarly as above in the following plots we show the behaviour of the temperature at during the last part of the LIS_0001 test, in which the major temperature variation in the system was the periodic fluctuation of the BEU.

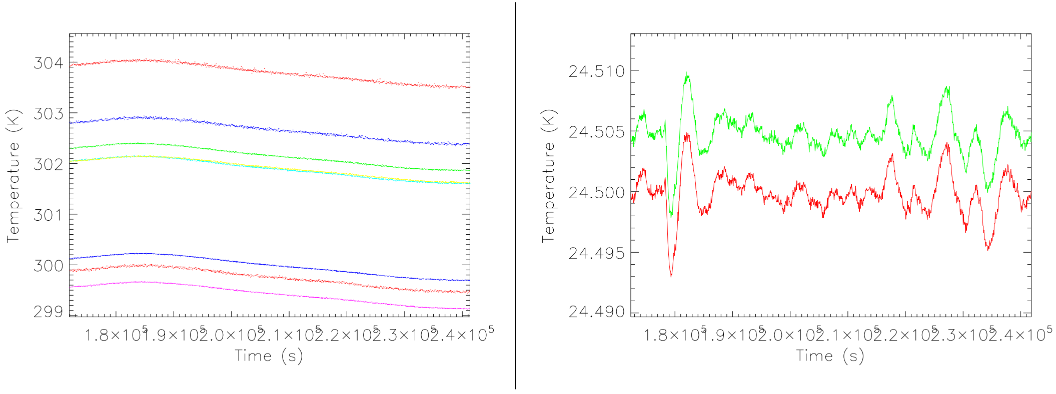

Figure 49: Behaviour of BEU (left) and reference load (right) temperatures during the LIS_0001 test

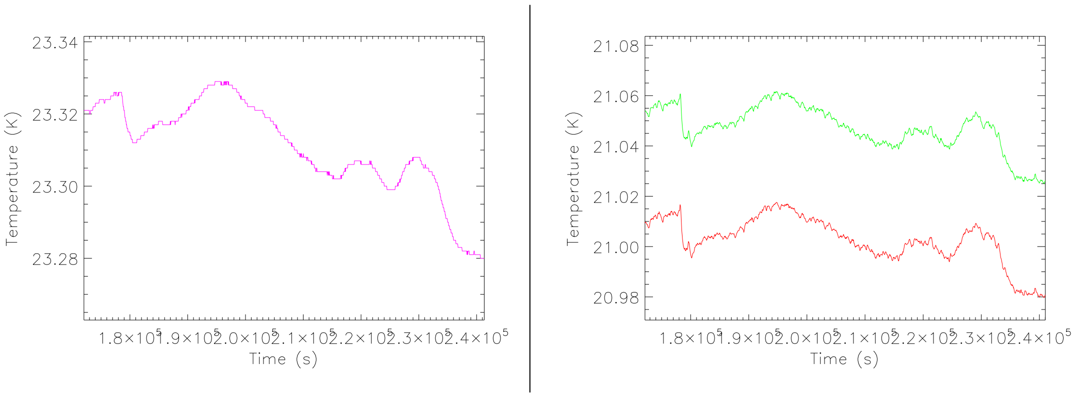

Figure 50: Behaviour of the sky load temperature during the LIS_0001 test. Left: temperature of the ECCSORB bed, right: temperature of the sky load base plate

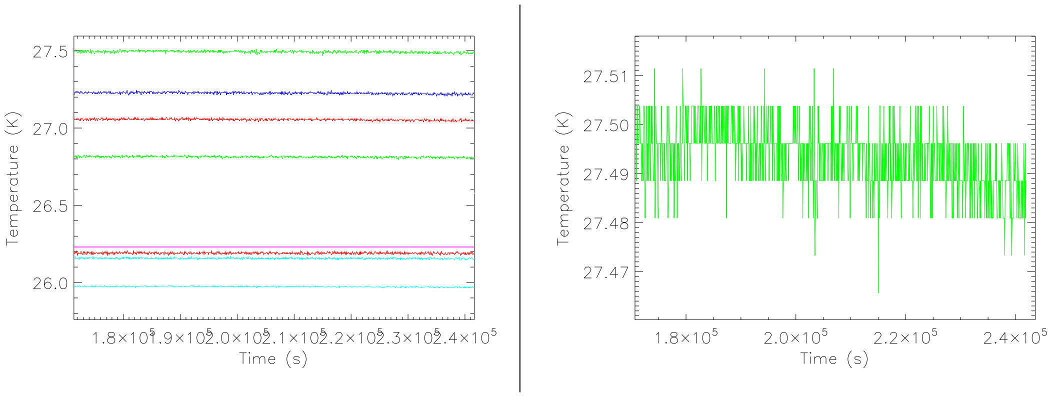

Figure 51: Behaviour of FEU temperatures during the LIS_0001 test. Left: view of all the working FPU sensors, right: detail of sensor TS2R

In Figure 52and 55, we show the variation of the back-end unit temperature sensors. They have the same behaviour but different level. We have used different data files for the tests. The sensor we have considered in the tests is R-BEM1. We have done more tests using other sensors and we have found similar results because we use differences between the temperatures independently of the level. The BEM temperature was cooled continously from the maximun to the minimum temperature. We used small sections of data in which the temperature is constant assuming conditions of thermal stability.

30 GHz - LFI28

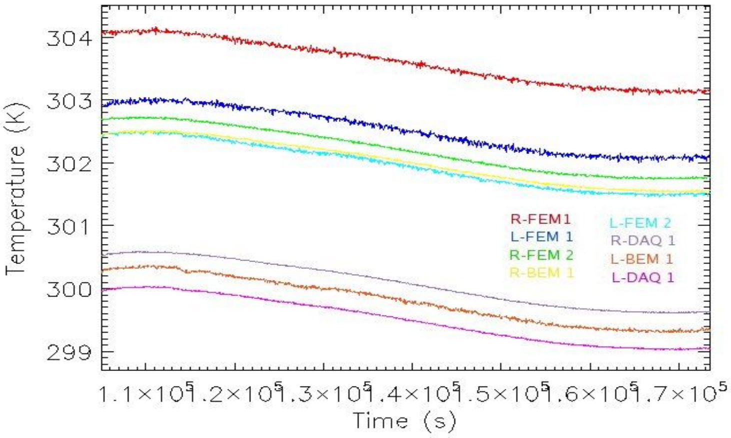

Figure 52: BEU temperatures during the temperature susceptibility test (LFI28)

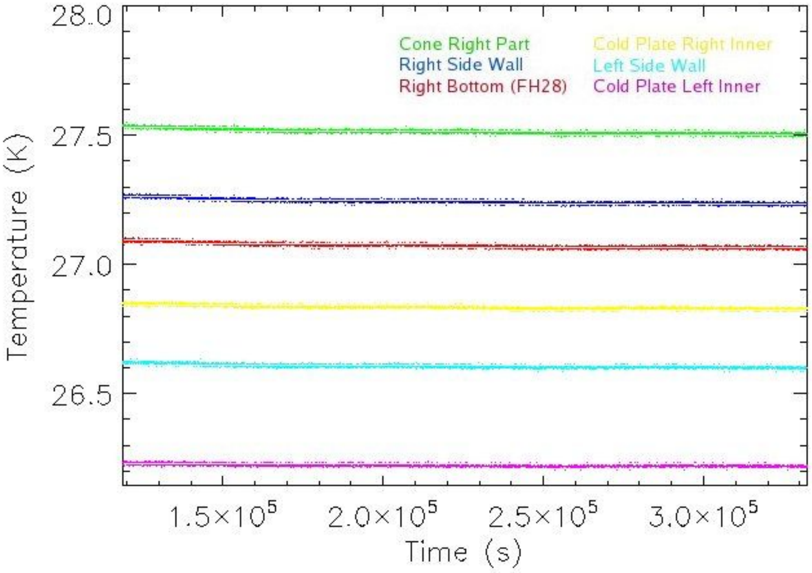

In Figure 54 we show the behaviour of the sky and reference load temperatures

Figure 53: Focal plane temperatures during the temperature susceptibility test (LFI28)

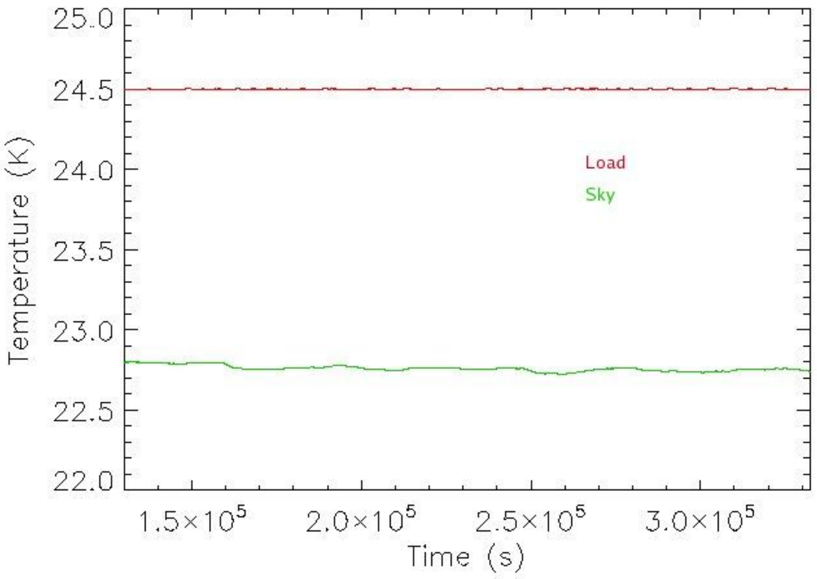

Figure 54: Sky (green line) and reference load (red line) temperature behaviour during the temperature susceptibility test (LFI28)

44 GHz - LFI24

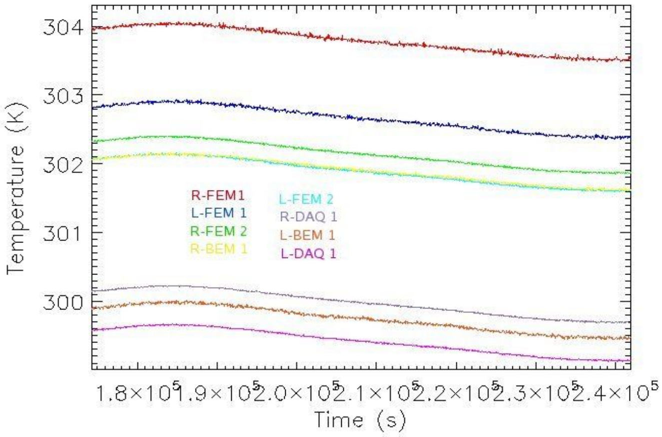

Figure 55: BEU temperatures during the temperature susceptibility test (LFI24)

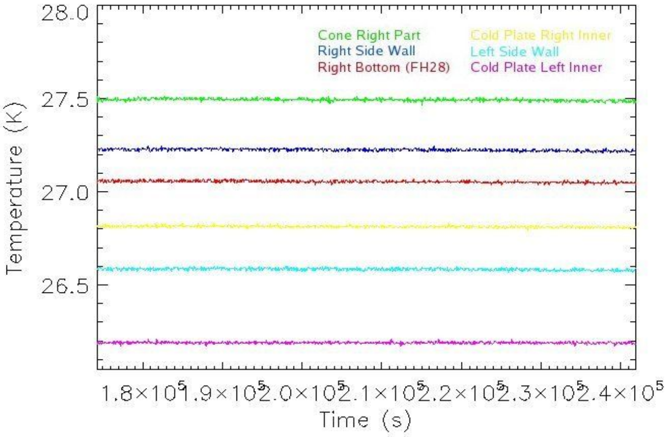

In Figure 57 we show the behaviour of the sky and reference load temperatures

Figure 56: Focal plane temperatures during the temperature susceptibility test (LFI24)

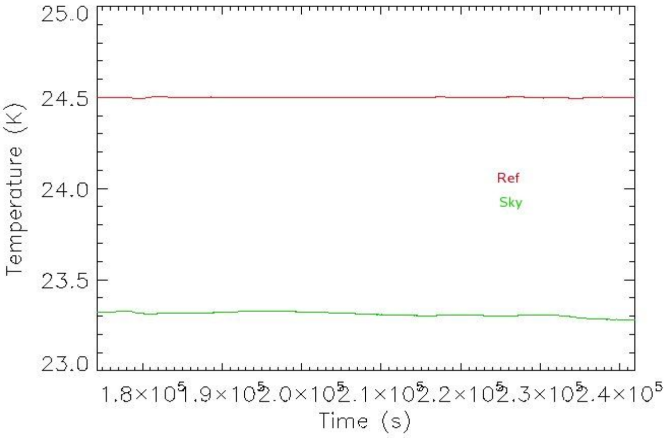

Figure 57: Sky (green line) and reference load (red line) temperature behaviour during the temperature susceptibility test (LFI24)

7.2.3 Results

30 GHz - LFI28 In Table 30 we summarise the measured transfer functions for the 30 GHz RCA compared with those calculated from the theoretical model. The parameters used in the theoretical calculation are summarised in Table 29 (crf with Table 47 of [AD4]).

Table 29: Receiver parameters used in the computation of the theoretical transfer functions

	Ch. A	**Ch. B**	**Ch. C**	**Ch. D**
$L_{feed-OMT}$ (dB)	0.25			
L_{4K} (dB)	0.2			
r	0.94533345	0.94339329	0.97562057	0.95901671
T_{sky} (K)	22.8			
T_{ref} (K)	24.5			
G^{dB}_{F1} (dB)	35			
G^{dB}_{F2} (dB)	35			
T_{nF1} (K)	20		20	
T_{nF2} (K)	20		20	
T_{nB1} (K)	350			
T_{nB2} (K)	350			
$\frac{\partial(G^{dB}_{B1})}{\partial(T^{BE}_{phys})}$ (dB/K)	-0.04	-0.05	-0.05	-0.04
$\frac{\partial(G^{dB}_{B2})}{\partial(T^{FE}_{phys})}$ (dB/K)	-0.04	-0.05	-0.05	-0.04
$\frac{\partial(a_{dB})}{\partial(T^{BE}_{phys})}$ (dB/K)	-0.01	-0.01	-0.01	-0.01
Gain Calibration factor (V/K)	0.02983	0.02732	0.03141	0.03535

Table 30: Measured and theoretical transfer functions $f^{back-end}_{therm}$

$f^{front-end}_{therm}$ (K/K)	Channel A		Channel B		Channel C		Channel D	
[meas | theo]	-0.018	-0.010	-0.016	-0.0137	-0.026	0.007	-0.024	-0.0029

44 GHz - LFI24 In Table 32 we summarise the measured transfer functions for the 30 GHz RCA compared with those calculated from the theoretical model. The parameters used in the theoretical calculation are summarised in Table 31 (crf with Table 35 of [AD3]).

Table 31: Receiver parameters used in the computation of the theoretical transfer functions

	Ch. A	**Ch. B**	**Ch. C**	**Ch. D**
$L_{\mathrm{feed-OMT}}$ (dB)	0.1			
L_{4K} (dB)	0.02			
r 0.95999742	0.99961401		0.91242703	0.93991017
T_{sky} (K)	23.317			
T_{ref} (K)	24.5			
$G^{\mathrm{dB}}_{\mathrm{F1}}$ (dB)	35			
$G^{\mathrm{dB}}_{\mathrm{F2}}$ (dB)	35			
T_{nF1} (K)	30	30	20	20
T_{nF2} (K)	30	30	20	20
T_{nB1} (K)	350			
T_{nB2} (K)	350			
$\frac{\partial(G^{\mathrm{dB}}_{\mathrm{B1}})}{\partial(T^{\mathrm{BE}}_{\mathrm{phys}})}$ (dB/K)	-0.016	-0.016	-0.1	-0.061
$\frac{\partial(G^{\mathrm{dB}}_{\mathrm{B2}})}{\partial(T^{\mathrm{FE}}_{\mathrm{phys}})}$ (dB/K)	-0.016	-0.016	-0.1	-0.061
$\frac{\partial(a_{\mathrm{dB}})}{\partial(T^{\mathrm{BE}}_{\mathrm{phys}})}$ (dB/K)	-0.004	-0.004	-0.024	-0.03
Gain Calibration factor (V/K)	0.007747	0.004190	0.00448	0.00383

Table 32: Measured and theoretical transfer functions $f^{\mathrm{back-end}}_{\mathrm{therm}}$

$f^{\mathrm{front-end}}_{\mathrm{therm}}$ (K/K)	Channel A		Channel B		Channel C		Channel D	
[meas | theo]	-0.0263	-0.004999	-0.11268	0.005	-0.0231	-0.0799	-0.0172	-0.0332

7.3 Susceptibility to bias voltage fluctuations

7.3.1 Test theory

The objective of this test is the measurement of the radiometric response in the differencial output to variation of the Gate 1 Voltage.

7.3.2 Test experimental conditions

In the following figures we show the Vgate1 for the channel during the tests.

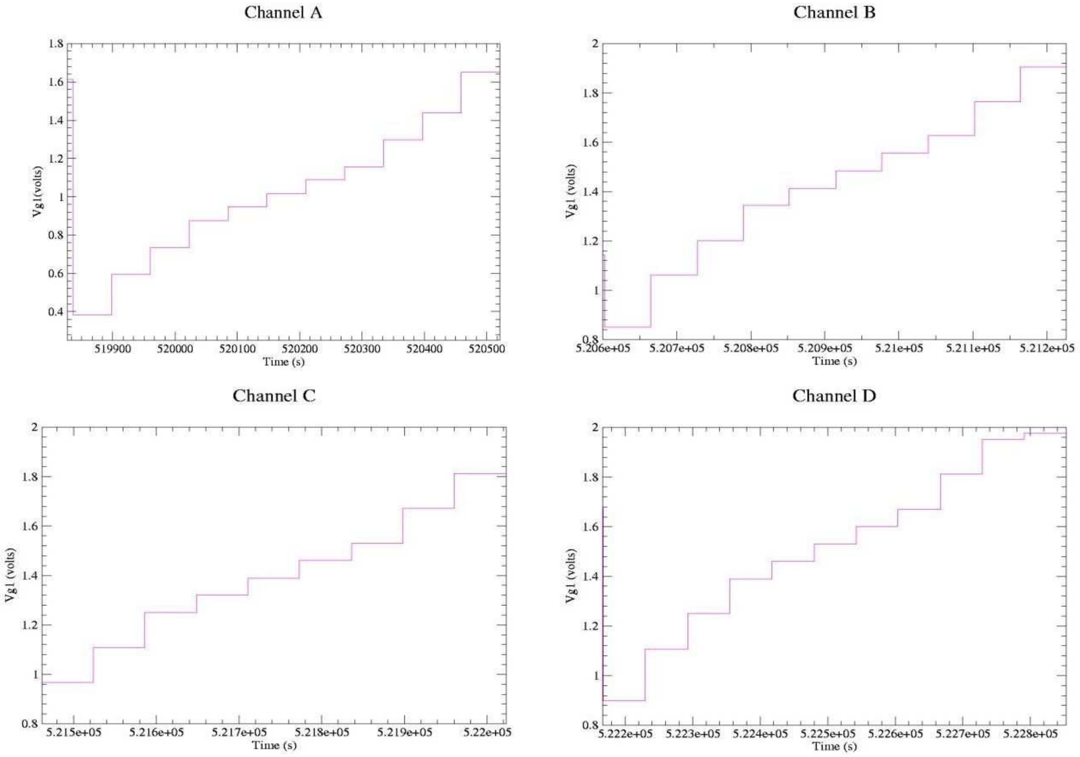

Figure 58: Vgate1 voltages

In Figure 59, we show the back-end unit temperature sensors.

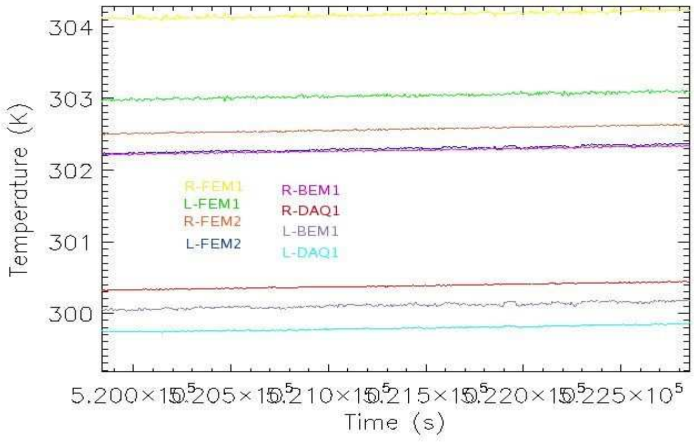

Figure 59: BEU temperatures during the test

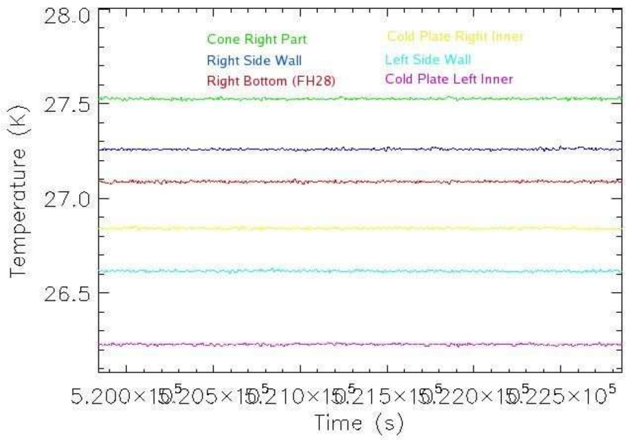

Figure 60: Focal plane temperatures during the test

In Figure 61 we show the behaviour of the sky and reference load temperatures

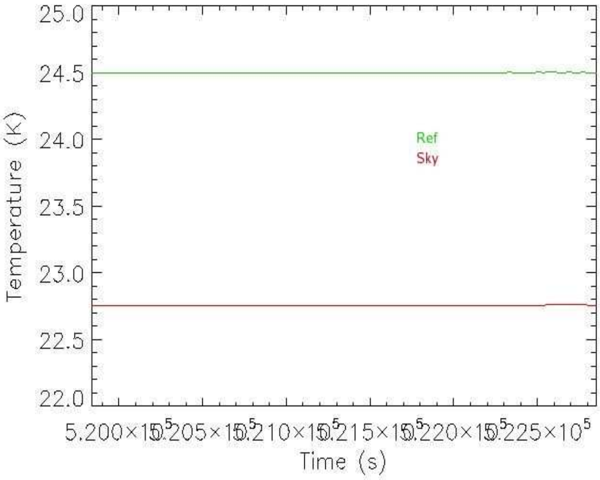

Figure 61: Sky (green line) and reference load (red line) temperature behaviour during the test

In Figure 62 we show the behaviour of the sky and reference load signals during temperatures

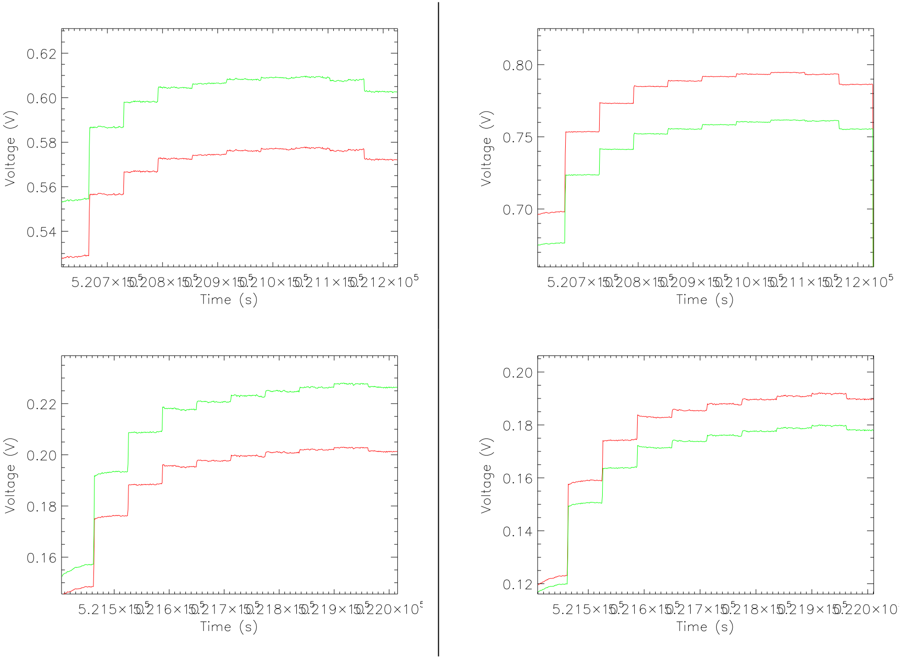

Figure 62: Sky (green line) and reference load (red line) signals during the test: top-left – channel A, top-right – channel B, bottom-left – channel C, bottom-right – channel D

7.3.3 Results

44 GHz - LFI24 In Table 34 we summarise the measured transfer functions compared with those calculated from the theoretical model. The parameters used in the theoretical calculation are summarised in Table 33.

Table 33: Receiver parameters used in the computation of the theoretical transfer functions

	Ch. A	**Ch. B**	**Ch. C**	**Ch. D**
$L_{feed-OMT}$ (dB)	0.1			
L_{4K} (dB)	0.02			
r 0.947282	0.969198		0.897251	0.938033
T_{sky} (K) 2.756	22.756	22.756	22.758	
T_{ref} (K)	24.5			
G^{dB}_{F1} (dB)	35			
G^{dB}_{F2} (dB)	35			
T_{nF1} (K)	30	30	20	20
T_{nF2} (K)	30	30	20	20
$\frac{\partial(G^{dB}_{F1})}{\partial(V_{gate1})}$ (dB/K)	10	10	4	4
$\frac{\partial(G^{dB}_{F2})}{\partial(V_{gate1})}$ (dB/K)	10	10	4	4
$\frac{\partial(T_{nF1})}{\partial(V_{gate1})}$ (K/V)	-52.7	-52.7	-30	-30
$\frac{\partial(T_{nF1})}{\partial(V_{gate1})}$ (K/V)	-52.7	-52.7	-30	-30
Gain Calibration factor (V/K)	0.007747	0.004190	0.00448	0.00383

Table 34: Measured and theoretical transfer functions $f^{\rm front-end}_{\rm Vbias}$

$f^{\rm front-end}_{\rm Vbias}$ (K/V)	Channel A		Channel B		Channel C		Channel D	
[meas | theo]	-0.03419	-0.03773	-1.68605	-1.6169	-0.77	-0.479	-0.0642	-0.8975

8 REBA quantisation and compression tests

8.1 Behaviour of the compression rate versus the quantisation factor

Data of TUN_0013 FH24 are analysed for test the compression efficiency as a function of the requantisation parameter Q. In order to analyse only the impact of Q we have set to zero the parameter GMF2. We have also tested the compressor in a very extreme limit of $Q \sim 1000$ to check its functionality in presence of very noisy data. The dispersion in the compression rate is small and well within the expected range

If we indicate with Cr the compression rate it is possible to linearly regress $1/Cr$ as a function of $\log(Q)$: $1/Cr \sim 0.135960 + \log 10(Q) * 0.254844$ with a good linearity as expected from theory.

However from theory the ideal scaling would be $1/Cr \propto \alpha * log10(Q)$ with $\alpha \sim 1$. Cr dispersion for different detectors seems to be ascribed to different levels of white noise.

Table 35: Compression factors for different REBA parameters for TUN_0013, FH=24 all the detectors.

						DTC=00		DTC=01		DTC=10	
TIME	NP	GMF1	GMF2	REQUANT	OFFSET	CR	RMSCR	CR	RMSCR	CR	RMSCR
26135.748	60	1.0	0.8	1.0	0.0	7.32	0.09	7.00	0.08	7.01	0.13
26422.880	47	1.0	0.0	1.5	0.0	4.59	0.09	4.73	0.08	4.21	0.08
26674.877	60	1.0	0.0	5.0	0.0	2.84	0.04	2.90	0.08	2.62	0.06
27013.571	138	1.0	0.0	1000.0	0.0	1.11	0.01	1.12	0.02	1.08	0.02

Table 36: Compression factors for different REBA parameters for TUN_0034, FH=28, DTC = 10

TIME	NP	GMF1	GMF2	REQUANT	OFFSET	CR	RMSCR
349705.567	55	0.940382	0.762557	1.000000	0.00	5.89	0.09
350178.067	85	0.940382	0.762557	1.000000	-1265.00	5.74	0.08
350902.567	44	0.940382	0.762557	2.877698	-1265.00	3.66	0.10
351311.882	16	0.940382	0.762557	4.285714	-1265.00	3.16	0.13
351429.607	13	0.940382	0.762557	7.142857	-1265.00	2.73	0.25
351545.610	9	0.940382	0.762557	11.428570	-1265.00	2.20	0.06
351611.040	155	0.940382	0.762557	17.142860	-1265.00	1.86	0.06

As expected the offset does not affect in a significant way the compression rate. The scaling with $\log 10(Q)$ is nearly linear: $1/Cr \sim 0.158413 + \log 10(Q) * 0.279746$. A quadratic law improves slightly the fit.

Table 37: Compression factors for different REBA parameters for TUN_0034, FH=28, DTC = 10

TIME	NP	GMF1	GMF2	REQUANT	OFFSET	CR	RMSCR
329266.162	56	0.862000	1.022000	2.857000	0.00	3.56	0.02
329772.777	29	0.862000	1.022000	4.286000	0.00	2.99	0.15
329996.199	25	0.862000	1.022000	7.143000	0.00	2.57	0.24
330185.876	20	0.862000	1.022000	11.429000	0.00	2.14	0.17
330359.465	1570	0.862000	1.022000	17.143000	0.00	1.82	0.03
346981.259	121	0.870619	1.020719	17.143000	0.00	1.83	0.02

The relationship is $1/Cr \sim 0.114807 + log10(Q) * 0.343435$. Alse in this case a quadratic law improves only slightly the fit.

In Fig. 63 we show graphically this result

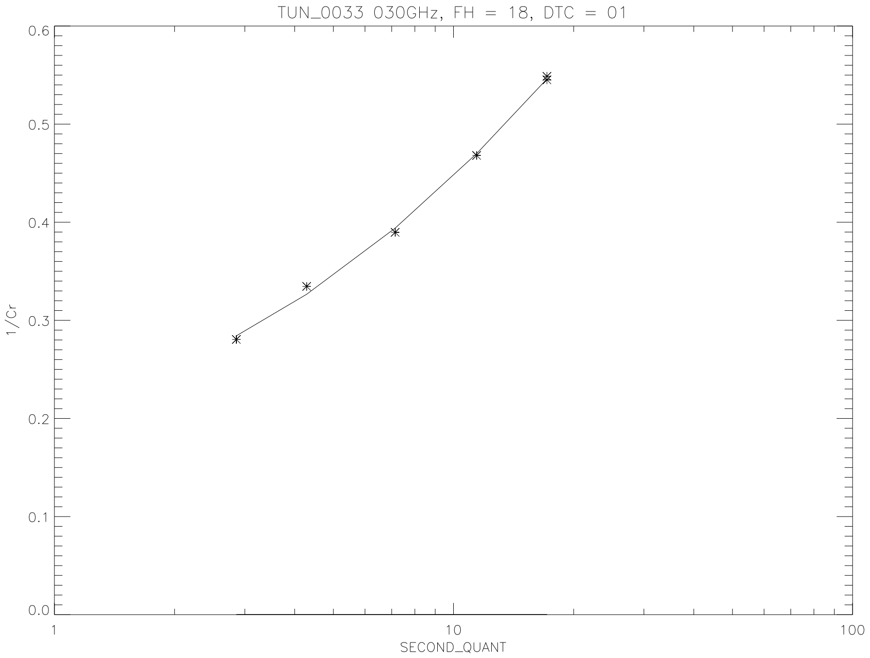

Figure 63: Behaviour of the compression rate versus the quatisation factor

8.2 Impact of second quantisation on scientific output

Tests aimed at the characterisation of the impact of second quantisation could not be analysed because of some bugs in the TQL/TMH software that showed up when the REBA worked in nominal (i.e. quantised and compressed) mode. The software has then been patched and tested. A report on the recent tests that were performed on the software is now ready and will be released soon [[RD3]].

9 Dynamic thermal response of the focal plane unit to temperature fluctuations

See technical note attached in Appendix B

A Appendix: Receiver basic properties – detailed figures

In this appendix we report detailed numerical results of receiver noise temperature, calibration constant and isolation, calculated as discussed in Sect. 5

Case 1: sky load temperature sensor on metal plate. BEU temperature fluctuation present in data

	Noise temperature							
	Channel A		***Channel B***		***Channel C***		***Channel D***	
	Tnoise	*sigma*	*Tnoise*	*sigma*	*Tnoise*	*sigma*	*Tnoise*	*sigma*
LFI28	27.17	0.69	26.95	0.72	24.53	0.88	21.78	0.85
LFI24	57.08	1.59	46.03	1.80	28.03	1.01	17.94	0.66
LFI23	61.77	1.04	63.57	2.17	61.46	1.42	55.44	0.99

	Calibration constant							
	Channel A		***Channel B***		***Channel C***		***Channel D***	
	G (K/V)	*sigma*	*G (K/V)*	*sigma*	*G (K/V)*	*sigma*	*G (K/V)*	*sigma*
LFI28	36.22624	0.22778	40.01154	0.25282	34.96276	0.21795	30.97560	0.19076
LFI24	161.74743	1.16628	106.59269	1.43488	254.27040	2.27859	285.69534	2.62100
LFI23	205.02397	1.75008	272.08233	2.50622	158.59137	1.45783	148.61477	1.28199

	Isolation							
	Channel A		***Channel B***		***Channel C***		***Channel D***	
	Iso (dB)	*sigma*	*Iso (dB)*	*sigma*	*Iso (dB)*	*sigma*	*Iso (dB)*	*sigma*
LFI28	-11.64035	0.48606	-11.79632	0.54140	-9.08139	0.32678	-9.93980	0.45968
LFI24	-8.36066	0.33538	-8.44461	0.34208	-13.70060	1.44000	-11.34979	0.38680
LFI23	-9.27574	0.25672	-8.61788	0.42278	-9.41906	0.41516	-8.76096	0.23966

Case 1: sky load temperature sensor on metal plate. BEU temperature fluctuation removed from data

	Noise temperature							
	Channel A		***Channel B***		***Channel C***		***Channel D***	
	Tnoise	*sigma*	*Tnoise*	*sigma*	*Tnoise*	*sigma*	*Tnoise*	*sigma*
LFI28	26.59	0.60	26.30	0.63	24.11	0.78	21.41	0.75
LFI24	55.63	1.19	44.53	1.30	28.24	1.01	17.99	0.60
LFI23	64.38	1.31	66.71	2.06	67.94	2.58	56.78	1.09

	Calibration constant							
	Channel A		***Channel B***		***Channel C***		***Channel D***	
	G (K/V)	*sigma*	*G (K/V)*	*sigma*	*G (K/V)*	*sigma*	*G (K/V)*	*sigma*
LFI28	36.18	0.21	39.87	0.23	35.23	0.21	31.13	0.18
LFI24	161.86	1.21	106.64	1.31	257.75	3.03	289.73	2.51
LFI23	209.37	2.02	286.32	3.49	167.69	2.71	147.83	1.63

	Isolation							
	Channel A		***Channel B***		***Channel C***		***Channel D***	
	Iso (dB)	*sigma*	*Iso (dB)*	*sigma*	*Iso (dB)*	*sigma*	*Iso (dB)*	*sigma*
LFI28	-11.04	0.36	-11.18	0.40	-8.70	0.24	-9.52	0.34
LFI24	-8.04	0.23	-8.06	0.22	-13.01	1.44	-10.69	0.30
LFI23	-9.43	0.41	-8.40	0.42	-9.70	0.68	-9.30	0.18

Case 2: sky load temperature sensor on ECCOSORB. BEU temperature fluctuation present in data

	Noise temperature							
	Channel A		***Channel B***		***Channel C***		***Channel D***	
	Tnoise	*sigma*	*Tnoise*	*sigma*	*Tnoise*	*sigma*	*Tnoise*	*sigma*
LFI28	22.62	0.52	22.41	0.55	20.10	0.73	17.49	0.70
LFI24	51.18	1.36	40.66	1.61	23.32	1.01	13.86	0.56
LFI23	55.68	0.82	57.33	1.83	55.98	1.39	49.67	0.92

	Calibration constant							
	Channel A		***Channel B***		***Channel C***		***Channel D***	
	G (K/V)	*sigma*	*G (K/V)*	*sigma*	*G (K/V)*	*sigma*	*G (K/V)*	*sigma*
LFI28	34.41868	0.08145	38.01510	0.09268	33.21924	0.09341	29.43093	0.07793
LFI24	153.99186	1.20084	101.48306	1.40092	241.68206	2.28269	271.43888	1.91950
LFI23	195.07975	0.32528	258.86625	0.58876	151.80730	0.33004	141.40355	0.20952

	Isolation							
	Channel A		***Channel B***		***Channel C***		***Channel D***	
	Iso (dB)	*sigma*	*Iso (dB)*	*sigma*	*Iso (dB)*	*sigma*	*Iso (dB)*	*sigma*
LFI28	-11.64035	0.48606	-11.79632	0.54140	-9.08139	0.32678	-9.93980	0.45968
LFI24	-8.36066	0.33538	-8.44461	0.34208	-13.70060	1.44000	-11.34979	0.38680
LFI23	-9.27574	0.25672	-8.61788	0.42278	-9.41906	0.41516	-8.76096	0.23966

Case 2: sky load temperature sensor on ECCOSORB. BEU temperature fluctuation removed from data

	Noise temperature							
	Channel A		***Channel B***		***Channel C***		***Channel D***	
	Tnoise	*sigma*	*Tnoise*	*sigma*	*Tnoise*	*sigma*	*Tnoise*	*sigma*
LFI28	22.09	0.52	21.81	0.55	19.72	0.69	17.16	0.66
LFI24	49.82	1.01	39.25	1.15	23.55	1.01	13.92	0.55
LFI23	58.15	1.10	60.31	1.65	62.19	2.49	50.95	1.03

	Calibration constant							
	Channel A		***Channel B***		***Channel C***		***Channel D***	
	G (K/V)	*sigma*	*G (K/V)*	*sigma*	*G (K/V)*	*sigma*	*G (K/V)*	*sigma*
LFI28	34.37456	0.11708	37.88689	0.13179	33.48348	0.19745	29.58501	0.13423
LFI24	154.14662	1.55511	101.54535	1.38367	245.06596	3.28860	275.33545	2.18339
LFI23	199.25363	1.47908	272.50083	2.86656	160.50063	2.12363	140.71873	1.39226

	Isolation							
	Channel A		***Channel B***		***Channel C***		***Channel D***	
	Iso (dB)	*sigma*	*Iso (dB)*	*sigma*	*Iso (dB)*	*sigma*	*Iso (dB)*	*sigma*
LFI28	-11.03559	0.35781	-11.18261	0.39556	-8.69548	0.24318	-9.52396	0.33831
LFI24	-8.03651	0.22534	-8.06472	0.21651	-13.01432	1.44000	-10.68803	0.29524
LFI23	-9.42890	0.41251	-8.39598	0.41810	-9.70011	0.67756	-9.30467	0.18249

B Appendix: Technical note on dynamic thermal tests

INAF-IASF Sez. di Milano
LFI Project System Team

Planck LFI

TITLE: **Analysis of dynamic thermal tests performed during the LFI QM test campaign**

DOC. TYPE: Technical Note
PROJECT REF.: PL-LFI-PST-TN-070
PAGE: 1 of 8
ISSUE/REV.: 1.0
DATE: December 15, 2005

Prepared by	Maurizio Tomasi	December 15, 2005
Agreed by	M. Bersanelli LFI Instrument Scientist C.R. Butler LFI Program Manager	December 15, 2005
Approved by	N. Mandolesi LFI Principal Investigator	December 15, 2005

CHANGE RECORD

Issue	**Date**	**Sheet**	**Description of change**	**Release**
1.0	15th Dec, 2005	All	First issue of document	1.0

DISTRIBUTION LIST

Recipient	**Company/Institute**	**E-mail address**	**Sent**
E. Alippi	Alenia Spazio S.p.A.	`alippi.e@laben.it`	Yes
M. Balasini	Alenia Spazio S.p.A.	`balasini.m@laben.it`	Yes
P. Battaglia	Alenia Spazio S.p.A.	`battaglia.p@laben.it`	Yes
E. Artal	Univ. of Cantabria - Santander	`artal@dicom.unican.es`	Yes
M. Bersanelli	Univ. degli studi di Milano	`marco.bersanelli@fisica.unimi.it`	Yes
C. Burigana	INAF-IASF sez di Bologna	`burigana@bo.iasf.cnr.it`	Yes
C. Butler	IASF-CNR Sez di Bologna	`butler@bo.iasf.cnr.it`	Yes
G. Cafagna	Alenia Spazio S.p.A.	`cafagna.g@laben.it`	Yes
B. Cappellini	Univ. degli studi di Milanl	`benedetta.cappellini@mi.infn.it`	Yes
B. Collaudin	ASPI - Cannes	`bernard.collaudin@space.alcatel.fr`	Yes
F. Cuttaia	INAF-IASF sez di Bologna	`cuttaia@bo.iasf.cnr.it`	Yes
O. D'Arcangelo	IFP - CNR	`ocleto@ifp.cr.it`	Yes
R. Davis	JBO - UK	`rjd@jb.man.ac.uk`	Yes
X. Dupac	INAF-OAT - Trieste	`dupac@oat.ts.astro.it`	Yes
L. Figini	IFP - CNR	`figini@ifp.cr.it`	Yes
C. Franceschet	Alenia Spazio S.p.A.	`franceschet.c@laben.it`	Yes
E. Franceschi	INAF-IASF sez di Bologna	`franceschi@bo.iasf.cnr.it`	Yes
T. Gaier	JPL - Pasadena	`gaier@merlin.jpl.nasa.gov`	Yes
S. Galeotta	INAF-IASF sez. di Milano	`samuele@mi.iasf.cnr.it`	Yes
M. Guerrini	INAF-OAT - Trieste	`guerrini@oat.ts.astro.it`	Yes
H. Hyates	JBO - UK	`hyates@jb.man.ac.uk`	Yes
R. Hoyland	IAC - Tenerife	`rjh@ll.iac.es`	Yes
N. Hughes	Ylinen	`nicholas.hughes@elektrobit.com`	Yes
D. Kettle	JBO - UK	`dkettle@jb.man.ac.uk`	Yes
M. Laaninen	Ylinen	`mikko.laaninen@elektrobit.com`	Yes
J.M. Lamarre	IAS - Orsay	`lamarre@ias.u-psud.fr`	Yes
C. Lawrence	JPL - Pasadena	`crl@jplsp.ipl.nasa.gov`	Yes
R. Leonardi	UCSB – USA	`rodrigo@deepspace.ucsb.edu`	Yes
P. Leutenegger	Alenia Spazio S.p.A.	`leutenegger.p@laben.it`	Yes
S. Lowe	JBO - UK	`S.R.Lowe@postgrad.manchester.ac.uk`	Yes
D. Maino	Univ. degli studi di Milano	`davide.maino@fisica.unimi.it`	Yes
M. Malaspina	INAF-IASF sez di Bologna	`malaspina@bo.iasf.cnr.it`	Yes
N. Mandolesi	INAF-IASF Sez. di Bologna	`reno@bo.iasf.cnr.it`	Yes
M. Maris	INAF-OAT - Trieste	`maris@oat.ts.astro.it`	Yes
J. Marti Canales	ESA	`javier.marti.canales@esa.int`	Yes
E. Martinez-Gonzalez	Univ. of Cantabria - Santander	`martinez@ifca.unican.es`	Yes
P. Meinhold	UCSB – USA	`peterm@cfi.ucsb.edu`	Yes
L. Mendes	ESA	`lmendes@rssd.esa.int`	Yes
A. Mennella	Univ. degli studi di Milano	`daniele.mennella@fisica.unimi.it`	Yes
M. Miccolis	Alenia Spazio S.p.A.	`miccolis.m@laben.it`	Yes
G. Morgante	INAF-IASF Sez. di Bologna	`morgante@bo.iasf.cnr.it`	Yes
L. Pagan	Alenia Spazio S.p.A.	`pagan.l@laben.it`	Yes
F. Pasian	INAF-OAT - Trieste	`pasian@oat.ts.astro.it`	Yes
T. Passvogel	ESA - PT	`tpassvog@estec.esa.nl`	Yes

L. Popa	INAF-IASF sez di Bologna	`popa@bo.iasf.cnr.it`	Yes
J.L. Puget	IAS - Orsay	`puget@ias.u-psud.fr`	Yes
N. Roddis	JBO - UK	`nr@jb.man.ac.uk`	Yes
M. Salmon	Univ. of Cantabria - Santander	`salmon@ifca.unican.es`	Yes
M. Sandri	INAF-IASF sez di Bologna	`sandri@bo.iasf.cnr.it`	Yes
M. Seiffert	JPL - Pasadena	`michael.d.seiffert@jpl.nasa.gov`	Yes
R. Silvestri	Alenia Spazio S.p.A.	`silvestri.r@laben.it`	Yes
A. Simonetto	IFP - CNR	`simonetto@ifp.cr.it`	Yes
C. Sozzi	IFP - CNR	`sozzi@ifp.cr.it`	Yes
L. Stringhetti	INAF-IASF sez di Bologna	`stringhetti@bo.iasf.cnr.it`	Yes
J. Tauber	ESA	`jtauber@astro.estec.esa.nl`	Yes
L. Terenzi	INAF-IASF sez di Bologna	`terenzi@bo.iasf.cnr.it`	Yes
M. Tomasi	INAF-IASF sez di Milano	`tomasi@mi.iasf.cnr.it`	Yes
J. Tuovinen	Millilab	`jussi.tuovinen@vtt.fi`	Yes
L. Valenziano	INAF-IASF sez di Bologna	`valenziano@bo.iasf.cnr.it`	Yes
J. Varis	Millilab	`jussi.varis@vtt.fi`	Yes
F. Villa	INAF-IASF sez di Bologna	`villa@bo.iasf.cnr.it`	Yes
A. Wilkinson	JBO - UK	`aw@jb.man.ac.uk`	Yes
F. Winder	JBO - UK	`fwinder@jb.man.ac.uk`	Yes
A. Zacchei	INAF-OAT - Trieste	`zacchei@ts.astro.it`	Yes
LFI System PCC	INAF-IASF sez di Bologna	`lfispcc@bo.iasf.cnr.it`	Yes

Contents

1 Introduction **1**

2 An Analytical Model of the Test **1**

3 A Numerical Model **2**

4 Experimental results **3**
  4.1 Comparison with the Toy Numerical Model 3

5 Conclusions **8**

Abstract

In this report we show our progress in evaluating the thermal transfer function from the LFI FPU cold end to a point on the focal plane using the data aquired during the LFI Qualification Model Test Campaign. The objective is to estimate the spectral response of the FPU thermal mass when a fluctuation of a fixed frequency is induced on the LR2 cold end. In order to shorten the test duration, we chose not to induce a series of plain sinusoidal fluctuations, but to force a step change in temperature and then use the Discrete Fourier Transform (DFT) to decompose the temperature profile in frequencies and derive the transfer function from it. However, our analysis shows that this method is difficult to apply because of singularities in the evaluation of the transfer function from discrete data.

Reference Documents

1 Introduction

The objective of the LFI QM Transfer Function Test is to estimate how temperature fluctuations propagate from the LFI cold end through the Front Plane Unit (FPU). This test is important in order to evaluate the impact of LR2 temperature instabilities on the LFI radiometers and therefore on the measured signal. Particularly critical are the sorption cooler cycle frequencies (1/4000 Hz and 1/667 Hz) and the satellite spin frequency (1/60 Hz), the first ones because of their relatively large value compared with the white noise, the second one because of the fact that aquisition redundancy is not able to dump them.

In the QM Transfer Function Test we induce a temperature variation at the LR2 cold end and measure the temperature variation induced in several points on the FPU using termometers. Depending on the type of temperature sensor, the sampling frequency can be either 1 s or 30 s.

The simplest way to perform this test is to induce a pure sinusoidal fluctuation in temperature at the LR2 cold end and measure the amplitude of the induced fluctuation at the other points of the FPU; the transfer function is simply the ratio of the two amplitudes. We call this the *sinusoidal method*. However, in order to save some time during the test, we chose not to run this test for all those frequencies for which an estimation of the transfer function is required. Instead, we induced a temperature step change at LR2 and measured the resulting temperature change. Then, using the Discrete Fourier Transform (DFT) we tried to estimate the spectral profile of the temperature variation, and then deduce the transfer function as the ratio between the absolute amplitudes of the Fourier coefficients. We call this the *DFT method*.

The study of step temperature changes with the DFT method has not been able yet to provide reliable results. Our analytical and numerical models show that the reason is likely to be the presence of zeroes in the fourier transform of the step function, which lead to singularities when evaluating their ratio.

2 An Analytical Model of the Test

We developed an analytical model which estimates how a temperature step function propagates through an infinite one-dimensional bar. The differential equation to be solved is:

$$\begin{cases} \frac{\partial T}{\partial t}(x,t) = D\frac{\partial^2 T}{\partial x^2}(x,t), \\ T(x=0,t) = \theta(t) - \frac{1}{2}, \end{cases}$$

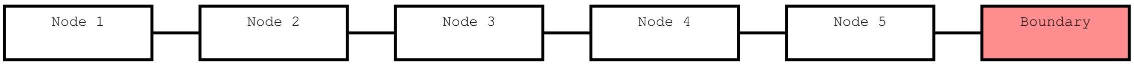

Figure 1: The numerical model used in the simulations. The temperature of the boundary node is specified by an analytical function or by a tabulated set of temperatures, depending on the test. We compare this boundary temperature with the temperature at node #1, at the other side of the bar.

where $T(x,t)$ is the temperature in x at time t, D is the thermal diffusivity constant ($[D] = \mathrm{cm/s^2}$) and $\theta(t)$ is the step function:

$$\theta(t) = \begin{cases} +1, & \text{if } t > 0, \\ 0, & \text{if } t < 0. \end{cases}$$

By decomposing the unknown solution and the boundary condition into the Fourier terms $e_n(t) = \sqrt{1/T}\exp(2\pi int/T)$, with T being the duration of the test and $n/T = \nu_n$ being the n-th frequency, we get the solution

$$T(x,t) = \sum_{n=-\infty}^{+\infty} \frac{-i}{n\pi} \sin^2(n\pi/2) \exp\left(-\sqrt{\frac{2\pi i\nu_n}{D}}x\right) \exp(2\pi i\nu_n t), \tag{1}$$

which can be written as

$$T(x,t) = \sum_{n=1}^{+\infty} \underbrace{\frac{2}{\pi(2n-1)} \exp\left(-\sqrt{\frac{\pi\nu_{2n-1}}{D}}x\right)}_{\text{Amplitude of the }(2n-1)\text{-th frequency}} \sin\left(2\pi\nu_{2n-1}t - \sqrt{\frac{\pi\nu_{2n-1}}{D}}x\right), \tag{2}$$

once we combine the terms $+n$ and $-n$ and perform the substitution $n \to 2n-1$ (since the n-th spectral component of the step function has zero amplitude because of the $\sin^2(n\pi/2)$ term).

The analytical transfer function between x_1 and x_2 is simply the ratio of the amplitude at these two points:

$$H(\nu_{2n-1}) = \exp\left(-\sqrt{\frac{\pi\nu_{2n-1}}{D}}(x_1 - x_2)\right),$$

and it is defined only for the odd frequencies ν_{2n-1}, while it is undefined for even frequencies (because the amplitudes at x_1 and x_2 are both zero). Note that $H(\nu) \sim \exp(-\sqrt{\nu})$: the analytical transfer function predicts that lower frequencies are better transferred through the mass.

3 A Numerical Model

In order not to be overcomed by the complexity of the global LFI thermal model, we developed a toy numerical model of a 1-D bar using ESATAN. This makes the test of the DFT method simpler and let us to match the results of the analytical model. The thermal model is made by 6 nodes and is shown in figure 1.

The purpose of this thermal model is to see how a temperature fluctuations induced on the boundary node (the rightmost one in the figure) induces a fluctuation on node #1 (on the other side of the bar). We tried various types of fluctuations:

1. A pure step function;
2. A sigmoid;

3. The QM temperatures taken from test THF_0002 (see below).

Finally, we used the pure step function and the QM data from test THF_0002 in the full LFI FPU thermal model, in order to have a direct comparison with the laboratory results.

4 Experimental results

Figure 2 shows the thermal reaction of one of the LFI QM feed horns (#28, a 30 GHz feed) to a step function induced at the LR2 point (data taken during the THF_0002 test), together with the results of a simulation done with ESATAN on the full LFI model and the same boundary condition on LR2.

The boundary condition used for LR2 is the mean temperature between FPU_1 and FPU_2 (the two sensors are both near the LR2 point). We averaged the two temperatures because the CSL program applied a wrong calibration curve to the two sensors, leading to an overestimation for FPU_1 and an underestimation for FPU_2.

Apart from a different offset in the temperatures (due to the fact that the full LFI thermal model assumes a deep space environment instead of considering the laboratory cryochamber), figure 2 shows a good agreement between the simulation and the experimental results. The spectral profile of the two temperatures is almost the same (apart from the noise at the higher frequencies, which is greater for the THF_0002 test), and so is the transfer function, evaluated using the DFT method.

The problem lies in the fact that the reconstructed transfer function does not show fluctuation damping, as we expected from the results of a test done on the same LFI thermal model using the sinusoidal method (see figure 3).

The reason for this discrepancy could lie in the fact that an ideal step function has a spectrum where even frequencies have zero amplitude (see equation 2).

4.1 Comparison with the Toy Numerical Model

To better understand the strange results found in the preceding section, we applied an ideal step function on the 1-D toy numerical model (see figure 1). Since the step function can be a rather crude idealization, we also used a sigmoid $s(t)$ as boundary condition:

$$s(t) = 1.5 + \frac{1}{\pi} \arctan\left(\frac{t - 5000\,\mathrm{s}}{100}\right).$$

Figure 4 shows the results. Despite the fact that we used the sigmoid too (a smooth function), both the transfer function show a widely fluctuating transfer function with no traces of dumping at the higher frequencies.

This could be related to the fact that even frequencies have zero amplitude (see equation 2), and thus the transfer function is not defined (the ratio between the amplitudes gives 0/0).

In order to verify this assumption, we applied the DFT method on the analytical function given by equation (2). The result is shown in figure 5, and even if it is qualitatively different from figure 2, yet we observe that the calculation shows an heat transfer rate which increases with the frequency, an obvious nonsense. The expected result, as given by eq. (2), should have been the one shown in figure 6.

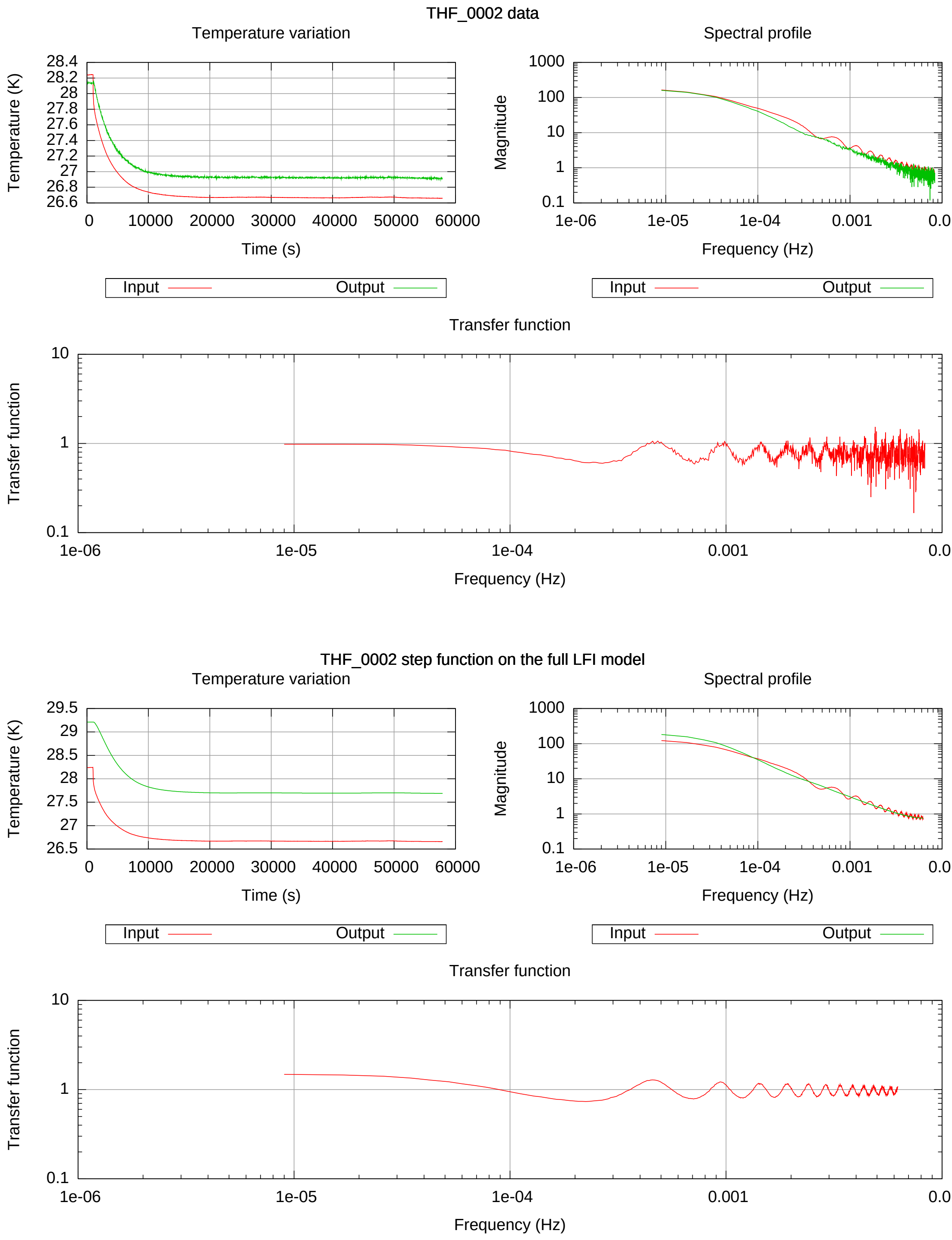

Figure 2: Comparison between the thermal behavior of the QM instrument (above) and the expected results of the full LFI numerical thermal model (below). Apart from a different offset (due to the two distinct radiative environments, the first being a cryochamber, the second the deep space), the results show a good match.

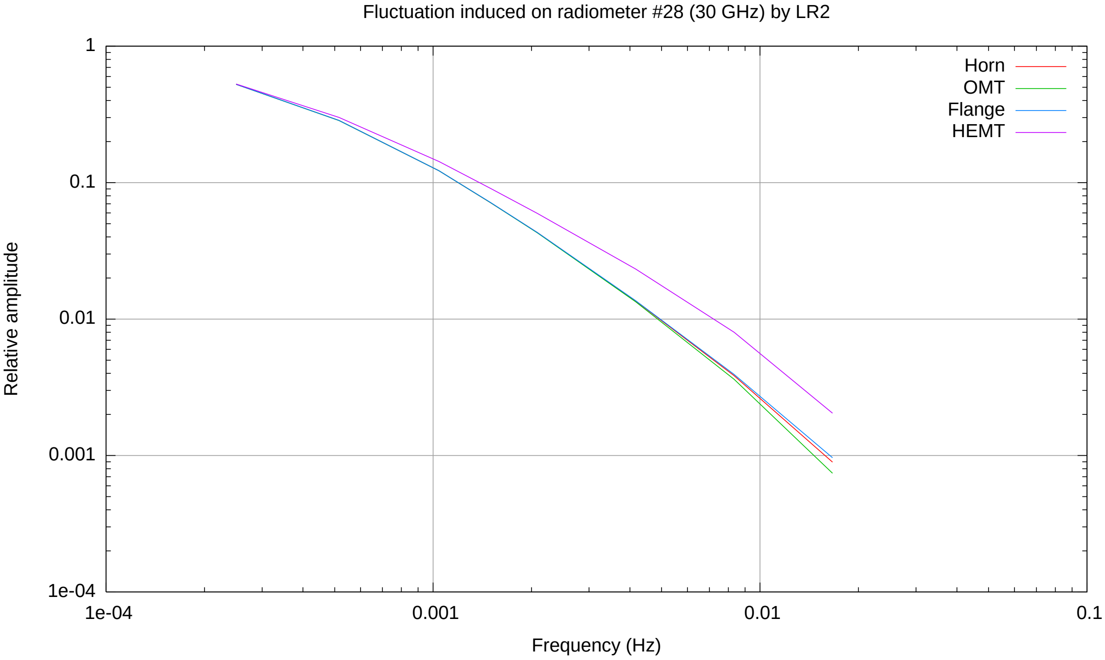

Figure 3: Expected transfer function for a fluctuation propagating from LR2 to the 30GHz feed horn #28. This has been evaluated by inducing a pure sinusoidal fluctuation in the temperature at the LR2 point using the full LFI thermal model.

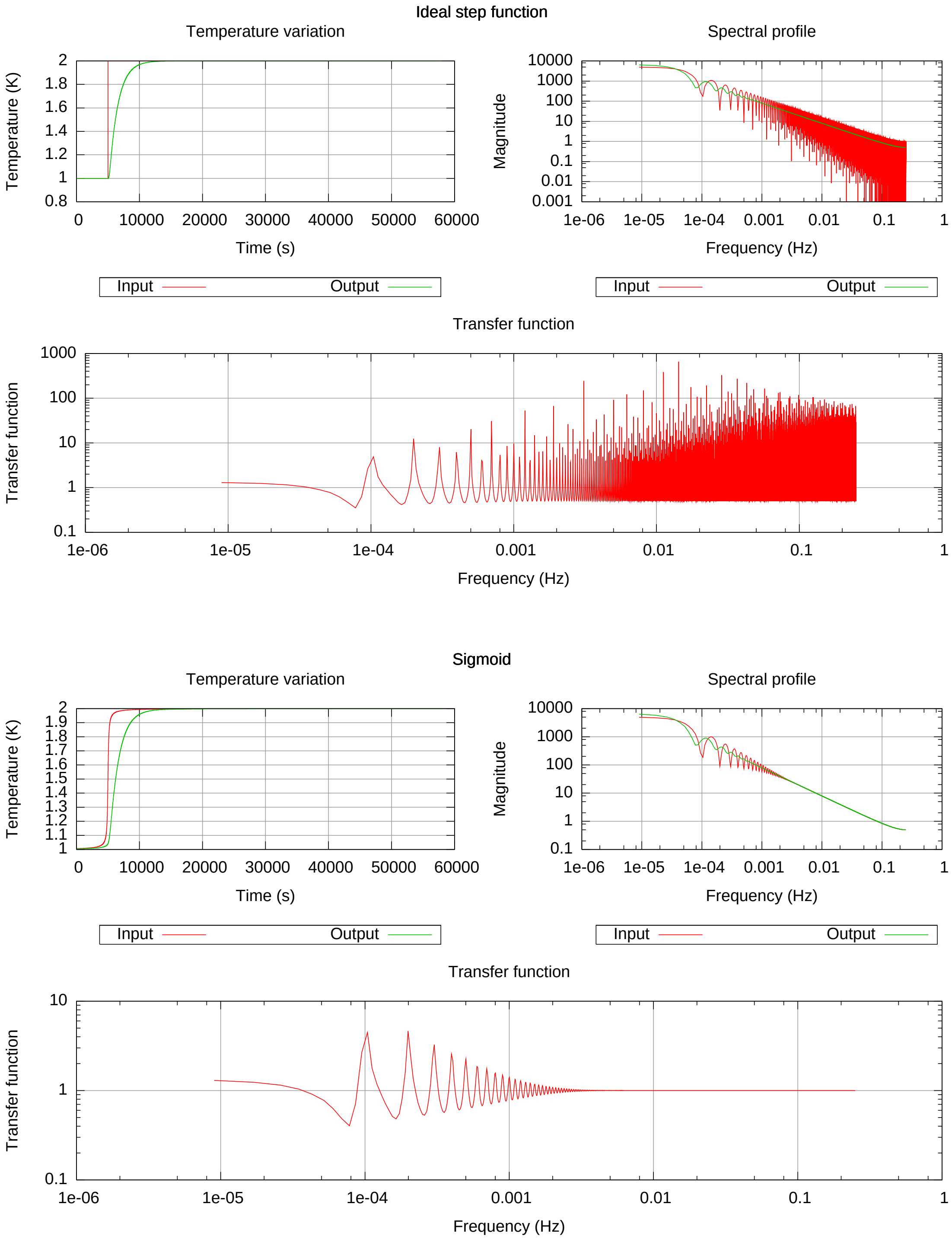

Figure 4: Tests done with the 1-D toy model. A step temperature variation (above) and a step-like variation (below) has been induced on one side of the bar, and the corresponding temperature on the other side has been used to estimate the transfer function.

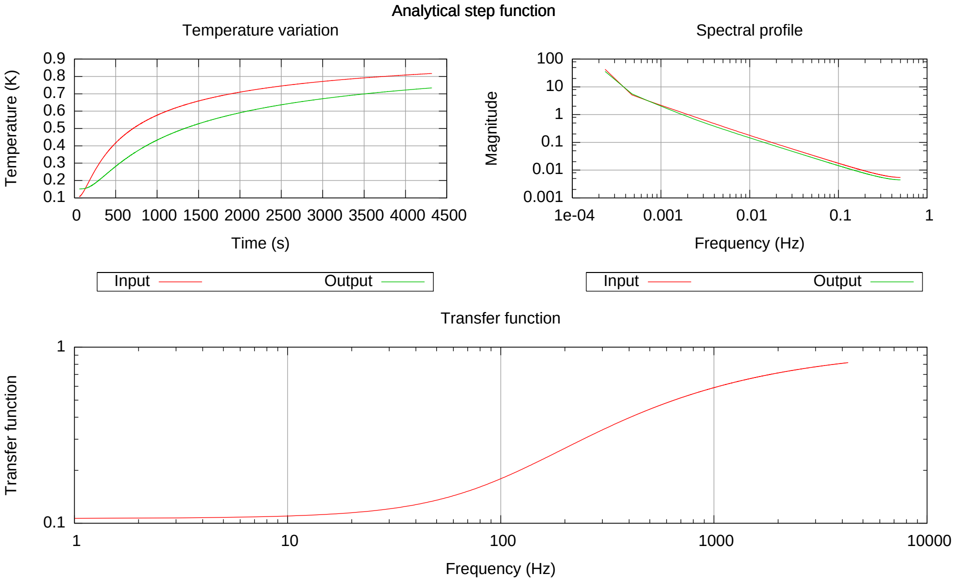

Figure 5: The DFT method has been applied to the analytical function given by equation (2). This function has been sampled with frequency 1 Hz, and then the same algorithms used to create figure 2 have been applied. In this case too we get a transfer function which does not match what we expect from the theory (i.e. a decreasing slope).

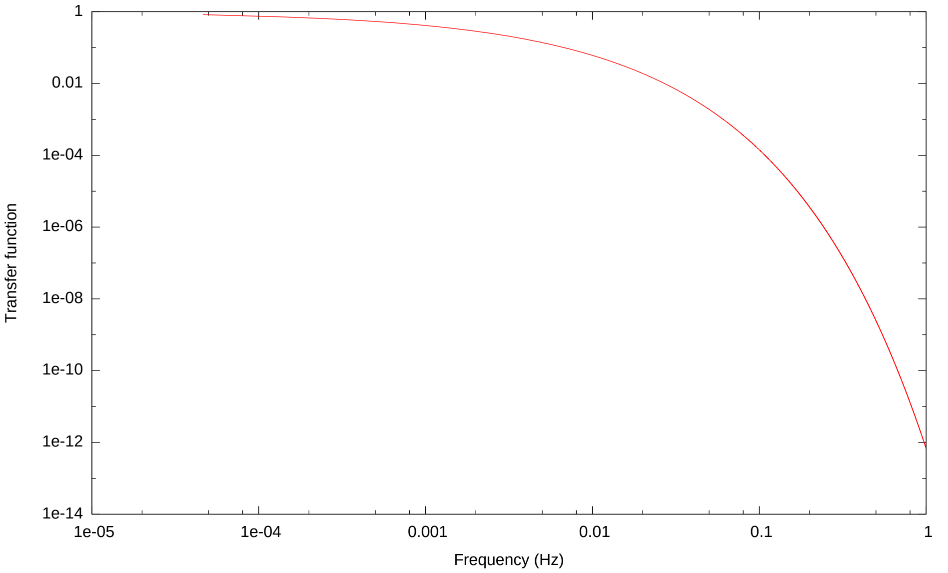

Figure 6: The transfer function as given by equation (2). It is simply the ratio of the amplitudes between two points x_1 and x_2, and it is plotted for those frequencies where the amplitude is nonzero (i.e. for ν_{2n+1}).

5 Conclusions

We could not find a way to make the DFT method produce reliable results with step-like temperature variations. The problem seems to be in the particular shape of the spectrum of the step function. We suggest that the sinusoidal method should be used in LFI FM tests. This because, despite the greater time required to do the measurements, the analysis would be considerably simpler.